Multi-Scale Modelling of Fatigue of Wind Turbine Rotor Blade Composites

Proefschrift

ter verkrijging van de graad van doctor
aan de Technische Universiteit Delft,
op gezag van de Rector Magnificus prof. ir. K.C.A.M. Luyben,
voorzitter van het College voor Promoties,
in het openbaar te verdedigen op maandag 22 april 2013 om 10:00 uur

door

Cheng QIAN

Master of Science in Materials Science and Engineering,
Beijing Institute of Technology, Beijing, China

geboren te Tonghua, Jilin, China

Dit proefschrift is goedgekeurd door de promotor:

Prof. dr. Z. Gürdal

Copromotor: Dr. C. Kassapoglou

Samenstelling promotiecommissie:

Rector Magnificus,	voorzitter
Prof. dr. Z. Gürdal,	Technische Universiteit Delft, promotor
Dr. C. Kassapoglou,	Technische Universiteit Delft, copromotor
Prof. dr. G. Q. Zhang,	Technische Universiteit Delft
Prof. dr. J. Varna,	LuleåUniversity of Technology, Zweden
Prof. dr. D. S. Cairns,	Montana State University, Verenigde Staten
Ir. D. R. V. van Delft,	Knowledge Centre Wind turbine Materials and Constructions
Dr. ir. R. P. L. Nijssen,	Knowledge Centre Wind turbine Materials and Constructions
Prof.dr. A. Rothwell,	Technische Universiteit Delft, reservelid

Ir. T. Westphal heeft als begeleider in belangrijke mate aan de totstandkoming van het proefschrift bijgedragen

故不积跬步 *If you do not accumulate little steps,*
无以至千里 *You will have no way to go a thousand li[1].*
不积小流 *If you do not accumulate small streams,*
无以成江海 *You will have no way to form river or sea.*
骐骥一跃 *Even the famous horse Qi Ji[2] could not go*
不能十步 *more than ten paces in a single leap,*
驽马十驾 *but with ten days of riding even an old nag can equal him,*
功在不舍 *because accomplishment rests in not giving up.*
锲而舍之 *If you start carving and give up,*
朽木不折 *you won't even be able to break rotten wood,*
锲而不舍 *but if you start carving and don't give up,*
金石可镂 *then you can engrave even metal and stone.*

- 劝学 An Exhortation to Learning

By 荀子 Xunzi, a Chinese philosopher
living in ca. 312 –230 BC,
Translated by Dr. Eric Hutton.

[1] *A traditional Chinese unit of distance (equal to 416 m in 770 - 250 BC).*
[2] *The legendary horse which could travel a thousand li in a single day*

Summary

Fatigue is an important design driver for wind turbine rotor blades. The strength and stiffness degradation of the composite materials caused by the fatigue damage can limit the blade service life. Thus, an adequate description of the composite fatigue damage is needed in the design of wind turbine rotor blades.

Models which can describe the fatigue behaviour of composite materials can be divided in to three categories: empirical, phenomenological and micro-mechanical models. Of these models, only micro-mechanical models are based on the failure analysis at the constituent level; fibres and matrix. Because of this, they hold the promise to be able to predict composite behaviour and the effect of changes of material and laminate configuration, with relatively limited experimental analysis, as would be required for models of the other categories.

In this dissertation, a multi-scale micro-mechanical fatigue model is presented that avoids the use of empirical or phenomenological factors at the composite laminate or structural scales. Using this model, the axial tension-tension fatigue behaviour of unidirectional Glass Fibre Reinforced Polymer (GFRP) composites is predicted, including the fatigue life and stiffness degradation. The model inputs are only material properties of fibres and matrix, and the entire calculation procedure consists of a three-step geometrical scaling-up process.

1. A small structure consisting of several fibres embedded in a matrix is modelled as a Multi-Fibre (MF) unit cell. The fatigue behaviour of this cell is simulated by considering (sequential) fibre breakages as the dominant mechanism. Simulation outputs are the fatigue life predictions and elastic constant degradation of the MF unit cells.

2. The fatigue behaviour of composite at the meso-scale is simulated by using the predicted MF unit cell properties as inputs. This model

is called the Meso-Structure (MS) model. The MS model is analysed using the finite element method, where each element is equivalent to an MF unit cell. The outputs of this analysis are the fatigue life predictions and elastic constant degradation of the MS models.

3. The fatigue behaviour of composites at the macro-scale is simulated by using the predicted MS model properties as inputs. In this numerical model a part of a test coupon is simulated and therefore it is called the Coupon-Size (CS) model. In turn, this model is made up of MS elements.

As the geometrical size increases, the S-N slope does not significantly change. The fatigue lives scatter is reduced by several orders of magnitude, and the axial stiffness degradation exhibits more clustered and sudden-death behaviour. At a single scale, for instance the meso- or macro-scale, the axial stiffness degradation rate is slightly reduced and the scatter in the stiffness degradation decreases, with the input fibre S-N slope reduced from -10.0 to -30.0, which covers the possible fibre S-N slopes extracted from single fibre fatigue tests.

Compared to the experimental results of the unidirectional GFRP composite dog-bone coupons tested in this project, the predicted fatigue lives are longer by one order of magnitude. This is probably due to not modeling some fatigue failure mechanisms, such as the fibre debonding. Nevertheless, the predicted axial stiffness degradation agrees with the experimental observations.

Samenvatting

Vermoeiing is bepalend voor het ontwerp van wind turbine rotor bladen. De sterkte- en stijfheidsafname van de composietmaterialen, veroorzaakt door vermoeiingsschade, kan de operationele levensduur beperken. Derhalve is een adequate beschrijving van vermoeiingsschade in composieten nodig voor het ontwerp van wind turbine rotor bladen.

Modellen die het vermoeiingsgedrag van composietmaterialen kunnen beschrijven kunnen verdeeld worden in drie categorieën: empirische, phenomenologische, en micro-mechanische modellen. Van deze modellen zijn alleen de micro-mechanische modellen gebaseerd op het berekenen van schade op het niveau van de bouwstenen van het composiet; de vezels en hars. Hiermee zijn deze methoden veelbelovend voor het voorspellen van het gedrag van composiet en het effect van veranderingen in materiaal- en laminaatsamenstelling, met relatief beperkte experimentele analyse van het uiteindelijke composiet, vergeleken met wat nodig is bij de modellen van de andere categorieën.

In deze dissertatie wordt een multi-scale micro-mechanisch model gepresenteerd dat het gebruik van empirische of fenomenologische factoren op composietlaminaat of constructieschaal vermijdt. Met dit model wordt het axiale trek-trek vermoeiingsgedrag van uni-directionele glasvezelversterkte composieten voorspeld, inclusief levensduur en stijfheidsafname. De invoerparameters van het model zijn beperkt tot vezel- en harseigenschappen en de berekeningsprocedure gebeurt via een geometrisch opschaalproces in 3 stappen:

1. Een kleine constructie bestaande uit enkele vezels ingebed in een hars wordt gemodelleerd als een *multi-fibre (MF) unit cell*. Het vermoeiingsgedrag van deze *unit cell* wordt gesimuleerd waarbij uitgegaan wordt dat opeenvolgende vezelbreuk het dominante faalmechanisme is. De uitvoer bestaat uit levensduurvoorspellingen en degradatie van de elastische eigenschappen.

2. Het vermoeiingsgedrag van een composiet op meso-schaal wordt ges-
imuleerd met de voorspellingen uit de *MF unit cell* als uitgangspunt.
Dit model wordt *meso-structure* (MS) model genoemd. Het MS model
wordt geanalyseerd met de eindige elementen methode, waarbij elk ele-
ment equivalent is aan een *MF unit cell*. De resultaten van deze analyse
zijn de vermoeiingslevensduren en degradatie van de elastische eigen-
schappen van de MS modellen.

3. Het vermoeiingsgedrag van composieten op macro-niveau wordt ges-
imuleerd met de MS model-eigenschappen als invoer. In dit numerieke
model wordt een deel van een testcoupon gesimuleerd en daarom wordt
het *Coupon-Size* (CS) model genoemd. Op zijn beurt is dit model opge-
bouwd uit MS elementen.

Bij opschalen verandert de helling van de SN-curve niet significant. De sprei-
ding in vermoeiingslevensduren wordt een aantal ordes van grootte kleiner,
en de curves die de stijfheidsafname beschrijven vertonen minder spreiding
en laten een sterker 'sudden-death' gedrag zien. Op ieder schaalniveau af-
zonderlijk is de stijfheidsafname lager en de spreiding in de stijfheidsafname
minder wanneer de helling parameter van de S-N curve wordt gereduceerd
van -10 tot -30. Dit interval voor de helling parameter omvat de mogelijke
waarden gebaseerd op de vermoeiingsdata van individuele vezels

Vergeleken met de experimentele resultaten van de proeven die in dit project
zijn uitgevoerd op unidirectionele composieten breedte-getailleerde proefs-
tukken, zijn de voorspelde levensduren een orde van grootte langer. Dit
is waarschijnlijk een gevolg van niet-gemodelleerde faalmechanismen, zoals
vezelonthechting. Desalniettemin komt de voorspelde stijfheidsafname overeen
met de experimentele observaties.

Glossary

List of Acronyms

2D	Two Dimensional
3D	Three Dimensional
cov	Coefficient of Variation
pdf	Probability Density Function
CFRP	Carbon Fibre Reinforced Polymer
CLD	Constant Life Diagram
CS	Coupon Size
DIC	Digital Image Correlation
ECN	Energy Research Centre of the Netherlands
FE	Finite Element
FRP	Fibre Reinforced Polymer
GFRP	Glass Fibre Reinforced Polymer
GLS	Global Load Sharing
ISS	Interface Shear Strength
LLS	Local Load Sharing
LR	Linear Regression
LRB	Likelihood Ratio Bounds
MF	Multi Fibre
MLE	Maximum Likelihood Estimation
MS	Meso Structure
RVE	Representative Volume Element
SCF	Maximum Stress Concentration
SEM	Scanning Electron Microscope
WMC	Knowledge Centre Wind turbine Materials and Constructions

List of symbols

Symbols used in chapter 2

β_e	Weibull shape parameter for tensile failure strains
β_H	Weibull shape parameter for high fibre tensile strengths
β_L	Weibull shape parameter for low fibre tensile strengths
β_M	Weibull shape parameter for middle fibre tensile strengths
β_S	Weibull shape parameter for tensile strengths
ϵ	fibre tensile failure strain
ϵ_0	Weibull scale parameter for tensile failure strains
ϵ_{avg}	average fibre tensile failure strain
ϵ_∞	axial tensile strain at the (infinite) fibre ends
γ	exponential parameter used in the weakest link theory
σ	axial tensile stress
σ_∞	axial tensile stress at the (infinite) fibre ends
σ_{0ref}	Weibull scale parameter for fibre tensile strengths with the reference length
σ_{0H}	Weibull scale parameter for high fibre tensile strengths
σ_{0L}	Weibull scale parameter for low fibre tensile strengths
σ_{0M}	Weibull scale parameter for middle fibre tensile strengths
σ_{eq}	equivalent tensile stress
σ_u	ultimate tensile strength
σ_L	transition point between low and middle fibre tensile strengths
σ_M	transition point between middle and high fibre tensile strengths
$\{\sigma^f\}$	stress components on fibres
$\{\sigma^m\}$	stress components on matrix
σ_t	fibre pull out strength
σ^1	first principle stress
σ^2	second principle stress
σ^3	third principle stress
τ	normalized fatigue life
ξ	normalized x
d_f	fibre diameter
l	actual fibre length
l_{em}	embedded fibre length
l_{ref}	reference fibre length
k	material parameter used in the critical element model

n	elapsed number of fatigue cycles
p	axial loads at the (infinite) each fibre
p_i	axial loads on the ith fibre
q	empirical parameter used to calculate σ_{eq}
r	number of broken fibres
s	centre-to-centre distance of fibres
u_i	axial displacement of the ith fibre
x	fibre orientation axis
$[A]$	6×6 bridging matrix relating the stress components on the fibres and matrix
A_f	fibre cross-sectional area
E_f	fibre Young's modulus
F_e	failure functions of the critical element
F_L	failure functions of a position far away to the incipient failure in the laminate
G_f	fibre shear modulus
G_m	matrix shear modulus
L_i	normalized load on the ith fibre
N	fatigue life
P_i	normalized p_i
S_a	applied stress on the critical element
S_u	ultimate strength on the critical element
S_L^r	composite residual strength
S_{Lu}^i	composite initial strength
U_i	normalized u_n
V_f	fibre volume fraction
V_i	normalized displacement on the ith fibre
V_m	matrix volume fraction

Symbols used in appendix A

α	Weibull scale parameter for the ratio $l_{seg,cr}/d$
β_e	Weibull shape parameter for tensile failure strains
β_i	Weibull shape parameter for fibre tensile failure strains in failure mode i
β_{seg}	Weibull shape parameter for fibre fragment lengths
β_{ld}	Weibull shape parameter for the ratio $l_{seg,cr}/d$
β_S	Weibull shape parameter for tensile strengths
ϵ	fibre tensile failure strain

ϵ_{0i}	Weibull scale parameter for fibre tensile failure strains in failure mode i
ϵ_{avg}	average fibre tensile failure strain
ϵ_r	fibre tensile failure strain with the maximum slack length
λ	fragment density of a fibre fragmentation specimen
λ_{max}	the maximum crack density of a fibre fragmentation specimen
ν_f	fibre Poisson's ratio
ν_m	matrix Poisson's ratio
σ	tensile strength
σ_0	Weibull scale parameter for tensile strengths
σ_{fc}	tensile strength of a fibre fragmentation specimen
σ_{max}	maximum tensile stress over an area with λ_{max}
σ_∞	tensile stress at the (infinite) fibre ends
τ	fibre/matrix interface shear stress
τ_{max}	fibre/matrix interface shear strength
ϕ	shear-lag parameter
c	weight factor in Okoroafor's model
d_f	fibre diameter
f	the product of $\epsilon \times P_s(\epsilon)$
g	probability density function of the slack lengths of fibres
l	actual fibre length
l_{em}	embedded fibre length
l_{ref}	reference fibre length
l_{seg}	fibre fragment length
$l_{seg,0}$	Weibull scale parameter for fibre fragment lengths
$l_{seg,avg}$	average fibre fragment length in a fibre fragmentation specimen at σ_{fc}
$l_{seg,cr}$	critical fibre fragment length
k	total number of fibre fragments in a fibre fragmentation specimen
m	fit parameter in Eq. A.26
n	total number of tests
n_f	total number of fibres of a fibre bundle
n_{seg}	total number of fibre fragments of a fibre fragmentation specimen
p_f	probability density function
r_f	fiber radius
r_m	matrix radius
s	centre-to-centre distance of fibres
u_{ep}	fibre indentation displacement due to fibre elastic-plastic deformation

u_f	fibre compressive displacement in a micro-indentation test
u_i	original indentation displacement in a micro-indentation test
A_f	fibre cross-sectional area
E_{cr}	the critical energy release rate to form a fibre debonding crack
E_f	fibre Young's modulus
E_m	matrix Young's modulus
F_{de}	fibre debonding force
F_{img}	imaginary load on a fibre bundle where no fibre is assumed broken
F_{in}	indented force in a micro-indentation test
$F_{in,cr}$	inflection point in the load-reduced displacement curve of a micro-indentation test
F_{real}	real load on a fibre bundle
G_m	matrix shear modulus
K	fit parameter in Eq. A.26
L	likelihood function
P	fibre failure probability
P_k	probability to have k fragments in a fibre fragmentation specimen
P_s	survival probability

Symbols used in the other chapters

β_e	Weibull shape parameter for tensile failure strains/equivalent strains
β_S	Weibull shape parameter for tensile strengths/equivalent strengths
β_N	Weibull shape parameter for fatigue lives
ϵ_0	Weibull scale parameter for tensile failure strains/equivalent strains
ϵ_{0ref}	Weibull scale parameter for tensile failure strains with the reference length
ϵ_{11}	axial strain
ϵ_{eq}	equivalent tensile failure strain calculated from the fatigue life
ϵ_{max}	maximum fatigue strain
ϵ_t	tensile failure strain
$\epsilon_{t,avg}$	average tensile failure strain
ζ	parameter in Halpin-Tsai's model
η	parameter in Halpin-Tsai's model

σ_0	Weibull scale parameter for tensile strengths/ equivalent strengths
σ_{11}	axial stress
σ_{max}	maximum fatigue stress
σ_{mean}	average fatigue stress
ν_f	fibre Poisson's ratio
ν_m	matrix Poisson's ratio
ν_{12}	composite Poisson's ratio (1-2 direction)
ν_{13}	composite Poisson's ratio (1-3 direction)
ν_{21}	composite Poisson's ratio (2-1 direction)
ν_{23}	composite Poisson's ratio (2-3 direction)
ν_{31}	composite Poisson's ratio (3-1 direction)
ν_{32}	composite Poisson's ratio (3-2 direction)
$\chi^2_{0.95,1}$	chi-squared statistic value with 95% probability and 1 degree of freedom
dx	x-directional nodal displacement
dy	y-directional nodal displacement
dz	z-directional nodal displacement
ds/dF	slope of the fibre displacement vs. load curve
err_{max}	the maximum fibre tensile failure strain measurement error
l	fibre length
l_{ref}	reference fibre length
m	number of fatigue loading blocks in a variable fatigue loading sequence
n	predefined fatigue cycles at a fatigue loading block
n_{fib}	required number of fibre tests for determination of tensile failure strains
s	standard deviation of fibre failure strains
$z_{0.45}$	the critical value corresponding to a 90% confidence interval
C_1	S-N slope parameter
C_2	strain based S-N intercept parameter
C_3	stress based S-N intercept parameter
D	damage factor
$D13$	composite dog-bone coupon geometry
E_f	fibre Young's modulus
E_m	matrix Young's modulus
E_{11}	composite longitudinal Young's modulus (equivalent to axial stiffness in this thesis)
E_{22}	composite transverse Young's modulus
E_{33}	composite through thickness Young's modulus
F_t	the load (force) to break a fibre in tension

G_{12} composite shear modulus (1-2 direction)
G_{13} composite shear modulus (1-3 direction)
G_{21} composite shear modulus (2-1 direction)
G_{23} composite shear modulus (2-3 direction)
G_{31} composite shear modulus (3-1 direction)
G_{32} composite shear modulus (3-2 direction)
$L(C_1)$ likelihood value for a trail C_1 value
$L(\hat{C}_1)$ the maximum likelihood estimator for C_1 parameter
N fatigue life
N_0 Weibull scale parameter for fatigue lives
N_{median} median of fatigue lives
N_{res} residual fatigue life
N_{seg} number of the fibre segments in a MF unit cell
P failure probability
V_f fibre volume fraction
V_m matrix volume fraction

Contents

List of Figures

List of Tables

Chapter 1

Introduction

In this thesis, a research project for predicting fatigue damage in wind turbine rotor blades using micro-mechanical methods is described. The project background is first described in Section 1.1, in which the problems encountered in composite fatigue modelling are particularly discussed. Following in Sections 1.2 and 1.3 are the motivation for the project and the purpose of this study. After that, Sections 1.4 and 1.5 give the approach and scope of a multi-scale micro-mechanical model developed to fulfill the research purpose. Finally, the thesis structure is shown in Section 1.6.

1.1 Background

In wind industry, the rotor blades are expected to work at least 20 years or up to 10^8-10^9 load cycles [13, 14]. During its service life, the rotor blade suffers from cyclic fatigue loads caused by the flapwise and edgewise bending moments, as shown in Figure 1.1 [1]. The flapwise bending moment is produced by the lift component perpendicular to the rotor plane. The edgewise bending moment is generated by the combination of the lift component in the rotor plane and the gravity on the blade. These two bending moments are cyclic, due to wind shear and blade rotation.

Wind turbine rotor blades are typically made out of glass or carbon fibre composite laminates, because of their excellent mechanical properties and low weight. A multitude of lay-ups and fibre orientations are used throughout
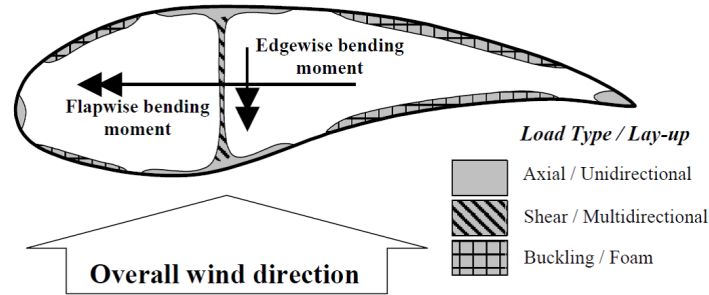
Figure 1.1: Cross-section of the wind turbine rotor blade (reproduced from [1])

the blade, tailored to local loads. In a common blade structure shown in Figure 1.1, the flapwise bending moments are carried by a beam like structure, the main spar, located at the largest thickness of the aerodynamic profile. This beam consists of laminates with high axial strength at the aerodynamic shell, separated by a web with high shear strength. To withstand the edgewise bending moments, axial reinforcements are placed near the leading and trailing edges of the blade.

Figure 1.2 shows 600 seconds of simulated flapwise and edgewise bending moments at the mid-point (30.6 m from the root) of a 61.5 m rotor blade. These signals were generated using the commercial design software FOCUS6 developed by Knowledge Centre Wind turbine Materials and Constructions (WMC) and Energy research Centre of the Netherlands (ECN) [15]. The characteristics of the flapwise and edgewise bending moments are:

1. The flapwise bending moment stays positive but varies stochastically in the mean value and amplitude, because of the stochastic wind speed as it flows past the wind turbine.

2. The edgewise bending moment appears periodic around a mean value near zero, because the bending moment is dominated by the gravity loads.

These loads characterise the resulting stresses in the main spar and the leading and trailing edges. Cyclic tensile and compressive stresses act on the main spar, depending on the side. In the leading and trailing edges, reversing stresses occur, going from tensile to compressive for each revolution of the rotor.

The wind turbine rotor blade fatigue design is based on experimental re-
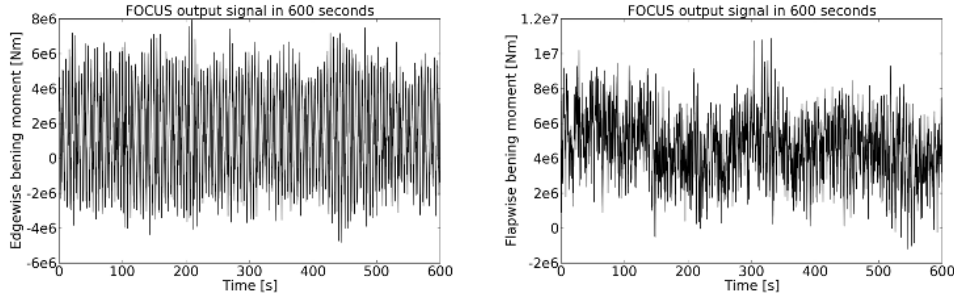
Figure 1.2: Simulated cyclic flapwise and edgewise bending moments at the mid-point of a rotor blade by using FOCUS6

sults from laboratory tests on composite coupons. For the fatigue design of the cross-section of the blade, a time series of fatigue stresses are calculated based on the spectrum flapwise, edgewise bending moments and the centrifugal load. By using the rainflow-counting method, this time series of fatigue stresses are converted to a spectrum load set [16]. Then, according to the Palmgren-Miner Rule [17] and Constant Life Diagram [18], the blade fatigue response (of that cross-section) can be designed from the experimental results of composite coupons. Here it is implicitly assumed that similar failure mechanisms exist in both the full-scale rotor blade and the laboratory coupons.

At the coupon level, the fatigue behaviour of composites has been studied intensely, by using empirical, phenomenological and micro-mechanical models (see Section 2.1). The empirical and phenomenological models describe the time to failure and sometimes macroscopic stiffness and strength degradation, but do not provide information on the micro-mechanical damage progression within the material. Ignorance of the micro-mechanical failure mechanisms brings the following limits.

1. The extraction of fatigue model parameters requires extensive experiments that are time-consuming.

2. The fatigue models typically describe constant amplitude behaviour of a limited number of material structures and configurations, and new parameters have to be re-extracted when any change is made in the material configuration.

The micro-mechanical models constitute novel approaches that aim to predict composite fatigue behaviour by studying interaction of failure mechanisms at

the fibre level. The ultimate goal of these models is to predict the composite fatigue behaviour, solely based on properties of composite constituents. However, the fatigue failure of composites is characterised by an interaction of many failure mechanisms and, therefore, capturing this in a model is a considerable challenge. The availability of micro-mechanical models is very limited, especially for fatigue models, and those that do exist still rely on empirical and phenomenological factors, for instance to describe the fatigue degradation of composite elastic constants. These parameters are obtained indirectly from experiments on composites instead of directly from tests on individual constituents, and therefore eliminate the main advantage of micro-mechanical models over phenomenological models.

1.2   Motivation

Although a large number of wind turbine blades in service show that reliable blades can be built with empirical and phenomenological models, these models have considerable drawbacks. Apart from the experimental effort involved and the fact that the tests only provide design data for a single fibre-matrix combination and lay-up, they do not provide any insight into underlying failure mechanisms. This limits the development and improvement of composites, for which insight in the failure mechanisms would provide valuable guidance.

As shown in Figure 1.1, different lay-ups of the above-mentioned composite laminates are distributed in a wind turbine rotor blade. Numerical experiments on composite laminates can assist in the selection of the optimal configuration of fabric architecture, fibre-resin combinations or even specimen geometry. Understanding the failure behaviour will improve knowledge of the limits of the materials. Therefore the development of a tool to perform numerical experiments on composite laminates will eventually improve the fatigue design of wind turbine rotor blades.

This thesis focuses on composites as used in wind turbine rotor blades. These composites differ from those used in e.g. aerospace industry because of different demands in terms of loads, reliability and cost. Notable characteristics of the wind turbine used composites are:

1. The diameter of fibres is usually large (up to ca. $17\mu m$).

2. Non-woven fabric is used in the lay-up of fabrics. That means the fibres are straight in the composite laminates, contrary to the undulated fibre bundles in woven fabric composites.

3. The composite laminates can be very thick (up to 100 layers or more)

In the main spar typically unidirectional glass fibre reinforced polymer (GFRP) composites are used as the stiffener materials to carry the axial normal stress imposed by the flapwise bending moment, as a result of which they are normally loaded under the cyclic tensile or compressive axial loading. Compared to the composite laminates with other lay-ups, unidirectional GFRP composites have a relatively simple structure. Micro-mechanical modelling of axial tension-tension fatigue behaviour of the unidirectional GFRP composites is performed in this thesis.

1.3 Purpose

The purpose of this study is to obtain a validated model for fatigue damage in wind turbine rotor blade laminates using micro-mechanical methods. According to the model, the composite fatigue lives and stiffness degradation will be predicted based on the material properties of (glass) fibres and polymer matrix.

1.4 Approach

A multi-scale fatigue model is developed to predict composite fatigue behaviour by using the properties of fibres and matrix via a scaling-up procedure. The scaling-up procedure consists of three steps, (a) Development of Multi-Fibre (MF) unit cells, (b) Development of Meso-Structure (MS) models and (c) Development of Coupon-Size (CS) models. At the lowest scale, the MF level, the fatigue behaviour is modelled using 3D unit cells, which are micro-structures of several fibres and surrounding matrix. For these unit cells the material properties of the constituents (fibres and matrix) are used as input, taking into account the stochastic strength properties of the fibres. At the next higher scale, the MS level, MF unit cells are used to predict the behaviour of multiple MF unit cells together. Finally the fatigue behaviour of composite coupons (CS level) is predicted by scaling up the MS modelling results. A chart describing this hierarchical flow is shown in Figure1.3.
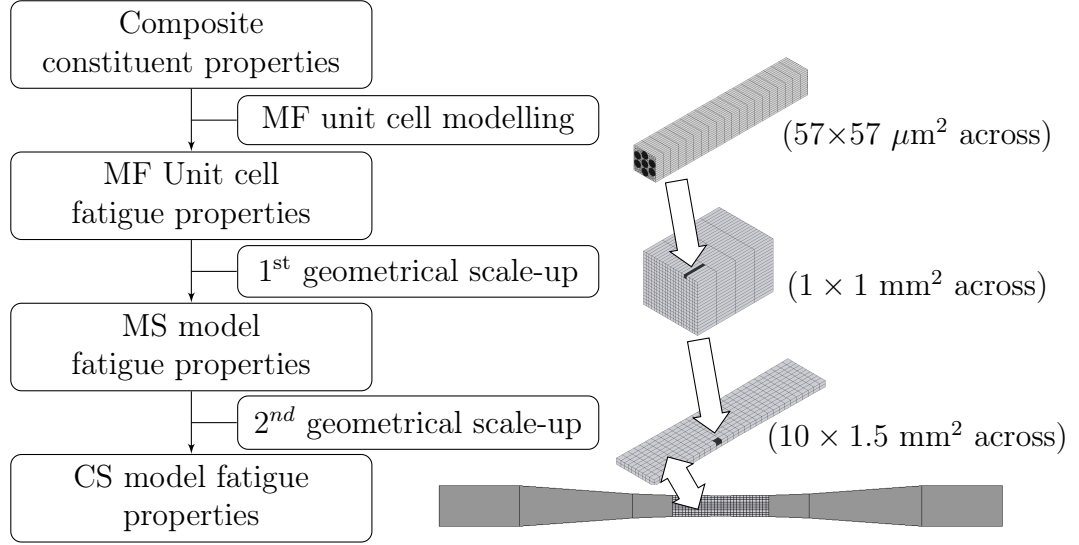
Figure 1.3: Flow chart of the multi-scale micro-mechanical fatigue modelling methodology

1.5   Scope

Due to the structural complexity, it is a huge amount of work to involve all possible micro-mechanical failures (see Section 2.2) in the fatigue model. Since fibres are the main constituents that bear loads, the proposed model is established by focusing on sequential fibre breakages (regarded as the dominant micro-mechanical failure) and the resulting matrix failures. The effect of fibre/matrix interface failure on composite fatigue behaviour is not discussed in this thesis. However, studying the fibre/matrix interface failure is vital for improving the prediction accuracy, and therefore is recommended for the next step in Section 7.2.

The proposed model is limited to predicting axial tension-tension fatigue behaviour of unidirectional composites. It will not work on composites under other fatigue loading conditions or with other configurations, due to the fact that sequential fibre breakage will not be the dominant fatigue failure mechanism any more.

Because glass and carbon fibres are characterized in the same technique, the proposed model is also suitable for unidirectional carbon fibre reinforced polymer (CFRP) composites.

1.6   Outline of the thesis

The thesis is organized in seven chapters. In this chapter, a brief introduction was given on the background and motivation of the project, the purpose of this study, and the approach and scope of the proposed multi-scale micro-mechanical fatigue model.

Chapter 2 reviews the state-of-the-art of micro-mechanical fatigue failure mechanisms including fibre breakage, matrix failures and fibre/matrix interface failures, and the micro-mechanical fatigue models. Considered as the dominant failure mechanism, the sequential fibre breakages are specially discussed to show the damage progression in the unidirectional GFRP composite materials under axial tensile loads. For the composite fatigue characterization, two kinds of micro-mechanical fatigue models for unidirectional GFRP composites are presented.

Chapter 3 reports the experimental work on the single glass fibres and unidirectional GFRP composite dog-bone coupons. The single fibre static and fatigue experiments are performed to provide inputs for the fatigue simulations of the MF unit cells. The fatigue experiments on the unidirectional GFRP dog-bone coupons are carried out to validate the proposed model. For the data analysis of these experimental results, the fatigue behaviour of the fibres and dog-bone coupons is characterized by three fatigue parameters.

From chapters 4 to 6, numerical fatigue simulations are performed on the MF unit cells, MS and CS models sequentially. The fatigue parameters and degradation curves of the composite elastic properties of the MF unit cells, MS and CS models are extracted to reveal the fatigue behaviour of the unidirectional GFRP composites at micro-, meso- and macro-scales. In Chapter 6, the final fatigue predictions on the unidirectional GFRP dog-bone coupons are obtained and compared to the experimental results.

Finally, the main conclusions and recommendations for future work are summarized in chapter 7.

This chapter includes the introduction of project background and motivation, the purpose of this study, and the approach and scope of the proposed multi-scale micro-mechanical fatigue model which is used to account for the fatigue damage in the unidirectional GFRP composites. The development of such a model requires a good knowledge of known micro-mechanical failure mechanisms and models, which are discussed in the next chapter.

Chapter 2

State of art

This chapter presents the literature study of micro-mechanical failure mechanisms and models. A general overview of the composites fatigue models is given in Section 2.1. Micro-mechanical models have an advantage regarding modelling of progressive failures compared to empirical and phenomenological models. The common micro-mechanical failure mechanisms are categorized into fibre breakage, matrix failure and fibre/matrix interface failure, and reviewed in Section 2.2. Since the fibres carry the vast majority of applied loads during fatigue, the influence factors on the sequential fibre breakages are of great interest to the micro-mechanical fatigue models. This part of the work is discussed in Section 2.3. Later in Section 2.4, two kinds of micro-mechanical fatigue models are presented based on the quantification of the relevant micro-mechanical failure mechanisms. The concluding remarks of this chapter are summarized in Section 2.5.

2.1   Fatigue models

In this thesis, fatigue models for Fibre Reinforced Polymer (FRP) composites are categorized into empirical models, phenomenological models and micro-mechanical models [19].

The empirical models are curve fitting models, and usually quite simple for the convenience of the model parameters extraction. The drawback is that these models do not consider any physical failure mechanisms. Accordingly,

they can only give fatigue life predictions of the composite coupons, but do not provide any detail of composite fatigue degradation.

Typical empirical fatigue characterisation methods are S-N curves, Constant Life Diagrams (CLD), etc. [1]. The S-N curve shows the fatigue life as a function of the fatigue loads (mostly the maximum fatigue stress or strain). The S-N curve is usually not directly used because it only gives information at a certain R ratio (the ratio between the minimum and maximum fatigue loads). To combine the S-N curves of different R ratios together, a CLD is plotted by connecting the fatigue load points subjected to the same fatigue life on the S-N curves of different R ratios. Figure 2.1 illustrates the relationship between the CLD and two constituent S-N curves of R ratios of -1 and 0.1 on both sides. Note that the y-axis of the S-N curves in Figure 2.1 is fatigue stress amplitude, on a linear scale in accordance with the y-axis of the CLD. In this case S-N data for nine different load ratios were used to construct this CLD. Commonly S-N data is available at only a few load ratios, resulting in a CLD with far less detail.
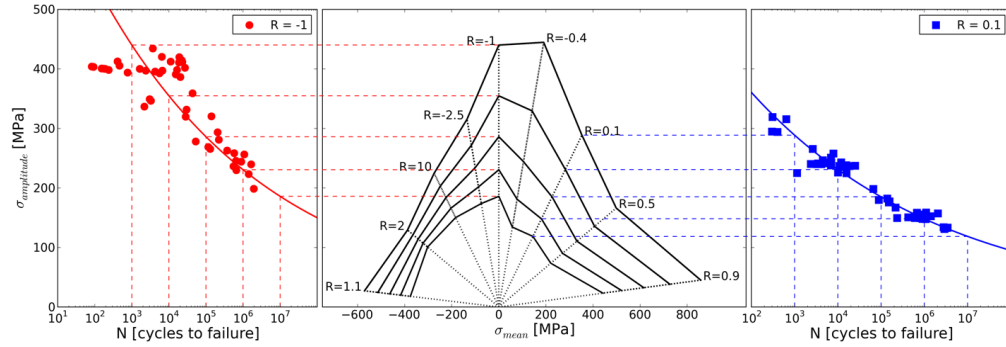
Figure 2.1: Illustration of the S-N curve and Constant Life Diagram

Phenomenological models [20, 21] attempt to describe the effect of fatigue damage evolution on material properties, such as stiffness degradation (Figure 2.2) and strength degradation (Figure 2.3). Figure 2.2 illustrates the normalized axial stiffness degradation of unidirectional GFRP composite dogbone coupons under tension-tension fatigue loads, tested in WMC's laboratory. The maximum fatigue stress was 390 MPa. The degraded stiffness was calculated from the axial strain measured using the Digital Image Correlation technique. On the x- and y- axes, the fatigue life and stiffness were normalized by the final fatigue life and initial stiffness respectively.

Figure 2.3 illustrates normalized residual strengths and fatigue data of $[90°/0°/\pm 45°/0°]_s$ GFRP composite dog-bone coupons under tension-tension fatigue loads [1]. The maximum fatigue stress was 380 MPa. The strength residual data were also combined with the tensile strengths and fatigue lives of the composite coupons to indicate the beginning and end of the residual strength degradation. On the x- and y- axes, the fatigue life and strength were normalized by the average values of the fatigue lives (subjected to the maximum fatigue stress of 380 MPa) and tensile strengths respectively.
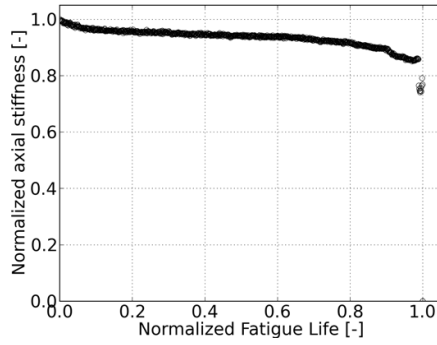
Figure 2.2:   Composite   stiffness   degradation
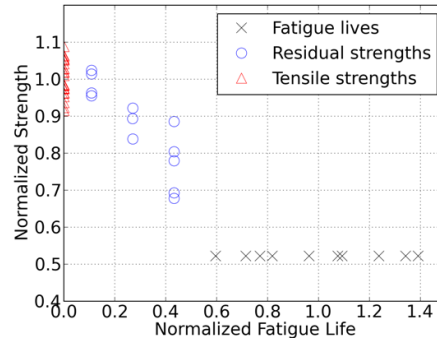
Figure 2.3:   Composite   strength   degradation (reproduced from [1])

The degradation of composite stiffness or strength is usually modelled by the failure accumulation which is not based on physical considerations. Another problem of strength degradation models is that the experimental determination of composite strength is obtained from a batch of composite coupons. Due to random flaw distribution and fatigue failure accumulation, the degraded strengths of the composite coupons subjected to the same fatigue loading show significant variation. Thus, the accuracy of strength degradation model parameters depends on the scatter of degraded strengths of composite coupons.

Compared to the empirical and phenomenological models, micro-mechanical models [7, 22–48] have potential advantages on interpreting progressive failures and saving test effort. The micro-mechanical model is an approach working at predicting composite properties by modelling microscopic failures that occurred on fibres, matrix and fibre/matrix interface (or interphase). For instance, the fatigue damage in unidirectional composites is caused by a synergistic interaction of fibre breakage, matrix failure and fibre debond-

ing, depending on the constituent properties, geometries, applied boundary conditions, etc.

The difficulty in micro-mechanical modelling on a coupon-size composite specimen is that the overall microscopic failure is very complex, since many thousands of fibres are involved. Due to computational limitations, numerical investigations can only be directly carried out on a microscopic composite structure up to a small number of fibres, for instance by using shear-lag models or finite element simulations [49–54]. The significance of these studies is to approximately account for the influence of certain micro-mechanical failure mechanisms on composite static behaviour. For predictions of large composite structures, a trade-off to minimize the model complexity has to be made by introducing some empirical or phenomenological factors (see Section 2.4).

In the micro-mechanical models for large composite structures, the anisotropic or orthotropic composite properties are modelled by unit cells, which are also called Representative Volume Elements or RVEs. Traditionally the unit cell is regarded as the smallest cell whose properties are equivalent to those of the composite (implicitly ignoring scale effects). Depending on the failure mechanisms of interest, different structures could be selected for the unit cell. For unidirectional composites, the most simple unit cell only consists of one fibre and surrounding matrix, and is limited to the failure mechanisms where no interaction between fibres occurs. The application of the one-fibre unit cells is frequently found in the models such as Micro-mechanical Homogenization [32], etc.

2.2   Microscopic failure mechanisms

During fatigue tests, the composite fatigue progressive failures initiate randomly at the weakest locations of the fibres, matrix and fibre/matrix interface. Therefore, the initiation of the microscopic failures should be understood before building up the micro-mechanical models. A large amount of literature has been published on the extraction of fibre properties and fibre/matrix interface properties. A survey of those approaches is given in Appendix A. In addition to the above two resources, failure may also stem from the manufacturing imperfections in matrix such as matrix voids.

A fatigue life diagram of unidirectional FRP materials proposed by Talreja is illustrated in Figure 2.4 [2]. Talreja's fatigue diagram consists of three regions, under different dominant fatigue failure mechanisms.
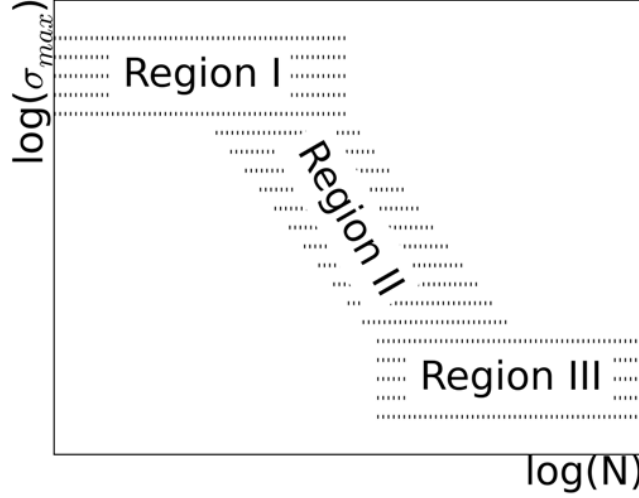
Figure 2.4: Three fatigue life regions defined by Talreja [2]

For unidirectional composites under tension-tension fatigue loads, in region I, the maximum fatigue load is large enough to break a critical number of fibres simultaneously. The resulting load-redistribution causes an overwhelming failure of all surviving fibres. In region II, the applied fatigue loads are reduced below the criterion that triggers the critical sequential fibre breakages. As a result, failures stemming from fibre/matrix interface and matrix become more significant. The composite fatigue life is longer because of the lower breaking rate of the supporting fibres. As the fatigue loads are further reduced to the region III, the composite fatigue life is not experimentally detectable any more. Therefore the composite is assumed to not fail by fatigue at least for the number of cycles that is practically reproducible in the laboratory or in service.

It has been noted that the existence of Region III is disputed, since for some composite materials the starting point of Region III is far more than the upper limit where the fatigue life can be measured. For instance, van Delft et al. observed that the power-law S-N curve is still valid to describe the fatigue behaviour of multi-directional GFRP composites up to 10^9 cycles [55].

2.2.1 Fibre breakage

Glass fibres exhibit statistically distributed strengths due to the superficial (and internal) statistically distributed micro-flaws, rather than the failure of chemical bonds [56, 57]. If a fibre fails by the rupture of chemical bonds (e.g. Si-O bond), the theoretical strength is approximately 10000 MPa [58]. However, although glass fibres show a much higher tensile strength compared to bulk glass products, the maximum fibre strength is still considerably lower than the theoretical strength.

Ladevéze and Genet [3] illustrated surface crack growth of single glass fibres by a post-mortem SEM picture, and claimed that a fibre fails when a critical crack length is formed, as shown in Figure 2.5.

(a) SEM picture   (b) Illustration
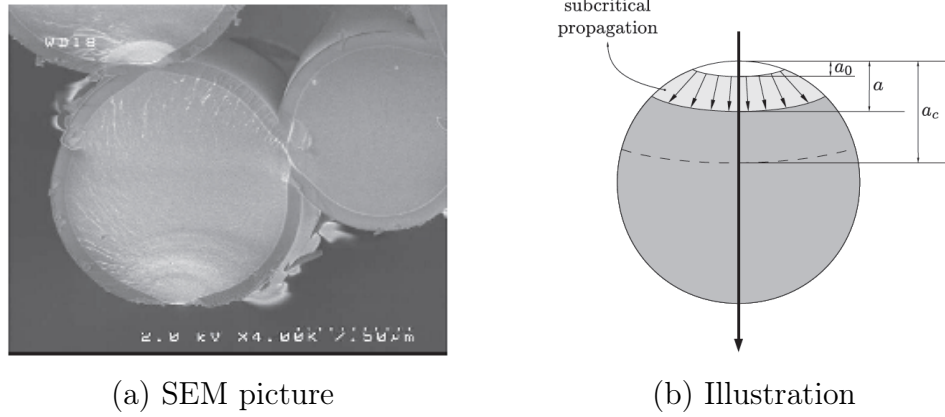
Figure 2.5: Superficial crack propagation on fibre cross-section (reproduced from [3])

Commonly, a two-parameter Weibull distribution modified by the weakest link theory is used to characterize the fibre tensile strengths (or failure strains), that is in Eq. 2.1 [59–62].

$$P(\sigma) = 1 - \exp\{-\frac{l}{l_{ref}}(\frac{\sigma}{\sigma_{0ref}})^{\beta_S}\} \tag{2.1}$$

in which P is fibre failure probability of tensile strength σ (or less), l is the fibre actual length while l_{ref} is the fibre reference length where the Weibull shape β_S and scale parameters σ_{0ref} are extracted from experimental results. The β_S parameter indicates the scatter of fibre tensile strengths. The effect

of β_S on the strength probabilities of fibres (when $l = l_{ref}$) is illustrated in Figure 2.6, in which the β_S values span the range from 4.0 to 10.0 covering a realistic range of β_S values of glass fibres while the σ_{0ref} is set to 2000 MPa.
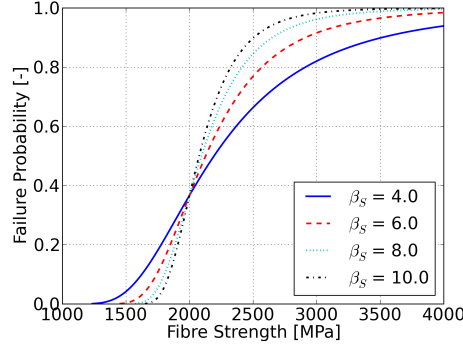
Figure 2.6: Illustration of fibre strength probabilities with different β parameters

For bulk glass (large scale structures), Jayatilaka and Trustrum [57] built up the correlations between the inner/superficial crack distribution and glass tensile strength distribution using the strain energy theory. They found that the Weibull form of the strength distribution can be related to the flaws distribution by assuming the flaw length to follow a Gamma distribution and the flaw angle to follow a uniform distribution. The Weibull shape parameter of the glass tensile strength is inversely proportional to the variability of the inner crack lengths. Therefore, a wider distribution of crack lengths gives rise to a smaller Weibull shape parameter (corresponding to a larger scatter) of glass strengths.

In many cases, the length effect on fibre tensile strength cannot be accurately described by the linear ratio l/l_{ref}, because of the fibre diameter variation [63] or the stress concentration at the clamped ends [64]. Taking these factors into account, Eq. 2.2 is modified to

$$P(\sigma) = 1 - \exp\{-(\frac{l}{l_{ref}})^{\gamma}(\frac{\sigma}{\sigma_{0ref}})^{\beta_S}\} \tag{2.2}$$

in which, γ is an exponential parameter ranging from 0 to 1, which is determined experimentally. If γ equals to 1, Eq. 2.2 reduces to Eq. 2.1, whereas if γ equals to 0, it means the fibre strength distribution does not exhibit a length effect.

Eq. 2.1 or Eq. 2.2 indicates longer fibres have lower tensile strength, and vice versa. However, in reality, the fibre tensile strength cannot be infinitely increased, as Eq. 2.1 or Eq. 2.2 implies if the length L approaches 0, due to the finite strength of chemical bonds. In other words, there should be a lower limit of the length of validity of Eq. 2.1 or Eq. 2.2. Unfortunately, so far it has been not been possible to determine this limit. Thomason [65] studied the strength of fibres with very short lengths (180 to 380 μm) and found that an increasing tendency of fibre strength still exists with the reduction of the fibre length.

It has been noted that the fibre tensile strengths are not always modelled in a uni-modal Weibull form (shown in Eq. 2.1 or Eq. 2.2) but a multi-modal Weibull form. This is because the trends in failure probabilities might be different with typical strength intervals. Wu and Robinson proposed a tri-Weibull distribution function Eq. 2.3 to describe the stepwise relationship between the failure probabilities and fibre tensile strength in the low, middle and high strength regions [66].

$$P(\sigma) = \begin{cases} 1 - \exp[-(\frac{\sigma}{\sigma_{0L}})^{\beta_L}] & \text{when } 0 \leq \sigma \leq \sigma_L \\ 1 - \exp[-(\frac{\sigma}{\sigma_{0M}})^{\beta_M}] & \text{when } \sigma_L \leq \sigma \leq \sigma_M \\ 1 - \exp[-(\frac{\sigma}{\sigma_{0H}})^{\beta_H}] & \text{when } \sigma_M \leq \sigma \leq \infty \end{cases} \qquad (2.3)$$

in which β_L and σ_{0L}, β_M and σ_{0M}, β_H and σ_{0H} are Weibull parameters for fibre tensile strengths corresponding to the low, middle and high strength region respectively. σ_L and σ_M are transitions between these different strength regions. However, Eq. 2.3 does not involve the length effect on fibre tensile strengths. It is uncertain whether the σ_L and σ_M can be modelled explicitly as a function of fibre gauge lengths. Therefore, unless there is a large difference between the Weibull parameters for different strength regions, Eq. 2.1 or Eq. 2.2 is regarded still efficient to describe the fibre tensile strengths over a certain gauge length range.

The experimental data for cyclic loading fatigue of glass fibres is very limited. One can assume that fibre fatigue damage is caused by the propagation of micro-flaws existing in fibres. Gupta [67] studied the static fatigue life prediction of high strength (bulk) glass materials and found that the power law equation can give a versatile and reasonably good prediction of all the data in which the crack growth rate was from 10^{-16} m/s to 10^{-4} m/s.

Studies of fibre static fatigue (creep) tests show a range of slope values of the fibre S-N curves spanning from -20 to -30 for E-glass fibres [68, 69]. The main problem of the S-N slope extraction of single fibres is that large scatter

is expected because of the wide distribution of micro-flaws. Kurkjian [69] carried out fibre creep tests and found that for silica glass fibres, the time to failure spans about a factor of 1000.

It has to be mentioned that all above-mentioned analyses on fibre static and fatigue properties were limited to room temperature (i.e. ca. 23°C). Fibre properties are also significantly affected by environmental conditions such as temperature, moisture, etc. Since in FRP composites, the polymer matrix provides good protection of fibres from the severe environmental conditions, the environmental effect on fibre properties is not considered during composite fatigue tests. The relevant studies of environment effect on fibre properties can be found in the work of Wiederhorn [70,71], Armstrong [72], Mrotek [73] and Pierre [74].

2.2.2   Matrix failure

Polymer matrix is used to constrain the fibres in a fixed alignment. For unidirectional composites under axial tensile loads, the matrix only carries a small part of the loads. Its main functionality is to transfer the normal stress in fibres, for instance from the broken fibres to the neighbouring intact fibres within a limited distance (called "ineffective length", see Section 2.3). Generally, according to Eq. 2.4 shown below in Section 2.3, a high matrix stiffness causes the fibre-to-fibre load redistribution in a small region, but a high stress concentration to the neighbouring fibres. When failures occur in the matrix, the load redistribution rule will be correspondingly changed, leading to a different fatigue response of the composites.

How matrix failures develop within a composite is influenced by the matrix viscoelasticity. According to the study by Zhang and Hartwig [75], composites with a brittle matrix (for instance, epoxy) show longer fatigue lives compared to those with a ductile matrix (for instance, PEEK) under the same fatigue loads, even though the matrices exhibit similar stiffness. This is because more matrix micro-cracks are initialized in the brittle matrix during a fatigue test. The initialization of these micro-cracks contributes to energy dissipation and therefore decreases the Stress Concentration Factors (SCFs) caused by fibre breakages. That means in brittle matrix composites the fibre breaking rate is slower and the final composite failure is delayed.

The frequency effect on the fatigue behaviour of composites is another consequence of the matrix viscoelasticity. The relationship between the testing

frequency and composite fatigue life is affected by the heat dissipation, which is related to the testing frequency in turn (by matrix viscoelastic damping). At low frequencies (no heat dissipation), the fatigue life increases as the frequency increases, but at high frequencies (obvious heat dissipation), the fatigue life decreases as the frequency increases [76]. Mishnaevsky and Brøndsted [52] developed a kinetics-based model to predict the influence of frequency on composite fatigue lives with respect to different loading histories. In their models, a linear damage accumulation law is assumed during every fatigue cycle. The model predictions show that composite fatigue lives are almost linearly increased with the testing frequencies.

Despite the above discussions, due to the fact that the fibres constrain the movement of its chemical chains, the matrix probably exhibits more elastic behaviour. Thus the effect of the matrix viscoelasticity on composite fatigue behaviour is less significant. At the current stage, the matrix is still assumed to exhibit pure elastic behaviour in the proposed multi-scale micro-mechanical model.

2.2.3   Fibre/matrix interface failures

Glass fibres are coated by a sizing material to improve the adhesion between fibres and matrix, and prevent the damage from fibre-fibre contact in fabrication. The sizing material is a complicated chemical mixture made up of 5-10 wt% lubricants, 80-90 wt% film formers and 5-10 wt% coupling agents, and takes 0.2-2 wt% of glass fibres [77, 78]. The fibre/matrix interface (or interphase) is formed by the mixture of fibre sizing materials and polymer matrix and can be regarded as a "constituent" of the unidirectional composites [4, 77–82] . The fibre/matrix interface shear strength (ISS) is in direct proportion to the compatibility between fibre sizing materials and matrix [79].

Zinck et al. [4] found that the coupling agents in the sizing materials can fix fibre superficial flaws. They compared the tensile strength distribution of glass fibres with different surface treatments, and concluded that the use of organosilane coupling agents increases the average fibre strength by approximately 15%. The scatter of fibre strength was not significantly changed. Zinck argued the sizing materials can only fill up but not fully cover the fibre superficial flaws, as illustrated in Figure 2.7. Therefore, the flaw distribution stayed the same.
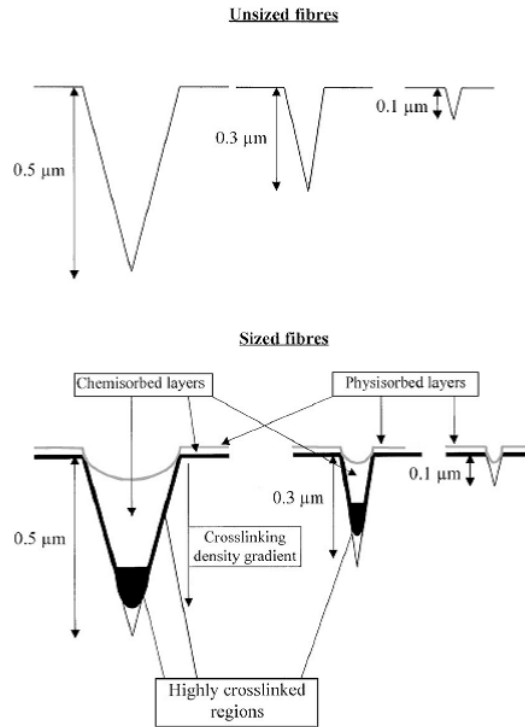
Figure 2.7: Illustration of covering fibre superficial flaws by sizing materials (reproduced from [4])

Sjögren et al. [5] studied the growth of the crack initialized from a fibre break-age. Depending on the strength of the fibre/matrix interface, this crack may grow parallel to the fibre on its surface (Figure 2.8a) when the fibre/matrix interface is weak, or perpendicular to it (Figure 2.8b) when the fibre/matrix interface is strong. For most commercial GFRP composite materials, Sjögren indicated that, even through the glass fibres surface is coated by sizing materials, the fibre/matrix interface is still not strong enough to initialize the matrix cracking [5].

In axial tension-tension fatigue tests on unidirectional FRP composites, Pupurs and Varna [6] pointed out that fibre debonding (namely the fibre/matrix interface failure along the fibre surface) is created by either fibre breakages for the high applied loads or matrix failure propagation for the low applied loads, as illustrated in Figure 2.9. The failure mechanism depends on the Mode II strain energy release rate. For fibre debonding caused by fibre breakages, they derived both analytical expressions and finite element simulations to predict the fibre debonding growth.

(a) Weak interface   (b) Strong interface
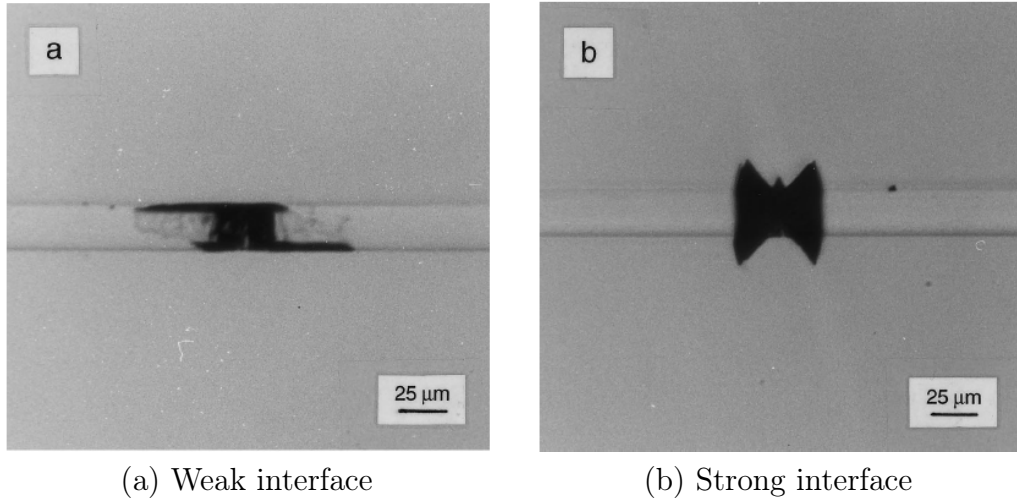
Figure 2.8: Fibre/matrix interface failure due to the fibre breakage (reproduced from [5])
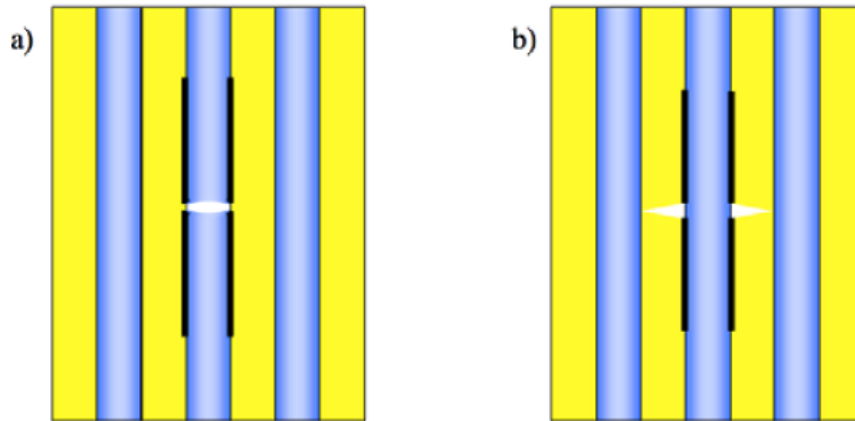
(a) Subjected to high fatigue loading (b) Subjected to low fatigue loading

Figure 2.9: Illustrations of fibre debonding initiation (reproduced from [6])

Van den Oever and Peijs [83] compared the axial tension-tension fatigue properties of unidirectional GFRP composites with strong and weak fibre/matrix interface. They found that if there is no fibre debonding in the composites, the axial Young's modulus of the composite follows a more sudden-death shaped degradation curve. Otherwise, the axial Young's modulus follows a gradual degradation curve.

2.3   Sequential fibre breakages

In unidirectional FRP composites under axial loads, fibres are the major components to bear the applied loads. Fibres will not break all at the same time because of their distributed strength, both from fibre to fibre and along the fibres. Thus, the investigation of fatigue damage evolution can be related to the study of a sequential fibre breakages failure mechanism.

After the breaking of weak fibres, the composite stress/strain state adjacent to the fibre breaking points is changed. The axial normal loads of broken fibres near the breaking point are transferred to other surviving fibres. Either a Global Load Sharing (GLS) load redistribution rule or a Local Load Sharing (LLS) load redistribution rule is used to reveal this natural load transfer. The difference between GLS or LLS is that, the axial normal loads are transferred evenly over all other surviving fibres or locally to the neighbouring surviving fibres with decreasing transferred loads to the further ones away from the broken fibre. GLS is usually used in ceramic or metal matrix composites, where the stiffness of the matrix is comparable with that of the reinforcing fibres [25, 84], whereas LLS is found more fit to FRP composites.

In Harlow and Phoenix's studies [29, 30], LLS is simply performed by transferring the axial normal loads of the broken fibres to the nearest neighbouring fibres. Later on, the shear-lag models are used to predict LLS by assuming the load transfer is actually done by matrix shear between broken fibres and the neighbouring intact fibres. In the shear-lag model, fibres are assumed to carry all axial normal loads. Therefore, the shear-lag model works better in cases where the stiffness of the matrix is much lower than that of fibers, corresponding to the characteristics of most FRP composites. Furthermore, the accuracy of the shear-lag model goes down with the decrease in the fibre volume fraction, since the matrix carries more load.

By studying the effect of the fibre orientation on the stiffness and strength of paper and other fibrous materials, Cox [85] developed a complicated formula to calculate the stress state of the infinitely long fibres embedded in a matrix with random orientations. For a special case that a single fibre of length l is embedded in a matrix subjected to a constant strain ϵ_∞ in fibre orientation, the stress state of the fibre is shown in Eq. 2.4.

$$\sigma(x) = \sigma_\infty \{1 - \frac{\cosh\left[\psi(l/2 - x)\right]}{\cosh\left[\psi l/2\right]}\}, \ \psi = \{\frac{G_f}{E_f}[\frac{2\pi}{A_f \ln\left(2s/d_f\right)}]\}^{1/2} \qquad (2.4)$$

in which σ_∞ is the applied stress at the fibre ends (i.e. $\sigma_\infty = E_f \times \epsilon_\infty$), A_f is the fibre cross-sectional area, E_f and G_f are the fibre Young's and shear moduli, s is the centre-to-centre distance of fibres and d_f is the fibre diameter.

Later on, to account for the axial loads redistribution in between fibres, Hedgepeth [86] developed a 2D shear-lag model for a planar fibrous composite under constant tensile loads on both ends, based on a dimensionless governing equilibrium equation Eq. 2.5 of fibre axial displacement.

$$\frac{\partial^2 U_i}{\partial \xi^2} + U_{i+1} - 2U_i + U_{i+1} = 0 \tag{2.5}$$

with the conditions

$$p_i = pP_i, \; u_i = p\sqrt{\frac{sU_i}{E_f A_f G_m d_f}} \text{ and } x = \sqrt{\frac{E_f A_f s\xi}{G_m d_f}}$$

in which i is the fibre rank id i^{th}, p_i is the axial load on i^{th} fibre, p is axial load at the infinite ends of each fibre, P_i, U_i, ξ are normalized variables, u_i is the axial displacement of the ith fibre, s is the centre-to-centre distance of fibres and x is the fibre orientation coordinate. Furthermore, $E_f A_f$ indicates the fibre tensile stiffness, and $G_m d_f$ indicates the matrix shear stiffness. Solution of Eq. 2.5 subjected to certain boundary conditions gives the stress state on the fibre bundle. For a specific circumstance of continuous fibre breakages (all broken fibres are in a cluster which does not contain any intact fibres), as described by Eq. 2.6 where r is the number of broken fibres, the numerical solution of Eq. 2.5 can be obtained by a two-step procedure.

$$P_i(0) = 0 \text{ where } 0 \leq i \leq r - 1 \text{ and } U_i(0) = 0 \text{ where for other fibres} \tag{2.6}$$

Firstly, an auxiliary function (also called influence function) Eq. 2.7 is introduced, with respect to boundary conditions Eq. 2.8 where no remote load is applied on the fibre bundle and only 1 fibre (for instance the 0th fibre) breaks when a unit displacement is applied, is solved using the Fourier transform method. Note that the boundary conditions for this case are different from Eq. 2.6.

$$\frac{\partial^2 V_i}{\partial \xi^2} + V_{i+1} - 2V_i + V_{i+1} = 0 \tag{2.7}$$

$P_i(0) = 0$ where $i = 0$ and $V_i(0) = 0$ where for other fibres   (2.8)

Then, the solutions of Eq. 2.5 are obtained by using superposition on all influence functions from 0th to $(r-1)^{th}$ broken fibres, as shown in Eqs. 2.9 and 2.10.

$$P_i(\xi) = 1 + \sum_{m=0}^{r-1} L_{i-m}(\xi) U_m(0)$$ (2.9)

$$U_i(\xi) = \xi + \sum_{m=0}^{r-1} V_{i-m}(\xi) U_m(0)$$ (2.10)

in which, L_i and V_i indicate the applied load and displacement at axial length ξ of the ith fibre in the influence function.

Eqs. 2.9 and 2.10 imply that most of the axial loads are transferred to the nearest neighbouring fibres of the continuous fibre breakage crack. On the broken fibres, the applied loads are gradually recovered from the breaking point within a certain length, known as characteristic load transfer length [87] or ineffective length [88]. For the fibres bearing the transferred loads, the axial tensile loads gradually attenuate to the boundary loads within the ineffective length.

The experimental technique to evaluate the ineffective length is the Laser Raman Spectroscopy technique [89, 90]. Anagnostopoulos et al. [90] measured the ineffective lengths in unidirectional aramid fibre reinforced epoxy composites subjected to different applied loads. According to their observations, the load recovery can be fitted by an exponential function, and the ineffective length is increased with the rise of applied strain levels. Anagnostopoulos also found that the fibre/matrix Interface Shear Strength (ISS) significantly deviates from Cox shear lag model predictions when high strain levels are applied. They attributed this discrepancy to a severe matrix shear modulus decrease caused by (high) residual thermal stresses.

Hedgepeth's model can only deal with 2D transverse continuous fibre breakages (on the same locations along their length). Satry and Phoenix [91] generalized Hedgepeth model to randomly distributed fibre breakages by using a Break-Influence Superposition (BIS) technique. The idea of the BIS technique is that, the transferred loads and resulting displacements of all surviving fibres due to every fibre breakage are independent of each other. In other

words, for a surviving fibre, the final stress state can be calculated by summing up the stress state induced by every single fibre breakage. Hedgepeth model can be regarded as a particular application of the BIS technique. According to the calculations by the BIS technique, the maximum transferred loads to the most two neighbouring fibres next to the transversely continuous fibre breakages are obviously reduced if the fibre breaking locations are unevenly distributed.

In general, the maximum Stress Concentration Factor (SCF) induced by a broken fibre predicted by the Hedgepeth and Satry models is approximately 1.333, which is higher than the range from 1.04 to 1.10 obtained from some numerical simulation results [92–97]. This is because of the rigid assumptions used in these models, namely:

1. Fibres are evenly aligned in an infinite 2D line.

2. The matrix has pure elastic properties and only carries shear load.

3. The fibre/matrix interface is made up by a perfect bond

Hedgepeth and van Dyke [98] developed a 3D model (hereby called HVD model) in which the influence fibres are enlarged to four nearest neighbouring fibres for a square fibre array or six nearest neighbouring fibres for a hexagonal fibre array. Later on, Landis et al. [99] pointed out that the HVD model still underestimates the transferred loads on the second nearest neighbouring fibres, and therefore predicts higher SCFs on the nearest neighbouring fibres but lower SCFs on the second nearest fibres. They generalized the HVD model to a more complex equation to further reduce the maximum SCF.

In the same paper, Hedgepeth and van Dyke [98] also took matrix shear yielding into account in the Hedgepeth model Eq. 2.5. They found that matrix yielding will limit the transferred shear stress and then diminish the maximum SCF. This resultant maximum SCF reduction becomes gradual as the ratio, between the applied load at far-away ends and the required load at far-away ends to cause the matrix to yield, increases.

Furthermore, fibre debonding and matrix cracking stemming from fibre/matrix interface failure are important failure mechanisms that alter the load transfer rules from broken fibres to intact fibres. Ochiai et al [100] studied the influence of fibre debonding and matrix cracking on the SCF calculations. They concluded that the calculated SCFs are decreased by fibre debonding, but increased by matrix cracking around the broken fibre.

However, Beyerlein and Phoenix [87] pointed out that fibre debonding is still negative for unidirectional FRP composites although it diminishes the SCF associated with fibre breakages. When a fibre starts to debond, the original interfacial shear stress along the fibres is replaced by the relatively lower friction loads in the debonding area. For this reason, the ineffective length for the load recovery of the broken fibres and load transfer of the neighbouring intact fibres is extended. The failure probabilities of the neighbouring intact fibres are then increased. This negative influence can be eased by a higher friction loads resulting from the fibre debonding.

Goda and Phoenix [49] performed Monte-Carlo simulations on the shear lag model considering the fibre debonding . They found that the CFRP composite specimens containing debonded fibres exhibit low average strength with a large variance compared to the non-debonding specimens. And as expected, higher average and lower variance of composite strengths can be obtained by increasing the friction loads in the fibre debonding region.

Landis and McMeeking [101] discussed the influences of debonding, axial matrix stiffness, and uneven fibre spacing on the maximum SCF calculations in 3D fibre array structures. They claimed that when a single fibre is broken, fibre debonding or increased axial matrix stiffness with well bonded fibre/matrix interface reduces the maximum SCF of the surrounding fibres. If the fibres are distributed unevenly, the maximum SCF will be higher for fibres that are close together.

2.4   Micro-mechanical fatigue models

Analytical micro-mechanical fatigue models are primarily developed to calculate the degradation of composite material properties as a function of localized failure events. In these models, only properties of the critical element (that causes final failure of the composite specimen) are of interest. Thus they are called critical element models.

The rapid development of modern computational technique allows modelling of the competitive microscopic failure mechanisms. For complex models, it is very difficult to obtain analytical expressions for the damage factor calculation in the critical element models. In these cases, the finite element model will be a good alternative.

The detailed introduction and application of critical element models and finite element models are given in Sections 2.4.1 and 2.4.2.

2.4.1   Critical element models

The critical element modelling concept was first developed by Reifsnider [33] to model FRP composite fatigue behaviour by reducing the structural complexity. Reifsnider suggested a composite specimen is made up of the critical element and sub-critical elements, and the composite failure is caused only by the failure of the critical element. The following assumptions are also used:

1. The composite failure is immediately caused by the failure of the critical element due to a dominant progressive failure mechanism. Therefore, the critical element should be large enough to trigger the catastrophic failure of a composite structure. For instance, for a multi-layer composite laminate subjected to axial tension fatigue loading, a unidirectional ply can be regarded as the critical element;

2. In the sub-critical elements, fatigue degrades the material stiffness but does not lead to the final failure of the composite;

3. During the fatigue test, the applied loads on the critical elements are changing continuously, depending on the stiffness degradation in the critical element and sub-critical elements.

The model outputs are the predictions on composite fatigue lives and strength or stiffness degradation curves.

A general equation to describe the composite strength degradation developed by Reifsnider is shown in Eq. 2.11 [33].

$$\frac{S_L^r(\tau_1)}{S_{Lu}^i} = [\frac{F_e(0)/F_L(0)}{F_e(\tau_1)/F_L(\tau_1)}]rv\{1 - \int_0^{\tau_1}[1 - F_e(\tau)]k\tau^{(k-1)}\mathrm{d}\tau \tag{2.11}$$

in which S_L^r and S_{Lu}^i are residual and initial (ultimate) strengths of the composite specimen, F_e is the failure function of the critical element under the dominant progressive failure mechanism, F_L is the failure function of a far-away position to the incipient failure in the laminate, subscript rv in brackets indicates the SCF (i.e. F_e/F_L) and is calculated from the RVE, τ is the normalized fatigue life defined by the ratio between the elapsed number

of cycles and total number of cycles (i.e. n/N), τ_1 corresponds to the τ value where the degraded strength is calculated, and k is a material parameter. For all τ, if it is assumed that F_e equals to F_L (i.e. uniform stress state over the critical element) and the failure function F is independent of τ (i.e. no load transfer from sub-critical elements to the critical element), Eq. 2.11 can be reduced to a commonly used phenomenological strength degradation function Eq. 2.12.

$$\frac{S_L^r}{S_{Lu}} = 1 - (1 - \frac{S_a}{S^u})(\frac{n}{N})^k \tag{2.12}$$

In Eq 2.12, no stress concentration is considered. Then, the critical element failure can be simply calculated by S_a/S_u, in which S_a and S_u are the applied and ultimate stresses on the critical element.

Reifsnider argued that an analytical calculation of failure function F_e depends on several factors such as the 3D stress state of the critical element, non-uniform applied stress due to the corresponding failure mechanisms and statistical properties of constituents. The consideration of any of the above effects will bring tremendous complexity into the F_e calculation.

In order to simplify the F_e calculation, semi-empirical damage evolution models of the critical and sub-critical elements are employed. For instance, Noll et al. [40] developed a critical element model to predict the fatigue lives of multidirectional CFRP composite specimens under tension-tension fatigue loads. The S-N curve, strength degradation model of the critical elements (0° plies), and stiffness degradation model and delamination model for the sub-critical elements (off-axis plies) were prepared in advance for calculating damage factors of the critical elements. Their model gives reasonable fatigue life predictions by considering a non-linear composite stress-strain relationship combined with stiffness degradation in sub-critical elements due to both inter-fibre failure and delamination.

An alternative way to reduce the computational complexity is to choose simple critical elements. Akshantala and Talreja [34] developed a critical element model for tension-tension fatigue characterizations of cross-ply laminates. The critical element is chosen as a unit cell where a 90° layer of thickness $2 \times t_1$ is embedded in between two 0° layers of thickness t_2. The dominant failure mechanism is assumed to be the ply delamination between the 90° and 0° layers and modelled by a power-law function. By using these assumptions, Akshantala developed the relationship between the elapsed fatigue life and the resulting ply delamination length. The model showed not

only the fatigue life but also the progressive fatigue failure evolution of a cross-ply laminate.

Spearing [35–38] studied the tension-tension fatigue properties of central notched CFRP composite specimens and found the fatigue failure mechanisms are the 0° ply (in-plane) split initiated from the central notch, ply interface delamination and transverse crack propagation in the 90° plies. By assuming the 0° ply as the critical element and fibre split as the dominant failure mechanism, Spearing developed a power-law for the fatigue growth of splits in order to predict the experimental results. Spearing's model gives good predictions on the ply splitting growth, residual strength and stiffness after a certain number of fatigue cycles. However, his model is limited to centre-notched composite specimens where the critical failure is dominated by the ply splitting growth.

Uleck [39]] developed an analytical model consisting of three sub-models (which are used to describe the damage initiation, damage evolution and composite failure) to predict the axial tension-tension fatigue behavior of 2-layer carbon reinforced unidirectional composites. In Uleck's model, the composite specimen was assumed to be a long fibre bundle and the critical element was selected to be one part of the bundle with an ineffective length δ which is long enough to break the entire bundle. In the first stage, the initial ineffective length was calculated by properties of fibres and matrix, laminate tensile strength, etc. The growth of the ineffective length was regarded as the dominant fatigue failure mechanism and further described using the Paris' Law together with the shear-lag model. The composite specimen was considered to fail when the ineffective length reached a critical value. According to Uleck's model, the fatigue failure probability of the composite specimens can be predicted by using the static tests results.

Because of the symmetric structure, the FRP composite specimens may contain a number of critical elements. On the other hand, the FRP composite specimens are produced from constituent materials (i.e. fibres and matrix) with randomly distributed micro-defects. These imperfections induce scatter in the composite properties (e.g. distributed strengths, scattered fatigue lives, etc.) and random progressive fatigue failures. Therefore, the failure of these critical elements is random, and should be predicted by statistical fatigue models.

Diao et al [7,41] developed a statistics based fatigue model by predicting the fatigue damage progression in the RVEs (see Figure 2.10) containing both critical elements and subcritical elements. In this model, the critical element

was not a typical element but any sub-structure that could cause the final failure of the composite. For instance, in cross-ply composite specimens, all 0° layers have the possibility to be the critical element. The authors assumed the composite fatigue failure started from the damage in the subcritical elements. A damage saturation of the subcritical elements will trigger further damage in the critical element. The composite fatigue properties are represented by fatigue properties of the critical element, of which the initial strengths are statistically distributed. The model is governed by the kinetic strength degradation function, with the consideration of load redistribution from subcritical elements to critical elements. This load redistribution is caused during the damage accumulation process of subcritical elements, and calculated by a semi-empirical load-redistribution factor [7] or shear-lag based load-redistribution factor [41]. It has been noted that the calculated load-redistribution factor is not a constant value but a function of composite fatigue life depending on microscopic failure mechanisms. Diao's model gave good predictions on the strength/stiffness degradation curves, S-N curves and fatigue life scatters of unidirectional and cross-ply composite materials.
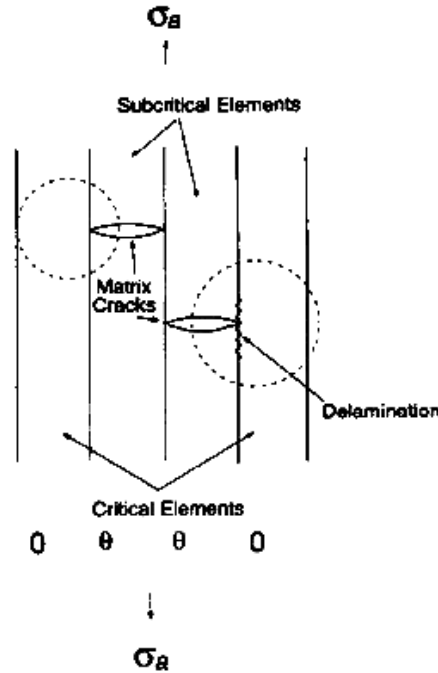
Figure 2.10: The RVE defined in Diao's model (reproduced from [7]

To conclude, the critical element models give fast composite fatigue characterization by quantifying the damage progression in the critical element

in analytical equations. Therefore, they are preferred to use when a quick estimate of the composite fatigue life and strength degradation is needed. However, the calculation of the failure function of the critical element is not completely micro-mechanics based, nor the stiffness degradation calculation in the sub-critical elements. This makes these models rely on the phenomenological curves (or empirical criteria) of macroscopic composites as input to define the fatigue properties of the critical and sub-critical elements. The resulting problem is that the fatigue predictions of composite structures still depends on the fatigue tests of the macroscopic composite specimens. Furthermore, the calculation of the failure function of the critical element should be simple enough for analytical implementation. This may lead to errors when dealing with complicated failures. Therefore, the critical element models can only be used on composites with simple geometries.

2.4.2   Finite element models

Finite element (FE) simulations are developed for fatigue characterization of composite materials, in particular with non-linear material properties and complex coupon geometries. In these continuum mechanics based FE models, the composite fatigue failures are assumed to be a combination of the microscopic failures. The model outputs are the predictions on composite fatigue lives and stiffness degradation curves.

Van Paepegem et al [45] predicted load degradation curves of plain woven GFRP composites under fatigue bending loads. The tests were done in bending displacement control mode. They deduced a power law damage growth model for the prediction of the composite stiffness degradation. The damage growth model parameters were empirical fitting parameters. Their model was implemented by both semi-analytical numerical programming and finite element simulations. The predictions of stress redistribution across the structure under the applied fatigue bending moments and bending load degradation by both implementations were in good agreement. Particularly the predictions of the bending load degradation are close to the experimental observations.

Huang [46, 47] developed a bridging model for fatigue life predictions of the unidirectional FRP composites. In his model, the input parameters are only fibre and matrix fatigue properties and fibre volume fraction. A bridging rule shown in Eq. 2.13 is used to correlate the stress states applied on the fibres

and matrix.

$$\{\mathrm{d}\sigma^m\} = [\mathrm{A}]\{\mathrm{d}\sigma^f\} \tag{2.13}$$

in which $\{\mathrm{d}\sigma^m\}$ and $\{\mathrm{d}\sigma^f\}$ indicate the increments of all six stress components (σ_{11} to σ_{66}) applied on matrix and fibres, and [A] is a 6×6 bridging matrix relating the two stress components. According to the Rule-of-Mixtures theory, the relationship between $\{\mathrm{d}\sigma^m\}$ or $\{\mathrm{d}\sigma^f\}$ and increments of unidirectional composite stress $\{\mathrm{d}\sigma\}$ can be obtained as

$$\{\mathrm{d}\sigma^f\} = (V_f[\mathrm{I}] + V_m[\mathrm{A}])^{-1}\{\mathrm{d}\sigma\} \text{ and } \{\mathrm{d}\sigma^m\} = [\mathrm{A}](V_f[\mathrm{I}] + V_m[\mathrm{A}])^{-1}\{\mathrm{d}\sigma\} \tag{2.14}$$

in which V_f and V_m are the fibre and matrix volume fractions. For 2D planar unidirectional composites, all elements of the matrix [A] were deduced by considering elastic or plastic-elastic properties of fibres and matrix. The bridging parameters in matrix [A] can be retrieved from shear tests of unidirectional composites. Furthermore, the composite constituent failures are determined by the maximum normal stress criterion on fibres and matrix, as shown in Eq. 2.15.

$$\sigma_{eq} \geq \sigma_u \tag{2.15}$$

in which σ_{eq} and σ_u are the equivalent stress and ultimate strength of fibres or matrix. Depending on the third principal stress, σ_{eq} is empirically calculated by Eq. 2.16

$$\sigma_{eq} = \begin{cases} \sigma^1 & \text{when } \sigma^3 < 0 \\ \{(\sigma^1)^q + (\sigma^2)^q\}^{1/q} & \text{when } \sigma^3 = 0 \\ \{(\sigma^1)^q + (\sigma^2)^q + (\sigma^3)^q\}^{1/q} & \text{when } \sigma^3 > 0 \end{cases} \tag{2.16}$$

in which σ^1, σ^2 and σ^3 are three principal stresses, q is the empirical parameter ranging from 1 to infinity. Huang's model provides a comprehensive application incorporating thermal analysis, mechanical analysis, and fatigue analysis of both unidirectional and multi-directional composites.

In continuum based finite element models, composite statistical aspects are represented using statistical properties of the model elements. Lian and Yao [48] developed a statistical continuum based model for fatigue life predictions of FRP composites with different stacking sequences. In their model, the Normal-distributed elastic components were randomly assigned to the model elements. The stiffness degradation of each element was considered in

two alternative ways. If the applied fatigue loads did not reach the criteria for certain microscopic failures (i.e. fibre breakages, matrix failure, fibre/matrix interface failure), the degradations of element stiffness followed traditional phenomenological degradation rules. The corresponding parameters were obtained by the curve fitting of experimental degradation curves of the composite specimens. Otherwise, while a certain microscopic failure occurred, the stiffness degradation was conducted by empirical reduction factors. Their model gave good predictions on cross-ply composites fatigue properties and reasonably good predictions on other multi-directional composites.

Kabir et al [43] developed a two-stage statistics-based micro-mechanical fatigue model to predict the fatigue behaviour of short fibre reinforced ductile matrix composites. The properties of microscopic structures were first simulated using 3D unit cell models taking Weibull-distributed fibre breakages and fibre debonding into account as the failure mechanisms. In order to show the random orientation of short fibres, simulations were performed on several types of unit cells consisting of a fibre volume fraction from 1.8% to 13.1%. Then these unit cell material properties were randomly attributed using Gaussian distribution to the elements of a 3D continuum model as input parameters to characterize the composite stiffness degradation. It was shown that the simulated stiffness degradation curve is in a good agreement with the experimental results on Al-Al$_2$O$_3$ short fibre reinforced composites.

To conclude, the continuum based models implemented by finite element simulations allow virtualization of the numerical representation and are quite versatile since they can characterize the fatigue behaviour of various composite structures. The composite statistical characteristics can also be incorporated in the fatigue predictions. For the numerical continuum models, the fatigue damage evolution in the continuum based models can be described by two approaches. One way, as done in the critical element models, is to use phenomenological curves (or empirical criteria) of the macroscopic composites [48]. And the problem of using the experimental results of the macroscopic composite specimens as input still exists. An alternative way is to predict the damage evolution from a microscopic composite structure by considering the relevant microscopic failures [43]. The latter method is regarded as having more potential because the composite fatigue behaviour is directly predicted from the properties of composite constituents.

2.5   Concluding remarks

1. In micro-mechanical study of unidirectional FRP composites subjected to axial tension-tension fatigue loads, fibre breakage, matrix failure and fibre/matrix interface failure are the three basic failure mechanisms.

2. The broken-to-intact fibre load transfer rule is usually analytically calculated by the shear lag models, in which the calculated SCFs are influenced by fibre properties, matrix properties, fibre/matrix interface properties, fibre alignment, etc.

3. The micro-mechanical models to predict the fatigue behaviour of the composite specimens are categorized into critical element models and finite element models. The critical element models are usually analytical models and therefore give fast composite fatigue predictions, while the finite element models are numerical models which take more time to run. However, the critical element models can only be used for composites with simple geometries, while finite element simulations are more suitable for complicated composite structures.

As mentioned above, the approaches to degrade the elastic properties of composite elements are mostly phenomenological and empirical formulas, based on the composite progressive failure mechanisms. Also, the parameters are extracted from composite specimen tests, rather than the degradation characteristics of local composite structures. In this thesis, the fatigue behaviour of the local composite structures is investigated numerically, as inputs for fatigue predictions of the coupon-size composite structures.

In order to obtain input parameters and to validate modelling results, a number of experiments on single fibres and unidirectional composite dog-bone coupons were performed. These relevant experimental work and results are described in the next chapter.

Chapter 3

Experiments and results

Under the axial tension-tension fatigue loading conditions, fibres are the main constituents that bear the applied loads in the unidirectional composite structures. Therefore, the fibre breakage is considered to be an important fatigue failure mechanism. The fibre properties are used as input variables in the first step of the proposed multi-scale model, i.e. the MF unit cells. Since the fibre elastic properties such as Young's modulus and Poisson's ratio are related to the material elastic constants, they were regarded to be constant and obtained from manufacturers. The reason to utilize the failure strain instead of strength to characterize fibre tensile property is because the axial strains over the cross-section of unidirectional GFRP composites are constant, but stresses are not. Note that the fibres in the MF unit cells are too short to be tested (only 400 μm), their properties are predicted by extrapolating the properties of fibres with a length of several millimetres. For validating the model predictions, tension-tension fatigue tests were performed on unidirectional GFRP composite dog-bone coupons. The composite fatigue lives and axial stiffness degradation curves were extracted from these test results.

The test conditions of the single fibre tests and composite dog-bone tests are first shown in Section 3.1. Then the experimental results of single glass fibre and composite dog-bone tests are discussed in Section 3.2, and summarized in Section 3.3.

35

3.1   Tests description

3.1.1   Fibre tests

The glass fibres have an average diameter of 17.20 μm with a standard deviation of 0.98 μm, and a reference Young's modulus of 73.0 GPa [9,102]. The fibre specimens are prepared according to the standard ASTM 3379-75 [8]. Figure 3.1 illustrates a fibre specimen of 20 mm length used in the fibre tensile test. For fibre tensile tests, fibre specimens of 20, 50, 100 and 200 mm lengths were tested on an MTS 10 kN maximum load capacity testing machine, equipped with a 5 N maximum capacity load cell.

An equation to roughly determine the required number of single fibre tensile tests for each fibre length is given in Eq. 3.1 [103]

$$n_{fib} = \frac{z_{0.45} \times s}{err_{max}} \tag{3.1}$$

in which n_{fib} is the required number of the data sample, $z_{0.45}$ is the critical value corresponding to a 90% confidence interval, s is the standard deviation of the fibre tensile failure strains and err_{max} is the maximum failure strain measurement error. The $z_{0.45}$ value is calculated by the vertical boundary for the area of 90%/2 in the right tail of the probability distribution of the fibre tensile failure strains. For a 2-parameter Weibull distribution (which is going to be used for description of fibre tensile failure strains), it is calculated by Eq. 3.2.

$$z_{0.45} = \exp\{-\frac{1}{\beta_e}\ln(0.025) + \ln(\epsilon_0)\} \tag{3.2}$$

in which β_e and ϵ_0 are Weibull shape and scale parameters of fibre tensile failure strains.

For the glass fibres in this study, an estimate of the Weibull shape parameters is β_e of 5 and ϵ_0 of 3%. If the err_{max} is further assumed as $5\% \times \epsilon_0$, the required numbers of the single fibre tensile tests can then be calculated as 27. Therefore, approx. 30 fibres were tested at a loading rate of 0.5 mm/min at each length. Nevertheless, more tests could to be performed to improve accuracy especially for the extreme value statistics of the fibre strength.

Since it is not possible to apply strain gauges on the fibre specimens, the fibre tensile failure strain is calculated by fibre elongation divided by its
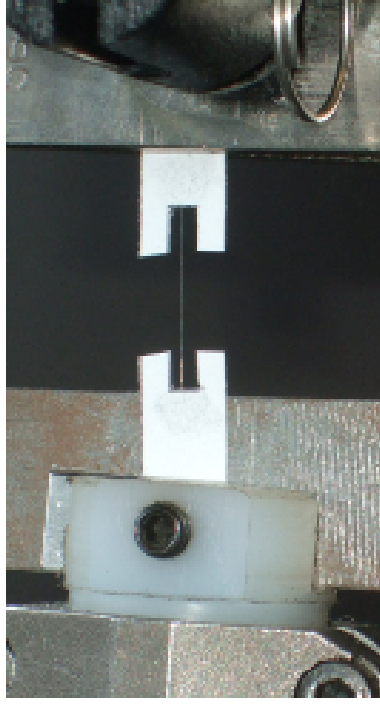
Figure 3.1: A 20 mm length fibre specimen

gauge length. Figure 3.2 illustrates an example of the fibre tensile test data. The calculation of the fibre tensile failure strain ϵ_t is given in Eq. 3.3, where the fibre is assumed to exhibit perfectly linear elastic behaviour according to Figure 3.2.

$$\epsilon_t = \frac{F_t \times (\mathrm{d}s/\mathrm{d}F)}{l} \tag{3.3}$$

in which F_t is the load (force) required to break a fibre in tension, $\mathrm{d}s/\mathrm{d}F$ indicates the inverse of the slope of the load-displacement curve and l is the actual fibre length.

For fibre fatigue tests, 39 fibre specimens of 20 mm length were tested on the same MTS testing machine, at an R ratio of 0.1 and frequency of 20 Hz in load control mode. For each fibre fatigue test, a pre-tension test was applied up to a tensile load of 300 μN to measure the factor $\mathrm{d}s/\mathrm{d}F$ in advance. This pre-tension test is significant because the $\mathrm{d}s/\mathrm{d}F$ value is different for each fibre specimen, depending on the different fibre diameter. Then the maximum fatigue strain ϵ_{max} is calculated by Eq. 3.3 in terms of the maximum fatigue load F_{max}.
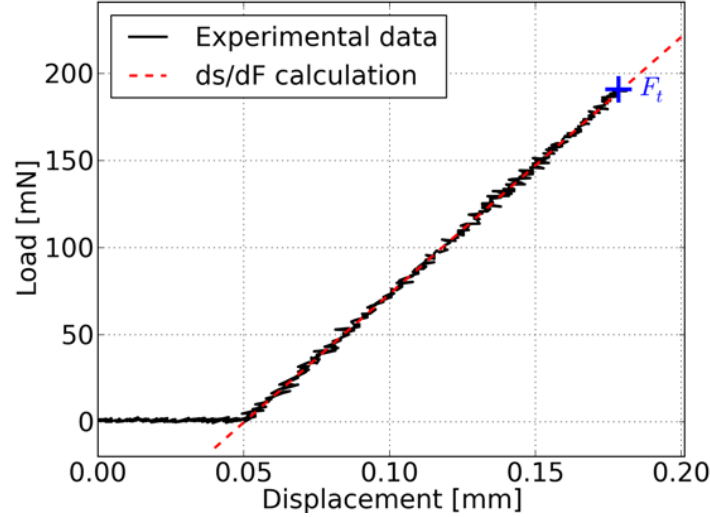
Figure 3.2: Experimental data of a fibre tensile test

Figure 3.3 shows the maximum and minimum displacement signals measured by the internal displacement sensor in the testing machine, subjected to the constant amplitude fatigue loads. It can be seen that the measured maximum and minimum displacements are not significantly changed. Therefore, the fibre fatigue test can be also regarded as occurring in displacement control mode.

3.1.2   Composite coupon tests

A dog-bone geometry (D13) shown in Figure 3.4, was selected for axial tension-tension fatigue tests of unidirectional GFRP composite materials. These composite dog-bone coupons were fabricated from 4-layer laminate panels with the symmetric configuration of $[\pm45°/0°/0°/\pm45°]$ produced by using the Resin Transfer Moulding method. At the gauge area, the $\pm45°$ layers were removed by milling, leaving only the unidirectional layers. Then, 20 mm loading tabs were machined starting at the edge of the 48 mm gauge area to reduce the possibility of delamination between 0° layers and $\pm45°$ layers during the fatigue test. This particular dog-bone geometry was designed for two reasons. First, the delamination failure in between tabs and unidirectional composites was reduced to the minimum, since the tabs are cured together with the unidirectional composites. Second, the dog-bone
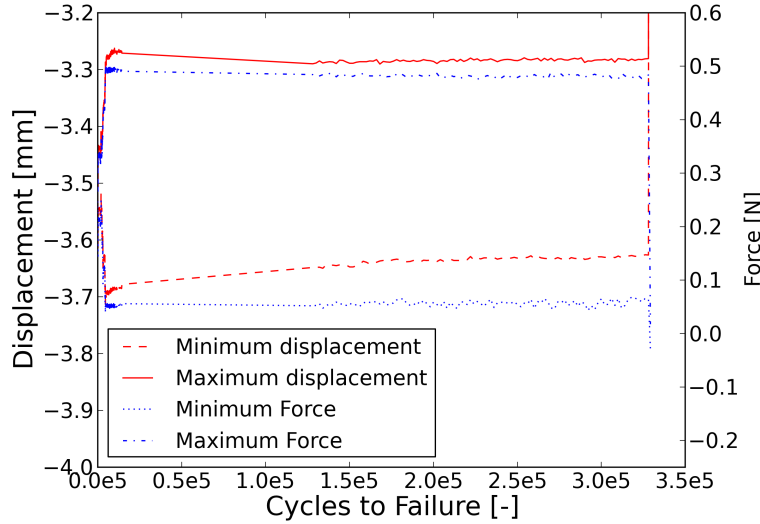
Figure 3.3: Load and displacement signals of a fibre fatigue test

shape was used to create an area of high stress and promote failure in the gauge section. The risk of longitudinal splitting along the fibres was reduced by the gradual curvature.
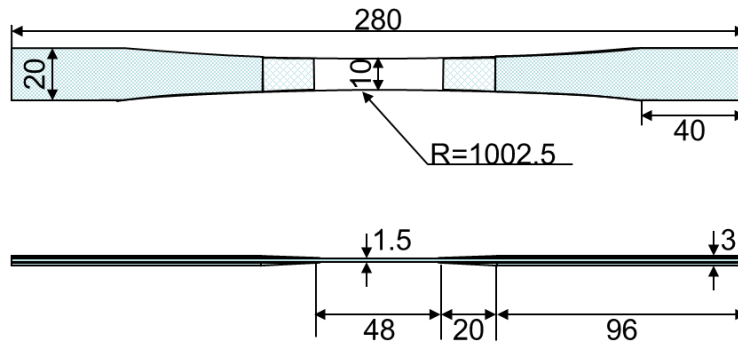
Figure 3.4: Illustration of the unidirectional composite dog-bone coupon

Unfortunately, the composite failure in between tabs cannot be avoided in the fatigue tests of the unidirectional composite dog-bone coupons. This failure usually occurs earlier than the failure in the gauge section and leads to the final failure of the dog-bone coupon, as illustrated by a failed composite dog-bone coupon in Figure 3.5.

Figure 3.5: A failed unidirectional composite dog-bone coupon (TR05D13)

In total 25 dog-bone coupons were tested on an Instron 25 kN maximum load capacity testing machine in load control mode. They were cut from three panels. The fibre volume fractions of the panels were measured as 46.2 % in average. The test frequency was 2 Hz for the low cycle fatigue tests (less than 10^5 cycles), and 8 Hz for the high cycle fatigue tests (above 10^5 cycles). For measuring axial stiffness degradation, 12 of these dog-bone coupons were tested with extensometers, and 6 were tested using a DIC technique. Table 3.1 shows the overview of all tested dog-bone coupons.

Table 3.1: Overview of the tested dog-bone coupons

Coupon ID	From panel	Fibre volume fraction [%]	Maximum Stress [MPa]	Fatigue life [cycles]	Measurement technique
TQ01D13	TQ	45.1	635	6360	extensometers
TQ02D13	TQ	45.1	320	1862053	extensometers
TQ03D13	TQ	45.1	631	4751	-
TQ05D13	TQ	45.1	635	2401	extensometers
TQ06D13	TQ	45.1	622	3055	extensometers
TQ07D13	TQ	45.1	321	2160283	extensometers
TQ08D13	TQ	45.1	315	2098277	extensometers
TQ09D13	TQ	45.1	563	1762	-
TQ02D13	TR	48.8	374	3240015	DIC technique
TR03D13	TR	48.8	601	7479	DIC technique
TR04D13	TR	48.8	370	1147114	DIC technique
TR05D13	TR	48.8	377	1668662	-
TR06D13	TR	48.8	390	772767	DIC technique
TR07D13	TR	48.8	605	9871	DIC technique
TR08D13	TR	48.8	595	15240	-
TQ09D13	TQ	48.8	612	9920	DIC technique
TS01D13	TS	44.8	326	1657831	-
TS02D13	TS	44.8	702	2214	extensometers
TS03D13	TS	44.8	704	2858	extensometers
TS04D13	TS	44.8	347	1488256	extensometers
TS05D13	TS	44.8	707	3512	extensometers
TS06D13	TS	44.8	718	2327	extensometers
TS07D13	TS	44.8	701	2020	extensometers
TS08D13	TS	44.8	349	2243272	-
TS09D13	TS	44.8	349	2623550	-

The composite axial stiffness, considered the same as the composite axial Young's modulus, is calculated by Eq. 3.4.

$$E_{11} = \frac{\Delta\sigma_{11}}{\Delta\epsilon_{11}} \tag{3.4}$$

in which E_{11} is the axial stiffness, $\Delta\sigma_{11}$ and $\Delta\epsilon_{11}$ are the axial stress and strain ranges for calculating E_{11}.

The axial strain in Eq. 3.4 is calculated by the composite dog-bone coupon vertical displacement, which can be measured directly from the internal displacement sensor of the testing machine. However, the corresponding measurements are strongly influenced by the actuator temperature, indirectly related to the fluctuating hydraulic oil temperature. To avoid this temperature influence, the coupon vertical displacements are measured by using external displacement sensors, such as the extensometers. Figure 3.6 shows the extensometers set-up on a tested dog-bone coupon. Two extensometers were attached to an iron frame with fixed distance (25 mm). The iron frame was fixed on the dog-bone coupon by two sets of knife-edge blades, which were placed on rubber pads glued to the coupon's surfaces to minimize the damage.

At the first cycle, the initial strain measurements by extensometers were calibrated using strain gauge measurements. During the fatigue test, each time after a given number of cycles, the degraded axial stiffness was calculated by the ratio of the fatigue stress and strain amplitudes of the next cycle. The strain amplitude was calculated from the average of two amplitudes measured by both extensometers.

The DIC technique provides an indirect solution to measure the displacements by correlating the pictures of the dog-bone coupon without and with load. A surface treatment is required on the gauge area of the dog-bone coupon, provide sufficient contrast for the digital image correlation. This was done by spraying the white paint firstly, followed by sputtering with black paint to create a fine speckle pattern.

In the correlation process, pixels in deformed pictures are matched with those in the reference picture for calculation of the displacement field. The match process is done not on a single pixel but all pixels in a small square window (called subset). Then the displacement of the subset is calculated by minimizing the summation of the squared differences of the grey values of the subset pixels. To obtain the displacement field, the subset scans all over
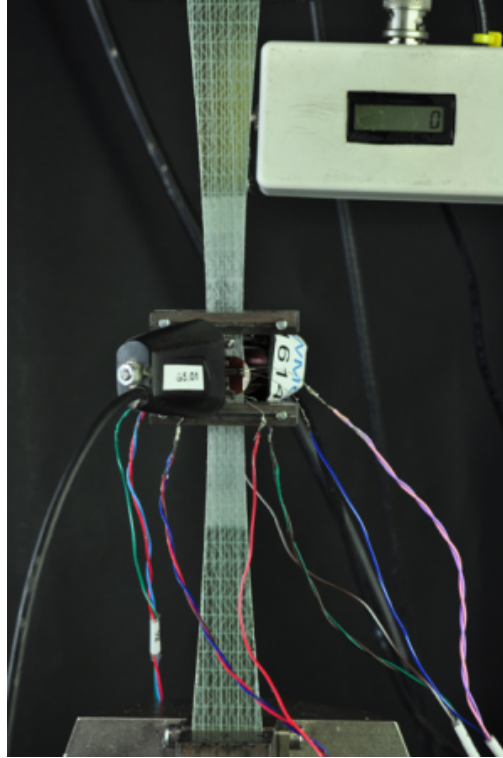
Figure 3.6: The composite dog-bone coupon with extensometers

the coupon surface by steps of a certain number of pixels (called stepsize). The optimal setting for the subset and stepsize depends on several factors such as the size and distribution of black particles, the computational power, the convergence of in-plane strain calculations, etc. Furthermore, for 2D correlation, the length of the stepsize should be smaller than the half-length of the subset for getting better spatial resolution of the displacement field [104].

Before testing, a (reference) picture was taken of the dog-bone coupon without any load, as shown in Figure 3.7. During the test, after each interval (1000 cycles for high cycle fatigue tests and 10 cycles for low cycle fatigue tests), the test was stopped, and two pictures were taken of the tested coupon under 1 kN and 5 kN tensile loads respectively. These two pictures were used together with the reference picture to calculate the coupon axial strains corresponding to the above two tensile load levels. During the entire test, the camera had to be in a fixed position to assure all pictures had the same frame of reference.

The DIC analysis was performed using Matchid2D software developed at
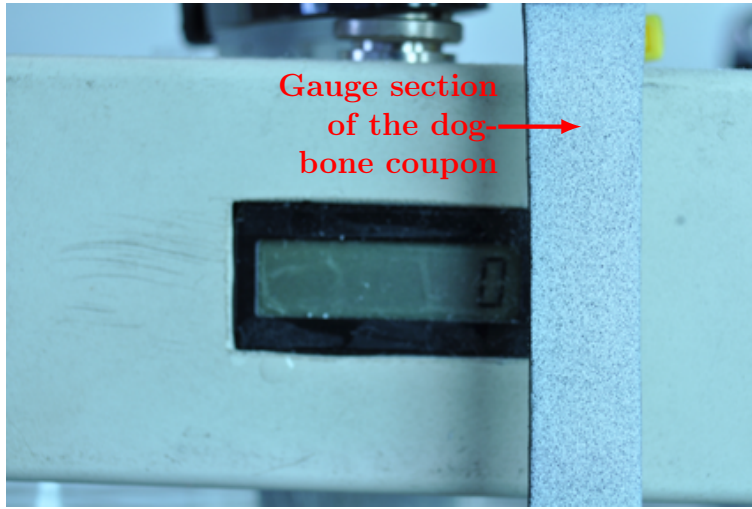
Figure 3.7: The composite dog-bone coupon for DIC technique

the Catholic University College Ghent, Belgium [105, 106]. An area on the coupon surface has to be selected for calculating the in-plane strain field. Subsequently the axial strain of the tested coupon was calculated by averaging the axial strains over this selected area. Finally, the (degraded) axial stiffness of the dog-bone coupon each time after a given number of cycles was calculated from the stress range of 1 kN and 5 kN tensile loads and the corresponding strain ranges.

The selected areas of all six dog-bone coupons are shown in Figure 3.8 [107]. The lengths of the pixel subset and stepsize were set to 20 and 7 respectively. All other parameters in the Matchid2D software were used at the default settings.

3.2 Results and discussion

3.2.1 Fatigue characterization

Fibre breakages occur when the ultimate strain of the fibre is exceeded. As a first-order estimate, the uni-model Weibull distribution is used to predict fibre tensile failure strains. This is convenient to take into account the length
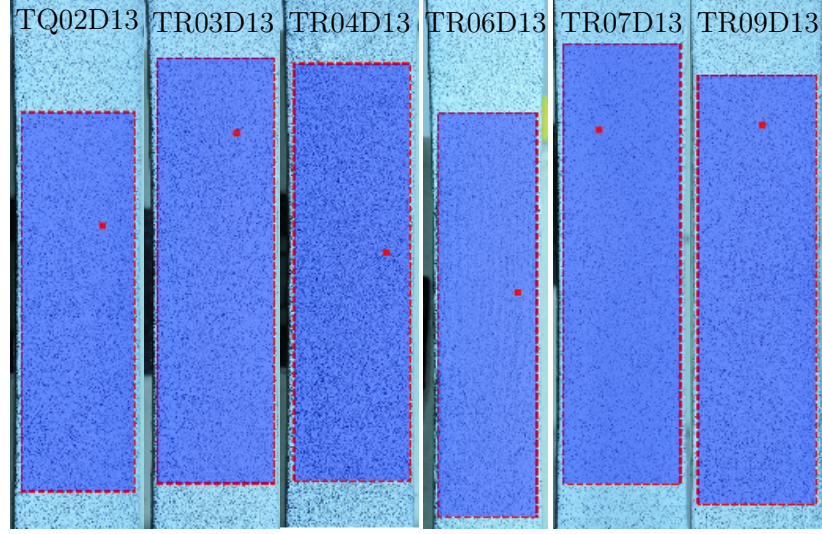
Figure 3.8: Selected areas of the composite dog-bone coupons for DIC analysis

effect in the model. Rewriting Eq. 2.1 for strain leads to Eq. 3.5.

$$P(\epsilon_t) = 1 - \exp\{-\frac{l}{l_{ref}}(\frac{\epsilon_t}{\epsilon_{0ref}})^{\beta_e}\} \tag{3.5}$$

in which P is the fibre failure probability of tensile strain ϵ_t (or less), l_{ref} and l are the reference and actual lengths, β_e and ϵ_{0ref} is the Weibull shape and scale parameters corresponding to the reference length. Then, the relationship between fibre length and the average tensile failure strain can be obtained by Eq. 3.6.

$$\epsilon_{t,avg} = (l/l_{ref})^{(1/\beta_e)}\epsilon_{0ref}\Gamma(1 + 1/\beta_e) \tag{3.6}$$

In order to describe the complete data set of the fibre fatigue lives, the Strength-Life-Equal-Rank-Assumption [108] is applied to correlate the fibre fatigue lives and (quasi-static) tensile failure strains. The fibre is assumed to fail when its ultimate tensile failure strain degrades to the applied maximum fatigue strain ϵ_{max}, through an S-N form fatigue model given by Eq. 3.7.

$$\log(N) = C_1 \times [\log(\epsilon_{max}) - \log(\epsilon_t)] \tag{3.7}$$

in which C_1 is the S-N slope in a log-log plot, N is the fibre fatigue life and ϵ_t is the tensile failure strain of that fibre. Note that the C_1 parameter is negative

because ϵ_{max} is always smaller than ϵ_t. Then the whole family of fibre S-N curves is characterized by a median S-N curve formed by connecting the fatigue life with 50% failure probability at each ϵ_{max} level and a quantification of fatigue life scatter. In order to achieve this, fibre fatigue lives are described by a two-parameter Weibull distribution function Eq. 3.8, which is derived by substituting Eq. 3.7 into Eq. 3.5.

$$P(N) = 1 - \exp\{-(\frac{N}{N_0})^{\beta_N}\} \text{ where } \beta_N = -\frac{\beta_e}{C_1} \text{ and } N_0 = (\frac{\epsilon_0}{\epsilon_{max}})^{-C_1} \qquad (3.8)$$

in which, β_N and N_0 are Weibull shape and scale parameters of fatigue lives subjected to ϵ_{max}. The Weibull shape parameter β_N is used to depict the fatigue life scatter. Generally, the single glass fibres exhibit small β_N values, for instance from 0.1 to 0.5. On the contrary the composite dog-bone coupons exhibit large β_N values, for instance from 1 to 5. In Figure 3.9, the fibre fatigue life probabilities calculated by Eq. 3.8 with β_N of 0.1, 0.5, 1 and 5 are illustrated, with the N_0 set at 10^6 cycles.
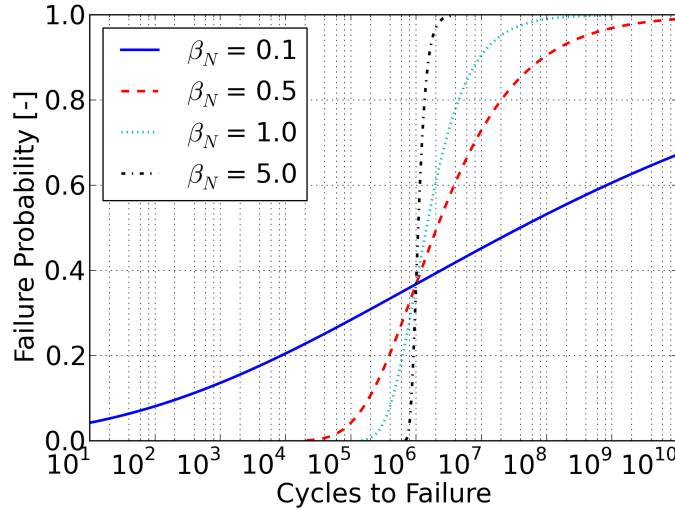
Figure 3.9: Illustration of fibre fatigue life probabilities with different β_N

For each ϵ_{max} level, the fatigue life with 50% failure probability N_{median} can be calculated by Eq. 3.9.

$$N_{median} = N_0[\ln(2)]^{1/\beta_N} \qquad (3.9)$$

Therefore, the median S-N curve is shown by Eq. 3.10.

$$\log(N_{median}) = C_1 \times \log(\epsilon_{max}) + C_2 \text{ where } C_2 = -C_1 \log(\epsilon_0) + \frac{\log[\ln(2)]}{\beta_N}$$

(3.10)

in which C_1 and C_2 are the slope and intercept.

Parameters β_N, C_1 and C_2 in Eq. 3.10 are fatigue parameters deduced for single glass fibres, but can also be used for the MF unit cells and MS models. In the latter two numerical models, ϵ_0 is regarded as the Weibull scale parameter of the equivalent tensile failure strains ϵ_{eq}, which are calculated from the projection of the fatigue lives by the S-N slope onto the y-axis, as shown in Figure 3.10.
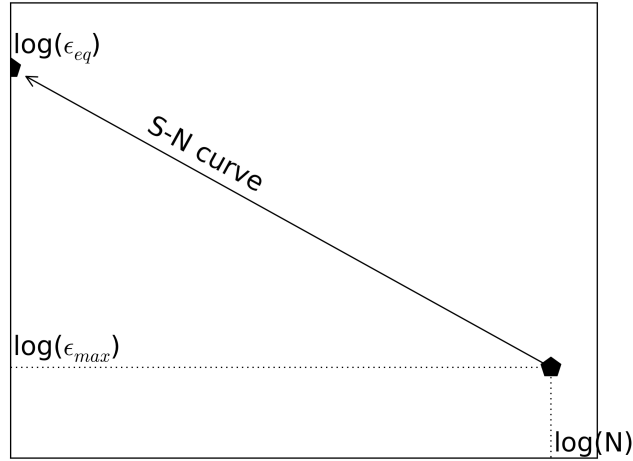
Figure 3.10: Illustration of calculation of an equivalent failure strain

According to Weibull properties, the coefficient of variation is calculated by Eq. 3.11.

$$cov = \sqrt{\frac{\Gamma(1 + 2/\beta_N)}{\Gamma^2(1 + 1/\beta_N)} - 1}$$

(3.11)

in which cov is the coefficient of variation. It can be seen that the calculated cov only depends on the shape parameter β_N, and is therefore constant for

all ϵ_{max} levels. Furthermore, Eq. 3.11 also indicates that the cov of fibre fatigue lives is much larger than fibre tensile failure strains, by reason of the very small shape parameter β_N.

For the description of fatigue lives tested under load control modes, Eq. 3.10 is rewritten to Eq. 3.12 in terms of the stress σ_{max} for the fatigue characterization.

$$\log(N_{median}) = C_1 \times \log(\sigma_{max}) + C_2 \text{ where } C_2 = -C_1 \log(\sigma_0) + \log[\ln(2)]/\beta_N \tag{3.12}$$

in which C_3 is the stress based S-N intercept, σ_0 is the Weibull scale parameter of the equivalent strengths calculated by the projection of the fatigue life by the S-N slope onto the y-axis. Eq. 3.12 characterizes the fatigue lives of ideal composites with no imperfection and the same fibre volume fraction, i.e. the CS models. For practical use of the composite dog-bone coupons, it has to be noted that the extraction of the fatigue parameters β_N, C_1 and C_3 is affected by many factors, such as manufacturing flaws, random fibre clusters and fibre volume fractions.

From Eqs. 3.10 and 3.12, it can also be seen that only two of the fatigue parameters β_N, C_1 and C_2/C_3 are independent.

3.2.2   Fibre properties

Figure 3.11 shows the experimental average tensile failure strains for different lengths. For a reference length of 20 mm, the values of Weibull parameters β_e and ϵ_{0ref} are extracted as 4.9 and 2.8%. Using this choice of reference length, the predictions of average fibre tensile strains with respect to other lengths were calculated by Eq. 3.6. In Figure 3.11, it can be seen that the predictions are in good agreement with the experimental data.

Figure 3.12 shows the experimental data of fatigue tests on single glass fibres with 20 mm length. A fatigue life of 1 cycle was assigned to fibres which broke during the initial cycle, before reaching the ϵ_{max} level. These tests were regarded as 1-cycle fatigue tests and they were plotted on the strain-axis. Data points with arrows were runout tests which were stopped before failure of the fibres. In the first few decades of cycles, the maximum fatigue load is gradually increasing to the predefined level to avoid overshoot at this high frequency. Any error arisen by these first cycles is negligible since the entire fatigue lives of most fibres are higher than 1000 cycles.
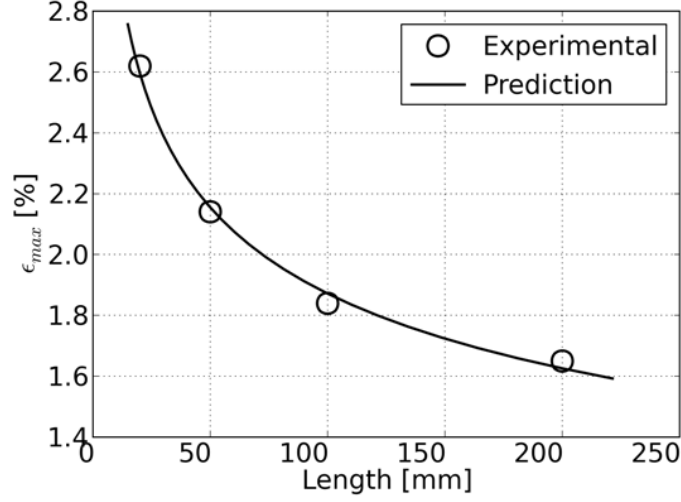
Figure 3.11: Fibre static test results

The fatigue parameters C_1, C_2 and β_N were extracted by using the Maximum Likelihood Estimation (MLE) method, in which the 1-cycle fatigue tests were treated as left-censored data and runout tests as right-censored data. As shown in the legend of Figure 3.12, the extracted values for C_1, C_2 and β_N values are -18.4, 12.1 and 0.144.

In agreement with the results in the literature [67–69], fibre fatigue lives exhibit a large scatter, as indicated by a low value of β_N in Figure 3.12. This large fatigue life scatter results in considerable uncertainty in the extracted C_1 value of the fibres. A sensitivity study of the C_1 value extraction was done by calculating the 95% confidence interval using the Likelihood Ratio Bounds (LRB) method. In the LRB method, a wide range from 0 to -50 of trail C_1 values were numerically scanned using intervals of -0.01. The C_1 values were regarded to be within the 95% confidence interval if they satisfied Eq. 3.13.

$$-2\ln\left[\frac{L(C_1)}{L(\hat{C}_1)}\right] \geq \chi^2_{0.95,1} \tag{3.13}$$

in which $L(C_1)$ is the likelihood value for a trail C_1 value (in the range from 0 to -50), $L(\hat{C}_1)$ is the maximum likelihood value for the maximum likelihood estimate for C_1 (i.e. -19.4), $\chi^2_{0.95,1}$ is the chi-squared statistics with 95% probability and 1 degree of freedom and equals to 3.84. The fibre fatigue
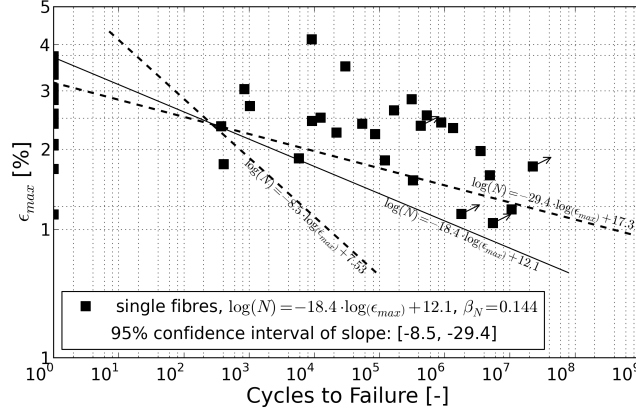
Figure 3.12: Fibre fatigue test results

data suggest that extracted C_1 values within 95% confidence interval are in a range from -8.5 to -29.4, as shown also in the legend of Figure 3.12. To indicate the region covered by the possible S-N curves, the S-N curve with the best C_1 value is plotted as the solid line while the S-N curves with extreme C_1 values are plotted using the dashed lines in Figure 3.12.

There are two aspects contributing to this large interval of extracted fibre C_1 values. Firstly the scatter of the fibre fatigue lives is large. Therefore the calculated likelihood value is not sensitive to the change of trial fibre C_1 values. Secondly fibre fatigue lives are located mostly in limited range of ϵ_{max} between 2.0% and 3.5%. The extraction of fibre C_1 value will be improved by adding some more test results at the ϵ_{max} levels lower than 2.0%. Then, the technical difficulty would be that high frequency testing equipment is required to measure the fatigue lives longer than 10^8 cycles subjected to such low ϵ_{max} levels, with a reasonable time frame.

As discussed in the previous chapter, according to the creep test results, fibres show a range of C_1 values ranging from -20 to -30 for E-glass fibres [68, 69]. For the case of cyclic loading fatigue lives, the C_1 value is expected to be within a similar range. To investigate the influence of the value of C_1, values of -10.0, -20.0 and -30.0 (corresponding approximately to the two extremes in the range and an average value) are used in fatigue simulations of the MF unit cells.

3.2.3   Unidirectional composite dog-bone fatigue properties

The initial longitudinal Young's modulus E_{11} and Poisson's ratio ν_{12} were calculated from the data obtained from 14 unidirectional composite dog-bone coupon tests. Table 3.2 shows the measurements of initial E_{11} and ν_{12}.

Table 3.2: Measurements of initial composite elastic properties

	E_{11} [MPa]	ν_{12} [-]
Average	37600	0.268
Standard deviation	2135	0.017

Figure 3.13 shows the experimental fatigue lives, which are fit by Eq. 3.12. By using the MLE method, the β_N, C_1 and C_3 values of the dog-bone specimens are extracted as 1.75, -9.8 and 31.4. The 95% confidence interval of C_1 values are also extracted using the LRB method. The main S-N curves with the best C_1 and the extreme C_1 values of the 95% confidence interval are plotted by solid and dashed lines in Figure 3.13. Compared to the single fibres, the composite dog-bone coupons show much smaller scatter in fatigue lives and 95% confidence interval of the S-N slope. The reason is probably that the composite dog-bone coupon always fails at the cross-section where a critical number of fibres are broken. For a unidirectional dog-bone coupon, the strength of any composite cross-section at the gauge area is similar and close to the average fibre strength.This also suggests that the fatigue life scatter of the unidirectional dog-bone coupons is small according to a Strength-Life-Equal-Rank-Assumption.

Twelve normalized axial stiffness degradation curves obtained using extensometers are plotted in Figure 3.14(a). A high dispersion is found at the start of the curves (low cycles region). This scatter is attributed to the scatter of axial strain measurements caused by the (random) drift of the extensometers early in the test, but not to the stiffness degradation of the coupon itself. Due to the small stiffness degradation in comparison to the observed scatter, no clear statement on the amount of stiffness degradation can be made. It can only be said that the stiffness degradation seems to be limited to a few percent until just before failure. Furthermore, the stiffness of the coupon TQ02D13 is found to be largely reduced in the second half of the
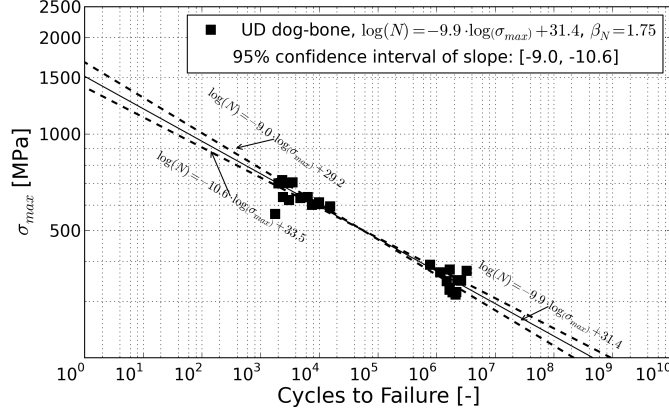
Figure 3.13: Fatigue lives of unidirectional composite dog-bone coupons

fatigue test. This large reduction of the stiffness is due to the drift of the extensometers [107].

The early normalized axial stiffness scatter due to the initial extensometer drift can be removed by normalizing the axial stiffness using the second rather than the first stiffness measurement (asuming that the first and second stiffness measurements are same). Then the normalized axial stiffness degradation curves are re-plotted in Figure 3.14(b). It can be seen that the normalized axial stiffness degradation curves are not significantly different from the maximum fatigue stress σ_{max} levels. This suggests the micro-mechanical fatigue failures (i.e. fibre breakage, fibre debonding, etc.) existing in the dog-bone coupon are probably independent of the σ_{max} levels.

Six normalized axial stiffness degradation curves obtained using the DIC technique are shown in Figure 3.15. Note that the axial stiffness degradation curve of the coupon TR02D13 is regarded as invalid for two reasons. Firstly, the stiffness exhibits an increasing trend during the fatigue test, instead of degradation. Secondly, because of the extreme high stiffness calculated at the end of the fatigue test, the normalized stiffness degradation curve of the coupon TR02D13 is far below the curves measured from the other tests. However, the reason is still not clear.

Except for TR02D13, the normalized axial stiffness degradation curves of the other dog-bone coupons are in good agreement with each other. Again, the σ_{max} level does not considerably affect the composite axial stiffness degradation.

(a) Original

(b) Excluding the initial drift influence
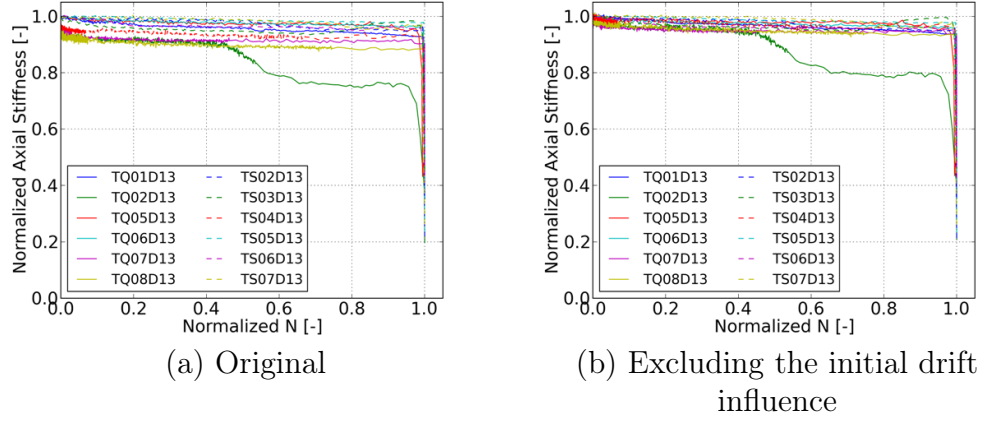
Figure 3.14: Normalized axial stiffness degradation curves measured by extensometers
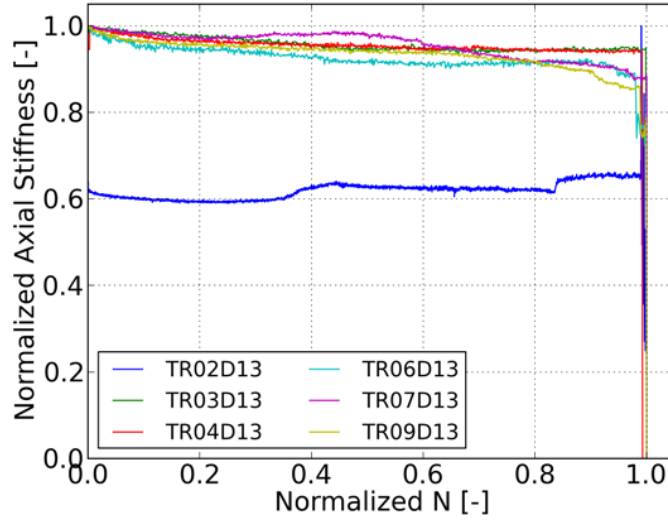
Figure 3.15: Normalized axial stiffness degradation curves measured by DIC technique

3.3   Concluding remarks

1. The fatigue lives can be characterized by three parameters. For single glass fibres, the MF unit cells and MS models, they are shape parameter β_N, S-N slope parameter C_1 and strain-based S-N intercept parameter

C_2 in Eq. 3.10. For unidirectional composite dog-bone coupons and the CS models, they are shape parameter β_N, S-N slope parameter C_1 and stress-based S-N intercept parameter C_3 in Eq. 3.12.

    (a) Fatigue life scatter of single glass fibres is much larger than that of unidirectional composite dog-bone coupons.

    (b) Because of the large fatigue lives scatter, a single C_1 of individual fibres is hard to pinpoint. The best value for fibres is -18.4 obtained using the MLE method. However, the sensitivity study shows the C_1 values of fibres lie in a range from -8.3 to -31.4 corresponding to 95% confidence interval.

    (c) The C_1 value of unidirectional composite dog-bone coupons is calculated as -9.9, with the 95% confidence interval from -9.0 to -10.6.

2. The axial stiffness degradation in unidirectional dog-bone composite coupons is studied using both extensometers and Digital Image Correlation technique.

    (a) The normalized composite axial stiffness degradation curves measured using extensometers exhibit a high dispersion at the beginning. This large scatter is due to the initial drift of extensometers and therefore does not exist in the stiffness degradation curves measured using the DIC technique.

    (b) The maximum fatigue stress σ_{max} level does not significantly influence the composite normalized axial stiffness degradation curves.

The extracted fibre properties will be used together with the matrix properties as the input variables to predict the axial tension-tension fatigue behaviour of unidirectional composites at the micro-, meso- and macroscales. The final fatigue predictions will be verified by the experimental results of the unidirectional composite dog-bone coupons. As the first modelling step, the fatigue simulations of MF unit cells are presented in details in the next chapter.

Chapter 4

Numerical fatigue simulations of the MF unit cells

Numerical studies of the fatigue behaviour of the MF unit cells are carried out in this chapter. The numerical model, fatigue simulation procedure and applied boundary conditions for calculating the MF unit cell elastic properties are first described in Section 4.1. The cumulative damage rule used in the MF unit cell fatigue simulations is particularly discussed in Section 4.2. Then in Section 4.3, the fatigue simulation results are discussed. Finally the concluding remarks are summarized in Section 4.4.

4.1 Multi-Fibre unit cells

The MF unit cell describes the structural details of unidirectional composites at micro-scale. In this study, the determination of the number of fibres in a MF unit cell was done under the following considerations.

1. The unit cell should contain enough fibres to allow load transfer from the broken fibre(s).

2. Fibres are aligned quasi-hexagonally.

3. Fibres should be all complete as opposed to portion of fibres to avoid the situation that several MF unit cells share the same fibre.

4. The unit cell should be computationally efficient.

The MF unit cell to satisfy these above conditions is regarded consisting of 7 to 45 fibres. For a MF unit cell with less than 7 fibres, a hexagonal fibre array cannot be generated. On the contrary, for a MF unit cell with more than 45 fibres, the computational effort becomes prohibitive.

For comparing the fatigue behaviour of MF unit cells of different size, the MF unit cells consisting of 7 and 45 fibres were created making use of a programme "Meso3DFibrer" developed by Mishnaevsky Jr and Brøndsted [53, 54, 109]. These two types of MF unit cells are called 7-fibre unit cell and 45-fibre unit cell respectively. In both MF unit cells, fibres had a constant diameter of 17.2 μm, and were positioned in a rectangular volume. The fibre volume fraction was set as 0.5 [110]. For this high fibre volume fraction, the influence of fibre alignment on the fatigue behaviour is small. Therefore, the fibres in both MF unit cells were aligned in a near hexagonal array with a constant distance between surrounding fibres and the unit cell border. The unit cell length was set as 400 μm. This length is much longer than the ineffective length caused by a fibre breakage, i.e approx. 10 times as long as the fibre diameter for a hexagonal fibre array with 50% fibre volume fraction [111]. This allows a fibre to possibly break at least two positions during the fatigue simulation.

The major role of matrix in the MF unit cell is to redistribute the axial normal loads when new broken fibres are detected. For a composite with a high fibre volume fraction, the fatigue propagation of micro-cracks existing in matrix is constrained by the reinforcing fibres. Based on such consideration, the fatigue failure is not considered in matrix elements. These matrix elements are only failed when the polymer chemical bonds (e.g. Si-O bond) are broken. This matrix failure usually occurs on the matrix elements next to the broken fibre segments by high stress concentrations.

According to the predefined fibre volume fraction and fibre diameter, the dimensions of both MF unit cells are calculated and shown in Table 4.1. All these numerical models are created by 3D 20-node brick elements (element type 21) using the finite element software MSC.MARC [112].

In order to allow for random distribution of fracture locations along the length of fibres, fibres were evenly divided into a number of segments with Weibull-distributed tensile failure strains. The calculation of stress concentration on surviving fibres was done by discretizing the fibres along their length and using finite elements. In order to find an optimal mesh density, fatigue

Table 4.1: Dimensions of the MF unit cells

	7-fibre unit cell	45-fibre unit cell
Length [μm]	400	400
Width [μm]	57	145
Thickness [μm]	57	145
Number of elements	15480	25240

simulations on 7-fibre unit cells with the same initial material properties of fibres and matrix were performed [113]. In these simulations, fibres were divided into 1, 5, 10, 20 and 30 segments along the x axis (along their lengths).

Figure 4.1 shows the normalized longitudinal Young's modulus E_{11} degradation curves from simulations with different numbers of fibre segments (indicated by n_{seg}). The E_{11} moduli were normalized by the initial E_{11} value, and the fatigue lives were normalized by the final unit cell fatigue life. As n_{seg} increases, the normalized E_{11} degradation curves converged to a single curve, for the reason that the accuracy of load transfer calculations is getting better. However, the disadvantage of using a high number of fibre segments is that the computational time is greatly increased. As a compromise, the number of fibre segments n_{seg} was set to 20, allowing for good accuracy and reasonable computational time.
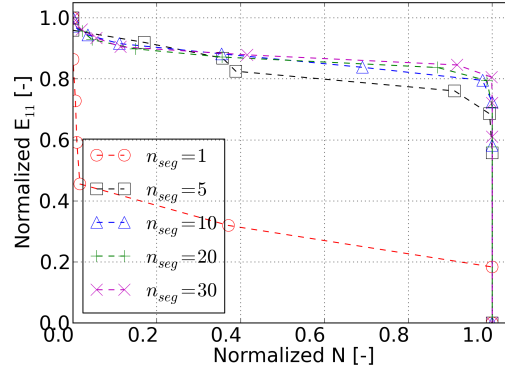
Figure 4.1: Normalized unit cell E_{11} degradation curves for different number of fibre segments

The generated 7-fibre unit cell and 45-fibre unit cell are illustrated in Figure 4.2. The assumptions used in fatigue simulations of these unit cells are:

1. The fatigue failure progression is caused by the accumulation of fibre breakages and resulting matrix (chemical bond) failures. The fatigue failure in matrix elements is not considered.

2. A Weibull distribution is used to define the tensile failure strains of fibre segments, for the determination of the fibre breaking point.

3. During the fatigue simulation, the axial strain of a fibre segment is calculated by averaging the axial strains of all elements in that fibre segment.

4. The final failure of the unit cell occurs when all supporting fibres are broken.

5. The fibre/matrix interface failure is not considered.

6. The plastic deformation of the unit cell is ignored. Therefore, the unit cell can resume its original shape on removal of the applied loads.
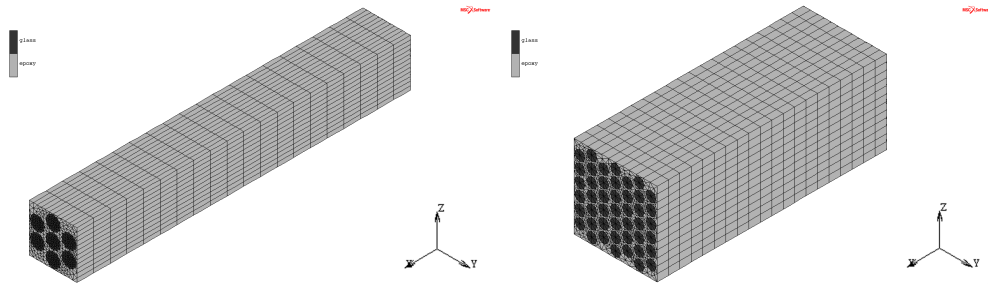
Figure 4.2: The overall view of 7-fibre unit cell (left) and 45-fibre unit cell (right)

As inputs, the matrix failure strain is a theoretical maximum failure strain corresponding to breaking the chemical bonds and is equal to 0.093 [114]. Note that if this critical matrix failure strain is defined significantly smaller than 0.093, a majority of matrix elements will fail after the failure of the weak fibres but prior to the failure of the strong fibres. This large scale failure of most matrix elements will change the load redistribution from the new broken fibre(s) towards a Global Load Sharing rule.

The Young's moduli and Poisson's ratios for fibres and matrix specified by the manufacturers are shown in Table 4.2. The input parameters of Eq. 3.5 to Eq. 3.8 for calculations of initial tensile failure strains and fatigue lives of fibres are shown in Table 4.3. These parameters were selected as tested

from the single fibre static and fatigue tests. Note that the three values for C_1 parameter were used to cover the entire range of possible fibre C_1 values. As shown in Figure 3.12, the scatter in the data corresponds to a relatively wide range of C_1 values and this entire range must be represented in the simulations.

Table 4.2: Static properties of fibres and matrix

	Fibre	Matrix
Young's modulus [MPa]	73000	3640
Poisson's ratio [-]	0.22	0.34

Table 4.3: Parameters of fibre properties characterization

Tensile strain calculation	
l_{ref} [mm]	20
β_e	4.9
ϵ_{0ref} [%]	2.8
Fatigue life calculation	
C_1	-10.0/-20.0/-30.0

As soon as a weak fibre segment breaks, the normal stresses (or strains) of all surviving fibre segments are redistributed according to the shear-lag effect. For both MF unit cells subjected to a tensile strain of 3%, the specific load redistribution caused by the breakage of the lowest segment of the middle fibre was investigated. Figure 4.3 shows the axial (normal) strains of the fibre segments on the same layer with the broken segment. It can be seen that the majority of the normal strain applied on the broken fibre segment is transferred to its immediate neighbours. In particular, the broken fibre and its neighbouring fibres are numbered in Figure 4.3.
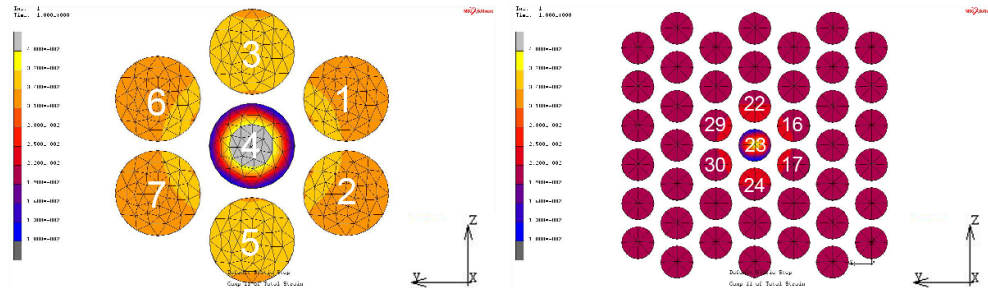

Figure 4.3: Illustration of the broken fibre and neighbouring fibres in both MF unit cells (Left: in 7-fibre unit cell; Right: in 45-fibre unit cell)

The Stress Concentration Factors (SCFs) of the numbered fibres along the fibre axis from the broken point are plotted in Figure 4.4. Note that the SCF curves of the neighbouring fibres on the top and bottom are slightly higher than those curves of the neighbouring fibres on the left and right sides. This is because the neighbouring fibres on the top and bottom are nearer to the broken fibre and therefore bear more transferred loads, compared to the neighbouring fibres on the left and right sides. Figure 4.4 shows that the resulting half-ineffective lengths (measured by the recovery distance of the normal stress on the broken fibre) in the 7-fibre and 45-fibre unit cells are similar. This length is measured about 150 μm, close to the value calculated using the shear-lag model by Landis et al [115].
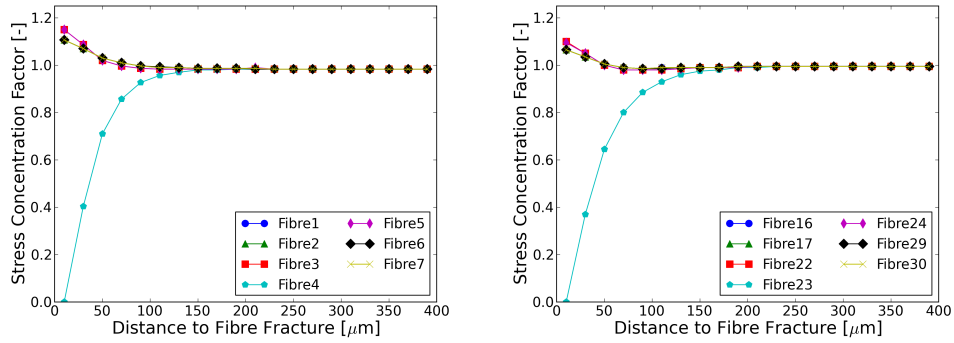
Figure 4.4: SCFs of the numbered fibres in both MF unit cells (Left: in 7-fibre unit cell; Right: in 45-fibre unit cell)

For both MF unit cells, the maximum SCFs of the neighbouring fibres are calculated and shown in Table 4.4. Two maximum SCF values for each MF unit cell are shown corresponding to the two groups of the fibres that are the nearest fibres (e.g. Fibres 3 and 5 in the 7-fibre unit cell) and relatively further fibres (e.g. Fibres 1, 2, 6 and 7 in the 7-fibre unit cell). The maximum SCFs in the 45-fibre unit cell are lower than those in the 7-fibre unit cell because more fibres are involved, and these maximum SCFs are near the middle of the range of the values calculated in the literature [86, 91, 92, 94–98, 101]. An illustration of the comparison between these maximum SCFs is shown in Figure 4.5.

The entire MF unit cell fatigue simulation procedure contains consecutive iterations in each of which new broken fibre segments are found. The simulation is run in displacement control mode. As outputs, the fatigue model gives predictions of the unit cell fatigue life and the degradation curves of all

Table 4.4: Comparison of the maximum SCFs caused by a single broken fibre

	Maximum SCF[1]
Unit cell models	
7-fibre unit cell	1.150/1.107
45-fibre unit cell	1.100/1.065
Shear Lag Models	
Hedgepeth [86]	1.333 (l)
Satry [91]	1.333 (l)
Deng and Fan [92]	1.104 (l)[2]
Hedgepeth and van Deke [98]	1.146 (s), 1.105 (h)
Landis [101]	1.081 (s), 1.085 (h)
Finite Element Models	
Nedele [94]	1.058 (h)
Li [95]	1.126 (l), 1.160 (l)[3]
Xia [96]	1.081 (h)
van der Heuvel [97]	approx. 1.07 (h)

[1] The letter in a parenthesis after the value indicates that SCF is calculated by a linear fibre array (l), a square fibre array (s) or a hexagonal fibre array (h);
[2] SCF calculated in [92] is the average SCF over the ineffective length;
[3] SCFs calculated in [96] are 1.126 for polypropylene matrix composites and 1.160 for epoxy matrix composites.
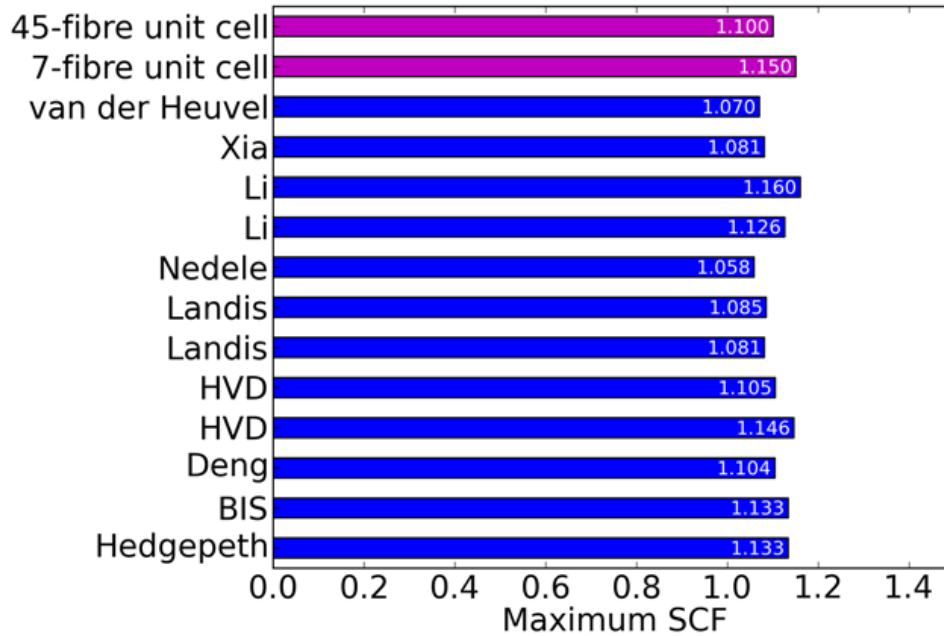
Figure 4.5: Comparison between maximum SCFs in Table 4.4

elastic properties. The calculation consists of the following steps, shown in Figure 4.6.
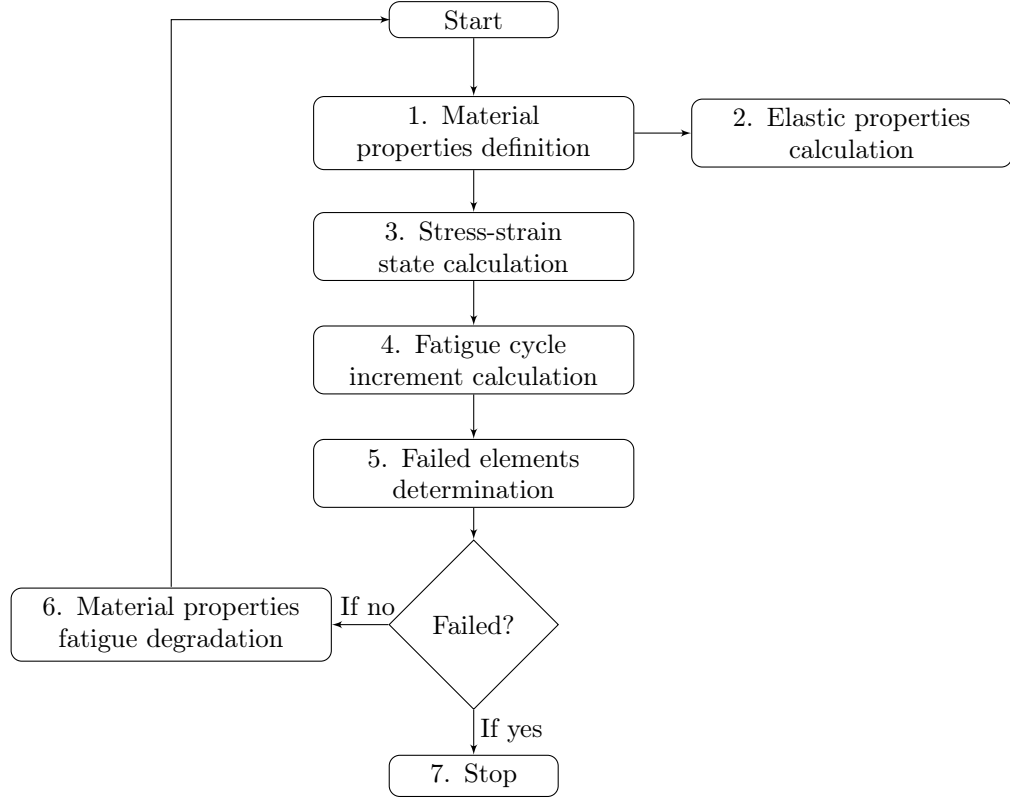
Figure 4.6: The unit cell fatigue simulation flow chart

1. At the beginning of each iteration, material properties of fibre and matrix elements are defined (initial material properties for the first iteration; properties from the previous iteration).

2. For the plots of unit cell properties degradation, longitudinal Young's modulus E_{11}, transverse Young's moduli E_{22}, E_{33}, Poisson's ratios ν_{23}, ν_{32}, ν_{12}, ν_{13}, ν_{21}, ν_{31}, and shear moduli G_{23}, G_{32}, G_{13}, G_{31}, G_{12}, G_{21} are calculated from nine independent finite element simulations. The applied boundary conditions in those simulations are shown below in Table 4.5.

3. The stress-strain state in the unit cell is calculated by using another finite element simulation under applied maximum fatigue strain ϵ_{max}. The applied boundary conditions are similar to those in the simulation for the calculations of E_{11}, ν_{12} and ν_{13}.

4. Fatigue lives of all surviving fibre segments are calculated according to Eq. 3.7. For practical reasons, the calculated fatigue lives of fibre segments less than 1 cycle are set to 0. The cycle increment for the current iteration loop is set equal to the smallest fatigue life calculated across all fibre segments.

5. The failed fibre segments and matrix elements are identified. For fibres, these are the segments with the smallest remaining fatigue life as identified in Step 4. The failure of a fibre element leads to the failure of all elements within that fibre segment. Matrix elements are considered to fail when the tensile strain exceeds 0.093.

6. If, at the end of one iteration, there are still surviving fibres, the degraded mechanical properties of fibre elements are calculated. For the surviving fibre elements, the failure strain degradations are carried out by assuming the slope of the S-N curve has not changed, as illustrated in Figure 4.7, in which the x- and y-axes are both logarithmic. Then the residual tensile failure strains are calculated based on the residual fatigue life by rewriting Eq. 3.7 to obtain Eq. 4.1:

$$\log(\epsilon_{res}) = \log(\epsilon_{max}) - 1/C_1 \log(N_{res}) \tag{4.1}$$

in which N_{res} and ϵ_{res} are the residual fatigue life and tensile strain.
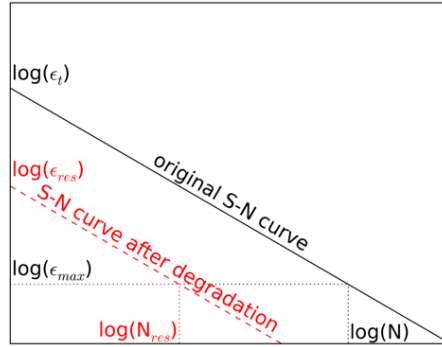
Figure 4.7: Illustration of fibre segment failure strain degradation

As brittle materials, fibres exhibit a strong sudden-death behaviour for the Young's modulus degradation during the fatigue test. Thus, the Young's modulus of fibres is assumed to not degrade in the present

model. Moreover, as mentioned in Step 5, no crack initiation and growth are assumed in the matrix elements. That also means, no material property of matrix elements is degraded. Furthermore, all elastic properties of broken fibre and matrix elements are directly reduced to a near-zero value (e.g. 0.001).

All degraded (and remaining) properties of the fibre and matrix elements are saved for the next iteration.

7. The final failure of the unit cell is reached when all fibres have failed. Figure 4.8 shows a 7-fibre unit cell at failure. The grey colour indicates the high ϵ_{11} strains caused by highly reduced stiffness after the failure of fibre segments. The corresponding modulus degradation curve is plotted at the right-bottom corner, with the black circles showing the stage where the final failure occurs.
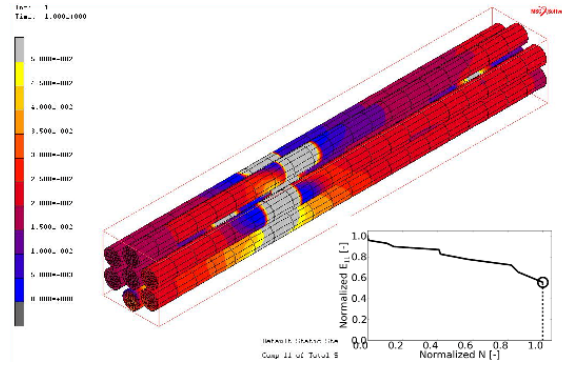
Figure 4.8: Final failure patterns of a 7-fibre unit cell

There are nine simulations in total to calculate the unit cell elastic properties. For showing the periodic boundary conditions, the surfaces of a 7-fibre unit cell are named as Top, $Bottom$, $Front$, $Back$, $Left$ and $Right$, as shown in Figure 4.9, in which top and $bottom$ surfaces are perpendicular to the x-axis (also fibre orientation), $front$ and $back$ surfaces are perpendicular to the y-axis, $left$ and $right$ surfaces are perpendicular to the z-axis. The boundary conditions applied on these simulations are shown in Table 4.5.
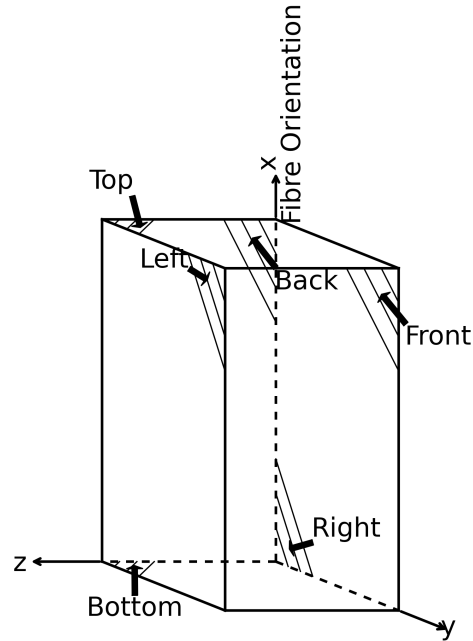
Figure 4.9: Surface terminology of the 7-fibre unit cell

It has to be pointed out that non-flat lateral surfaces still exist in the simulations for shear moduli G_{21}, G_{31}, G_{23} and G_{32}, even though the periodic boundary conditions were applied. For the shear strain calculation, equivalent flat surfaces were created by passing through the corner nodes of these non-flat lateral surfaces.

Table 4.5: Boundary conditions to obtain unit cell elastic properties*

| Calculated elastic properties	Nodal displacements on the unit cell surfaces*					
	Top	Bottom	Front	Back	Left	Right
E_{11}, ν_{12}, ν_{13}	Constant dx on all nodes	Zero dx on all nodes	Zero dy on all nodes	Tie dy on all nodes	Zero dz on all nodes	Tie dz on all nodes
E_{22}, ν_{21}, ν_{23}	Tie dx on all nodes	Zero dx on all nodes	Zero dy on all nodes	Constant dy on all nodes	Zero dz on all nodes	Tie dz on all nodes
E_{33}, ν_{31}, ν_{32}	Tie dx on all nodes	Zero dx on all nodes	Zero dy on all nodes	Tie dy on all nodes	Zero dz on all nodes	Constant dz on all nodes
G_{12}	Constant dy on all nodes; Tie dx and dz of each node to the corresponding node on the bottom surface	Zero dy on all nodes; Zero dx, dy and dz on the middle node	Tie dx, dy and dz of each node to the corresponding node on the back surface		Tie dx, dy and dz of each node to the corresponding node on the right surface	
G_{21}	Tie dx, dy and dz of each node to the corresponding node on the bottom surface		Zero dx on all nodes; Zero dx, dy and dz on the middle node	Constant dx on all nodes; Tie dy and dz of each node to the corresponding node on the front surface	Tie dx, dy and dz of each node to the corresponding node on the right surface	
G_{13}	Constant dz on all nodes; Tie dx and dy of each node to the corresponding node on the bottom surface	Zero dz on all nodes; Zero dx, dy and dz on the middle node	Tie dx, dy and dz of each node to the corresponding node on the back surface		Tie dx, dy and dz of each node to the corresponding node on the right surface	
G_{31}	Tie dx, dy and dz of each node to the corresponding node on the bottom surface		Tie dx, dy and dz of each node to the corresponding node on the back surface		Constant dx on all nodes; Tie dy and dz of each node to the corresponding node on the right surface	Zero dx on all nodes; Zero dx, dy and dz on the middle node
G_{23}	Tie dx, dy and dz of each node to the corresponding node on the bottom surface		Zero dx on all nodes; Zero dx, dy and dz on the middle node	Constant dz on all nodes; Tie dx and dy of each node to the corresponding node on the front surface	Tie dx, dy and dz of each node to the corresponding node on the right surface	
G_{32}	Tie dx, dy and dz of each node to the corresponding node on the bottom surface		Tie dx, dy and dz of each node to the corresponding node on the back surface		Constant dy on all nodes; Tie dx and dz of each node to the corresponding node on the right surface	Zero dy on all nodes; Zero dx, dy and dz on the middle node

* dx, dy and dz are the nodal displacements in the x-, y- and z-directions

4.2   Cumulative damage rule

The fibre fatigue damage under various maximum fatigue loading conditions is described by Eq. 4.1. The calculated residual fatigue life exactly agrees with the calculation using Palmgren-Miner Rule. Assuming that a single fibre is under a variable amplitude fatigue loading sequence consisting of m blocks, the predefined and entire fatigue cycles at the maximum fatigue loading level $\epsilon_{max,i}$ are set as n_i and N_i respectively. Then the damage factor D_i at $\epsilon_{max,i}$ can be calculated by Eq. 4.2.

$$D_i = \frac{n_i}{N_i} = \frac{N_{res,i-1} - N_{res,i}}{N_i} \qquad (4.2)$$

in which $N_{res,i-1}$ and $N_{res,i}$ are the residual fatigue cycles under the maximum fatigue loading level $\epsilon_{max,i}$ for the calculation of n_i. For two extreme conditions, the N_{res} values satisfy the formulas $N_{res,0} = N_1$ and $N_{res,m} = 0$. Figure 4.10 illustrates the relationship between n_i, $N_{res,i-1}$ and $N_{res,i}$.
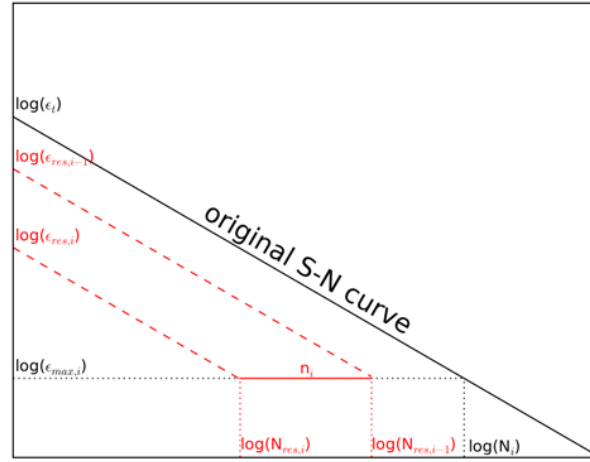

Figure 4.10: Illustration of n_i (a loading block in a variable amplitude fatigue loading sequence)

Substituting Eqs. 3.7 and 4.1 in to Eq. 4.2 gives rise to Eq. 4.4

$$D_i = \frac{\left(\frac{\epsilon_{res,i-1}}{\epsilon_{max,i}}\right)^{-C_1} - \left(\frac{\epsilon_{res,i}}{\epsilon_{max,i}}\right)^{-C_1}}{\left(\frac{\epsilon_t}{\epsilon_{max,i}}\right)^{-C_1}} \qquad (4.3)$$

in which $\epsilon_{res,i-1}$ and $\epsilon_{res,i}$ are the residual strains after $N_{res,i-1}$ and $N_{res,i}$ cycles at fatigue loading level $\epsilon_{max,i}$. Likewise, the extreme values of $\epsilon_{res,i}$ satisfy the formulas $\epsilon_{res,0} = \epsilon_t$ and $\epsilon_{res,m} = 0$. According to Eq. 4.4, the cumulative damage factor up to fibre failure is equivalent to unity, namely

$$\sum_{i=1}^{m} D_i \equiv 1 \tag{4.4}$$

4.3   Results and discussion

The calculated elastic properties of a pristine MF unit cell are shown in Table 4.6. They are compared to the calculations by analytical models, such as Rule-of-Mixtures, the Halpin-Tsai model [116], and Christensen's model [117]. The formulas used for the analytical calculations are given in Eq. 4.5 to Eq. 4.9. The terminology is that E, G, V and ν represent Young's modulus, shear modulus, volume fraction and Poisson's ratio, while the subscripts f and m represent fibres and matrix. The data within parentheses indicate the percentage difference (i.e. the difference between two values divided by the average of these two values) between the elastic properties calculated by MF unit cells and analytical models. All calculated percentage differences are within approx. 10%. As the unit cell size increases from 7 fibres to 45 fibres, the percentage difference becomes smaller for the Poisson's ratios ν_{23}, ν_{32} and the shear moduli G_{31}, G_{12}, G_{13}, G_{21} but larger for the Young's moduli E_{22}, E_{33} and Poisson's ratios ν_{21}, ν_{31}.

1. The longitudinal Young's modulus:

$$E_{11} = E_f V_f + E_m V_m \tag{4.5}$$

2. The transverse Young's moduli [116]:

$$E_{22} = E_{33} = E_m \times \frac{1 + \zeta \eta V_f}{1 - \eta V_f} \text{ where } \eta = \frac{E_f/E_m - 1}{E_f/E_m + \zeta} \text{ and } \zeta = 2 \tag{4.6}$$

3. The Poisson's ratios ν_{12}, ν_{13}, ν_{21} and ν_{31}:

$$\nu_{12} = \nu_{13} = \nu_f V_f + \nu_m V_m, \ \nu_{21} = \nu_{12} \times \frac{E_{22}}{E_{11}} \text{ and } \nu_{31} = \nu_{13} \times \frac{E_{33}}{E_{11}} \tag{4.7}$$

4. The Poisson's ratios ν_{23} and ν_{32} [117]:

$$\nu_{23} = \nu_{12} \times \frac{1 - \nu_{12}E_{22}/E_{11}}{1 - \nu_{12}} \text{ and } \nu_{32} = \nu_{23} \times \frac{E_{33}}{E_{22}} \qquad (4.8)$$

5. The shear moduli:

$$G = G_m \times \frac{1+\zeta\eta V_f}{1-\eta V_f} \text{ where } \eta = \frac{G_f/G_m-1}{G_f/G_m+\zeta} \text{ and}$$

$$\zeta = \begin{cases} 1 & \text{For shear moduli } G_{12},\, G_{13},\, G_{21} \text{ and } G_{31} \\ \frac{1+\nu_{23}}{3-\nu_{23}-4\nu_{21}\nu_{12}} = 0.53 & \text{For shear moduli } G_{23} \text{ and } G_{32} \end{cases}$$

$$(4.9)$$

In addition, the experimental modulus E_{11} and Poisson's ratio ν_{12} calculated from the acquisition data at the first cycle of composite dog-bone coupons are shown in Table 4.6. A good agreement can also be seen on the E_{11} and ν_{12} values between the MF unit cells and experimental results. Therefore, the (degraded) stiffness values calculated using MF unit cells are sufficiently accurate for our purposes.

Table 4.6: Comparison of calculated composite elastic properties

	7-fibre unit cell	45-fibre unit cell	Analytical models	Experimental results
E_{11} [MPa]	38340 (0.1%)	38273 (-0.1%)	38320	37600
E_{22} [MPa]	11969 (0.2%)	10654 (-11.4%)	11945	-
E_{33} [MPa]	11762 (-1.5%)	11139 (-7.0%)	11945	-
ν_{21} [-]	0.084 (-3.5%)	0.076 (-13.5%)	0.087	-
ν_{12} [-]	0.268 (-4.4%)	0.274 (-2.2%)	0.280	0.268
ν_{31} [-]	0.083 (-4.7%)	0.078 (-10.9%)	0.087	-
ν_{13} [-]	0.269 (-4.0%)	0.269 (-4.0%)	0.280	-
ν_{23} [-]	0.326 (-8.5%)	0.342 (-3.7%)	0.355	-
ν_{32} [-]	0.321 (-10.1%)	0.357 (0.6%)	0.355	-
G_{23} [MPa]	3219 (1.4%)	3214 (1.3%)	3174	-
G_{31} [MPa]	4017 (9.8%)	3875 (6.3%)	3640	-
G_{12} [MPa]	4109 (12.1%)	3653 (0.4%)	3640	-
G_{32} [MPa]	3215 (1.3%)	3214 (1.3%)	3174	-
G_{13} [MPa]	4017 (9.8%)	3875 (6.3%)	3640	-
G_{21} [MPa]	4110 (12.1%)	3661 (0.6%)	3640	-

Three batches of the 7-fibre unit cells were modelled with input S-N slope parameters C_1 of fibres of -10.0, -20.0 and -30.0. Furthermore, fatigue behaviour of the 45-fibre unit cells was also modelled in order to compare with the 7-fibre unit cells. Due to computational limitations, only one batch of

the 45-fibre unit cells were modelled with input fibre C_1 value of -30.0. In each batch, 20 unit cells were modelled under three ϵ_{max} levels. These ϵ_{max} levels were selected as 2%, 3% and 4% for the input fibre C_1 values of -10.0 and -20.0, while 3%, 4% and 5% for the input fibre C_1 values of fibres of -30.0. The reason of changing ϵ_{max} values is to avoid having to calculate very long fatigue lives under the ϵ_{max} of 2% for the input fibre C_1 value of -30.0.

As discussed in Section 3.2.1, the fatigue behaviour of the MF unit cells is described by Weibull shape parameter β_N, S-N slope parameter C_1 and strain-based S-N intercept parameter C_2. Table 4.7 shows the extracted fatigue parameters of the MF unit cells, compared with the reinforcing glass fibres (with 400 μm length). The comparison of fatigue parameters between fibres and the MF unit cells gives:

1. The MF unit cell has less fatigue life scatter (i.e. higher β_N values) than the fibres. This tendency of the scatter reduction is pronounced when the unit cell size is increased from 7 fibres to 45 fibres.

2. The C_1 values of the MF unit cells and fibres do not differ significantly. This can be further proved by a sensitivity study of the C_1 values, in which the fatigue parameters except for the C_1 values of fibres were set to be the same. Then the fatigue parameters of the MF unit cells consisting of the above fibres were extracted, as shown in Table 4.8. It can be seen that the extracted C_1 values of the MF unit cell are still quite similar with those of the fibres.

3. The C_2 values of the MF unit cells are higher than those of the fibres because strong fibres in the MF unit cell improve the unit cell fatigue lives. For this reason, the C_2 value of the 45-fibre unit cells is further higher than that of the 7-fibre unit cells, as shown in Table 4.7.

4. In Table 4.8, the C_2 values of the MF unit cells are not always higher than the fibres because the relevant fibres are virtual fibres and much different with the fibres used in this study. Actually, these fibres exhibit less scattered low tensile failure strains indicated by higher β_e values and lower ϵ_0 values (with respect to 400 μm length), according to Eqs. 3.10 and 3.12. As a result, the final failure of the 7-fibre unit cell is more likely to occur right after the breakages of first few fibres due to the efficient load redistribution. This results in the reduction of the C_2 value of the MF unit cells when only the input fibre C_1 value is decreasing.

Table 4.7: Comparison of fatigue parameters between single fibres and MF unit cells

Input fibre C_1		-10.0	-20.0	-30.0	-30.0
single fibre 400 μm long	β_N	0.49	0.25	0.16	0.16
	C_1	-10.0	-20.0	-30.0	-30.0
	C_2	7.6	15.2	22.8	22.8
		7-fibre unit cell			45-fibre unit cell
MF unit cell	β_N	1.03	0.58	0.49	0.58
	C_1	-10.5	-21.0	-32.2	-32.7
	C_2	8.8	16.9	25.4	26.6

Table 4.8: Sensitivity study of the C_1 values of MF unit cells

single fibre 400 μm long	β_N	0.49	0.49	0.49
	C_1	-10.0	-20.0	-30.0
	C_2	7.6	7.6	7.6
7-fibre unit cell	β_N	1.03	1.07	0.76
	C_1	-10.5	-20.0	-29.9
	C_2	8.8	7.9	7.1

Figure 4.11 shows all degradation curves of the elastic constants of a MF unit cell with the input fibre C_1 value of -10.0. For comparison purposes, the elastic properties were normalized by the initial values and the elapsed fatigue cycles were normalized by the final fatigue life. From Figure 4.11, it is found that the rotational symmetry around the fibre axis is not significantly reduced during the fatigue life, by a good match between the moduli and Poisson's ratios along the transverse and through-thickness directions, such as E_{22} and E_{33}, ν_{12} and ν_{13}, etc.

Figure 4.12 illustrates the fibre breakage progression in a 7-fibre unit cell. The broken fibre segments are indicated by large axial strains shown in grey colour. At the right-bottom corner of each graph, the normalized E_{11} degradation due to the corresponding state of fatigue failure evolution is also plotted, the black circle indicates the instantaneous stiffness. The unit cell eventually fails by a cluster of fibre breakages, which is caused by the large stress concentration associated with the shear lag.

Figure 4.14 shows the degradation curves of normalized E_{11} of a 7-fibre unit cell and a 45-fibre unit cell with the input C_1 value of fibres of -30.0, for three different ϵ_{max} levels. Initial reduction of the normalized E_{11} is found independent of the ϵ_{max} levels. This reduction is caused by the sequential breakages of the very weak fibre segments. After that, the matrix elements fail due to the resulting stress concentration. For the case of higher ϵ_{max}
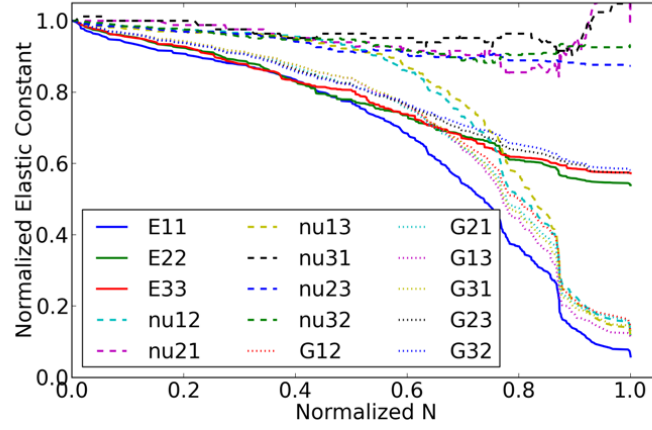
Figure 4.11: Simulated degradation curves of elastic constants of a MF unit cell
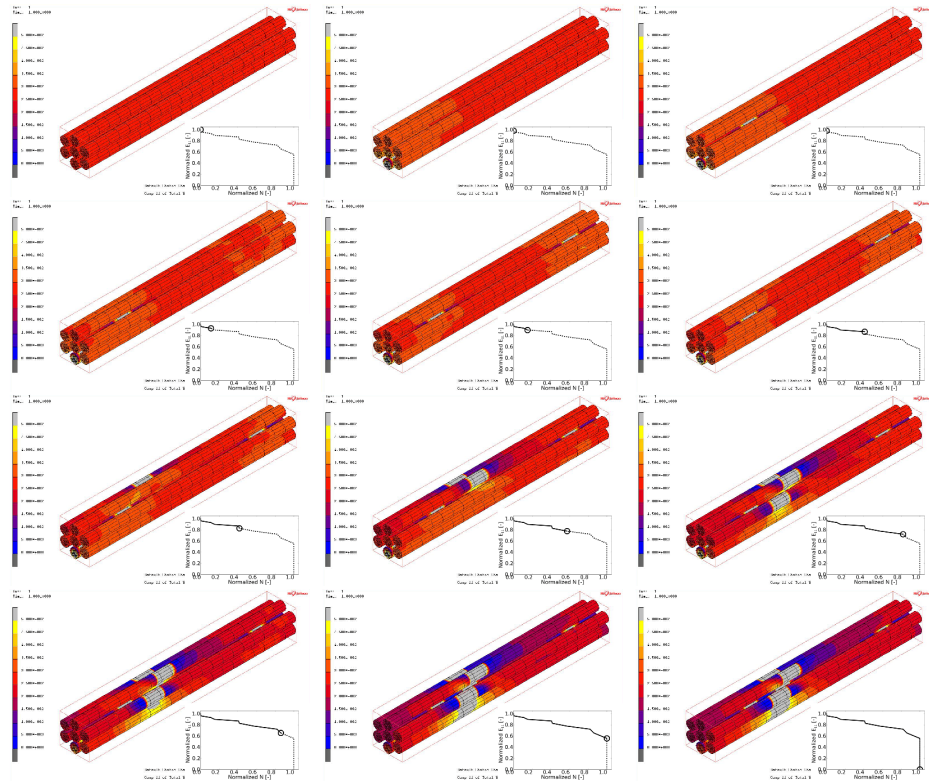

Figure 4.12: Fatigue failure evolution in a random 7-fibre unit cell

levels, the number of failed matrix elements increases. The failure of more

matrix elements alters the subsequent fibre segment breaking sequence by
changing the stress concentrations. These variations in fibre breaking se-
quence, however, do not lead to a systematic change in stiffness degradation.
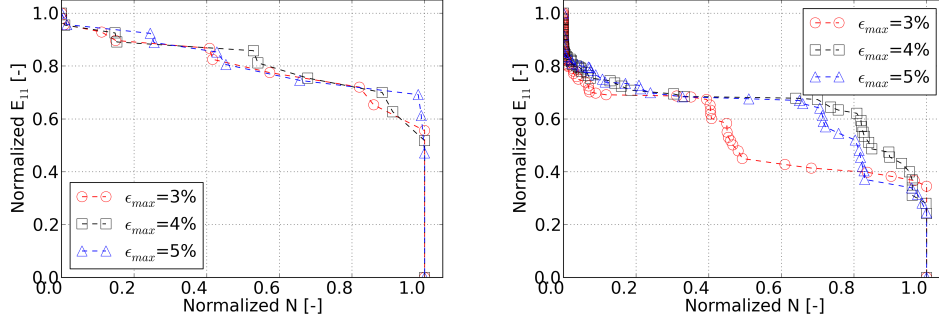
Figure 4.13: Normalized longitudinal Young's modulus degradation curves of
the MF unit cells (Left: a random 7-fibre unit cell; Right: a random 45-fibre
unit cell)

Because of the random damage progression of fibre segments, the stiffness
degradation curves show considerable differences among each unit cell. Fig-
ure 4.14 shows the normalized E_{11} degradation curves of the MF unit cells
(under the lowest ϵ_{max} level). Figure 4.14 shows the normalized E_{11} degrada-
tion curves of the MF unit cells (under the lowest ϵ_{max} level), it can be seen
that the normalized E_{11} degradation curves of the MF unit cells have large
scatter. This implies the fatigue damage progression and property degrada-
tion in the MF unit cell is more random. For the 7-fibre unit cell, the increase
of the fibre C_1 value (from -30.0 to -10.0) will slightly ease the reduction of
the normalized E_{11}, but not affect the scatter of the degradation curves, ac-
cording to the comparison from graphs (a) to (c).

4.4   Concluding remarks

1. The geometries, initial elastic properties and fatigue simulation proce-
   dure of the MF unit cell were introduced.
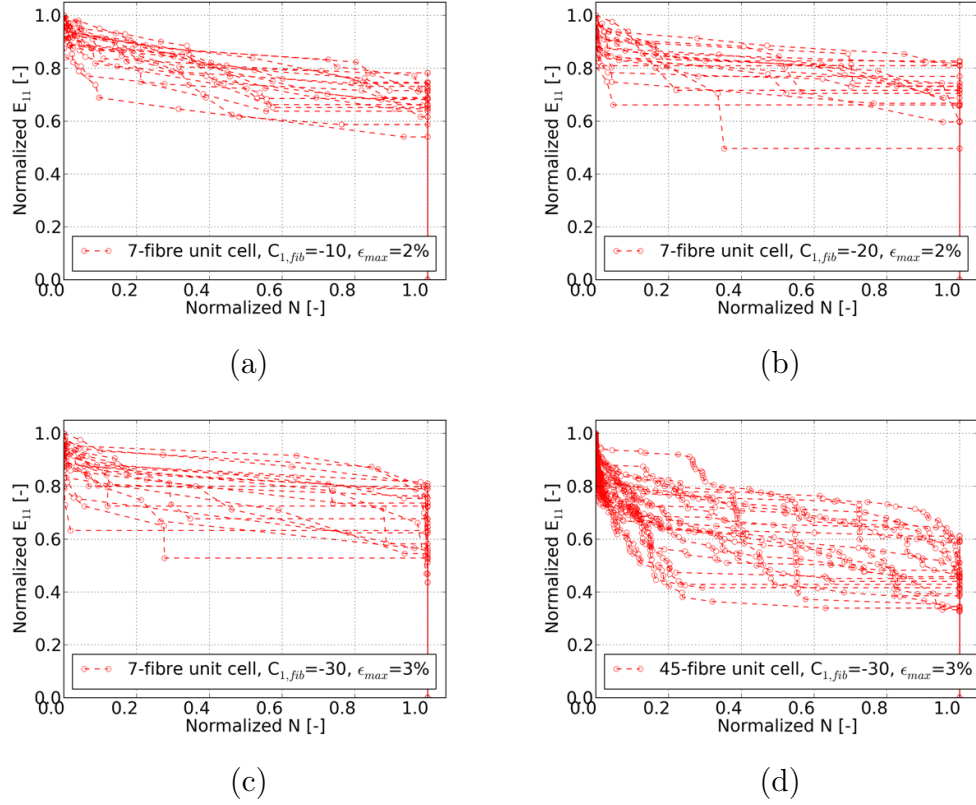
Figure 4.14: Normalized longitudinal Young's modulus degradation curves of the MF unit cells

2. Simulated elastic properties of the MF unit cells are in good agreement with the calculations by analytical models, such as Rule-of-Mixtures, the Halphin-Tsai model, the Christensen's model and limited experimental results.

3. Compared to single glass fibres, the fatigue lives scatter of the MF unit cells is drastically reduced, and the S-N slope parameter C_1 and intercept parameter C_2 are slightly smaller.

4. The normalized E_{11} degradation curves of a MF unit cell under variable fatigue loading conditions are similar, except for some stochastic variation.

5. The normalized E_{11} degradation curves of different MF unit cells are scattered, due to the random breaking sequence of the fibre segments.

6. The increase of the fibre C_1 value (from -30.0 to -10.0) will slightly reduce the degradation rate of the normalized E_{11} of the MF unit cell, but not affect the scatter of the degradation curves.

The simulated fatigue properties of the MF unit cell provide the inputs for fatigue simulations of the MS models. Note that the fatigue lives of the MF unit cells exhibit a wide scatter, according to the large β_N values in Table 4.7. The fatigue failure in the MS model initiates from few very weak MF unit cells. The failure of these unit cells together with the element stiffness degradation leads to stress concentrations on the neighbouring elements to speed up the failure of these elements. In the end, the MS model fails as soon as a critical cluster of failed elements have formed. The details of relevant work are discussed in the next chapter.

Chapter 5

Numerical fatigue simulations of the MS models

In this chapter, fatigue properties of the MF unit cells are scaled up to the MS level. The numerical model and simulation procedure of the MS models are described in Section 5.1. Subsequently, Section 5.2 shows the discussion on the simulation results. The concluding remarks are finally summarized in Section 5.3.

5.1 Meso-Structure models

The MS7 and MS45 models (consisting of 7-fibre or 45-fibre unit cells respectively) were created by stacking structural elements equivalent to the MF unit cells. Therefore the fibre volume fraction of the MS models is the same as the MF unit cells (i.e. 0.5). Figure 5.1 illustrates both MS models, with the dimensions given in Table 5.1. Each element represents a typical 7-fiber or 45-fibre unit cell.

Table 5.1: MS model dimensions

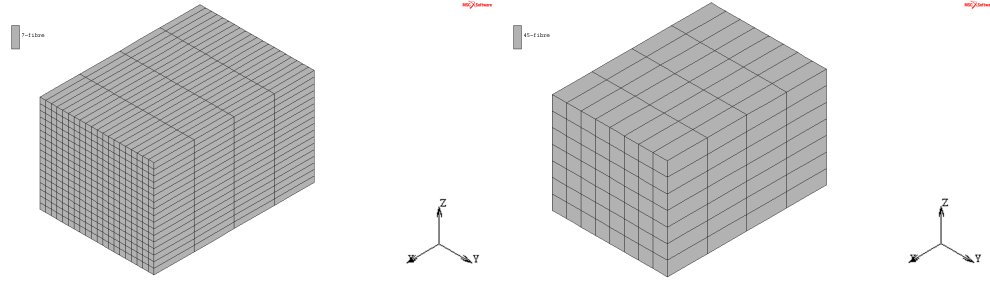|	MS7 model	MS45 model
Length [μm]	1600	1600
Width [μm]	1141	1157
Thickness [μm]	971	1012
Number of elements	1360	224

Figure 5.1: The overall view of MS7 models (left) and MS45 models (right)

The input variables for the structural elements are initial elastic static properties, fatigue lives and degradation curves of the elastic properties. The initial static properties are calculated directly from static simulations of the pristine MF unit cells. The definition of elastic properties degradation is done by randomly selecting a set of elastic properties degradation curves (of a MF unit cell) from a predefined library, which contains the degradation curves calculated from 20 MF unit cell fatigue simulations. The fatigue lives are calculated by using Eq. 3.7 with the fatigue parameters β_N, C_1 and C_2 shown in Table 4.7.

Moreover, because the elastic properties of the unit cell along the y-and z-axes are slightly different (transverse isotropy in 2-3 plane is not maintained, e.g. $E_{22} \neq E_{33}$), an arbitrary number of elements (MF unit cells) were rotated by 90°. For the rotated elements, the elastic properties along the y- and z-axes are interchanged. An example of the element rotation is illustrated in Figure 5.2.
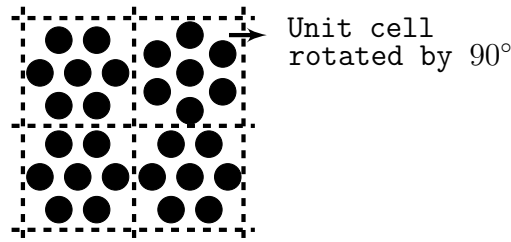

Figure 5.2: Illustration of a random 7-fibre unit cell rotated by 90°

During the fatigue simulation, the damage interaction between the structural elements is ignored. Therefore, the load redistribution due to the damage progression of each element only proceeds via the element global stiffness degradation. In other words, local damage in an element does not directly

create a large stress concentration on neighbouring elements but only causes a stiffness degradation that generally will create a much smaller stress concentration.

The flow chart for the fatigue simulation procedure of the MS model is similar to the that for the MF unit cell which was shown in Figure 4.6. However, the details of the simulation steps are different. The simulation is run in displacement control mode. As outputs, the fatigue model gives predictions of the MS model fatigue life and the degradation curves of all elastic properties. The calculation consists of the following steps.

1. At the beginning of the first iteration, the initial elastic properties of the model elements are defined by the predicted properties of the equivalent numerical models, i.e. the MF unit cells. During each new iteration, these elastic properties are re-defined by the (degraded) properties calculated from the previous iteration.

2. For the plots of the MS model elastic properties degradation, values for the longitudinal Young's modulus E_{11}, transverse Young's moduli E_{22}, E_{33}, Poisson's ratios ν_{23}, ν_{32}, ν_{12}, ν_{13}, ν_{21}, ν_{31}, and shear moduli G_{23}, G_{32}, G_{13}, G_{31}, G_{12}, G_{21} are calculated from nine independent finite element simulations. The applied boundary conditions are the same with those for calculations of the elastic properties of the MF unit cells, described in Section 4.1.

3. The stress-strain state in the MS model is calculated by using another finite element simulation under applied ϵ_{max}. The applied boundary conditions are similar to those in the simulation for the calculations of E_{11}, ν_{12} and ν_{13} (see Section 4.1)

4. The calculation of fatigue cycle increment at the current iteration is different in the MS7 and MS45 models. For the MS7 model, the cycle increment is set equal to the smallest remaining life of the model elements, which are calculated by Eq. 3.7.

   However, for the coarse-mesh model such as the MS45 model, the cycle increment of fatigue cycles is calculated as a fraction of the remaining fatigue cycles of the next possible broken element. This approach is required because otherwise the large element size affects the accuracy of the stress redistribution and stiffness degradation calculations, and consequently of the fatigue life. For the MS7 model this approach is not required because the finer mesh makes them less sensitive to stiffness degradation of individual elements.

As shown in Figure 5.3, it can be seen that a converged normalized E_{11} degradation curve can be obtained when the fraction is selected smaller than 1/20. Therefore, for MS45 models, the cycle increment is set equal to 1/20 of the smallest remaining life of the model elements. In the following iterations, if no elements are found broken, the cycle increment remains the same (as used in previous iteration). Otherwise, the cycle increment is updated by the remaining fatigue cycles of the new broken elements. Then in the next iteration, the increment of fatigue cycles is re-calculated as 1/20 of the calculated smallest remaining life of the model elements.
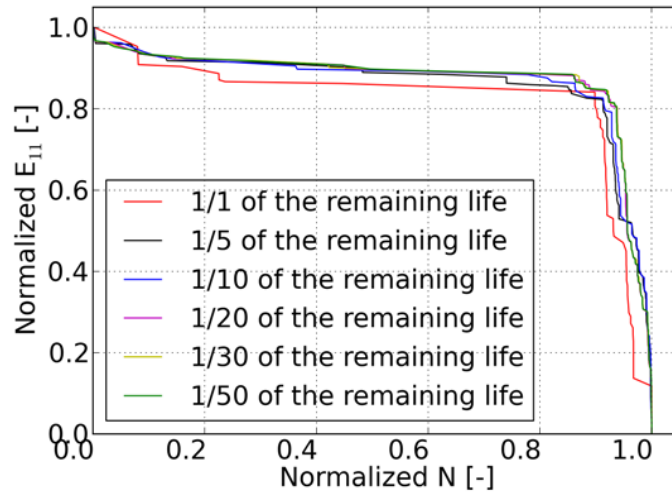
Figure 5.3: Normalized MS45 model E11 degradation curves for different intermediate cycle interpolations

For practical reasons, the calculated cycle increment less than 1 cycle is set to 0.

5. At the current iteration, elements in the MS model withstand variable fatigue loading conditions, calculated by the load redistribution as a result of the elastic property degradation of these elements themselves. The cumulative damage of an element is described by a damage factor, which is calculated by the ratio between the cycle increment and entire fatigue life of that element. For each element, the damage factor at the current iteration is calculated by the ratio between the cycle increment and entire fatigue life of the element. According to Palmgren-Miner

Rule, the final element failure is determined when the cumulative damage factor attains unity.

6. If, at the end of that iteration, the final model failure criterion is not reached, the degraded material properties of the elements are saved for the next iteration. All elastic properties of the broken elements are directly reduced to a near-zero value (e.g. 0.001). All elastic properties of the unbroken elements are reduced by the linear interpolation values of the corresponding normalized elastic property degradation curves. These degradation curves were obtained from fatigue simulations of the MF unit cells, mainly based on the sequential fibre breakages. The matrix failure does not significantly affect the degradation curves since only few matrix elements next to the fibre breaking points failed due to the stress concentration caused by the fibre breakages. As an example, Figure 5.4 illustrates the interpolated degraded E_{11} at 20% of the entire fatigue life (corresponding to a cumulative damage factor of 0.2).
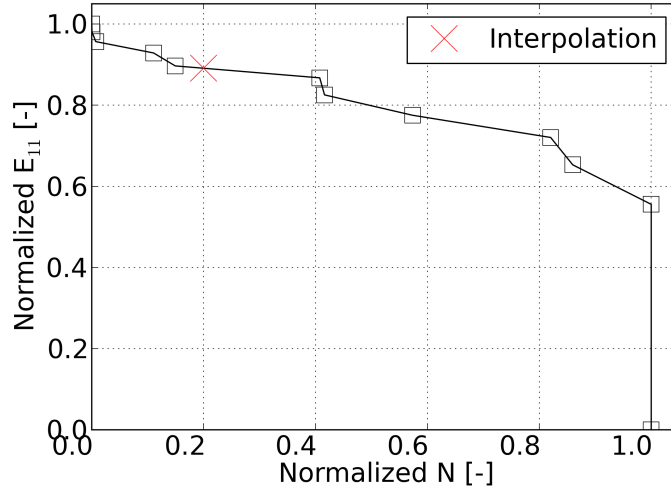
Figure 5.4: Illustration of interpolation of stiffness degradation

7. The final failure of the simulated model is reached when failure of adjacent elements extents to the edge of the model. Figure 5.5 shows the MS7 model at final failure with input fibre C_1 value of -30.0. The corresponding normalized E_{11} degradation curve is plotted at the right-bottom corner, with the black circles showing the stage where the final failure occurs.
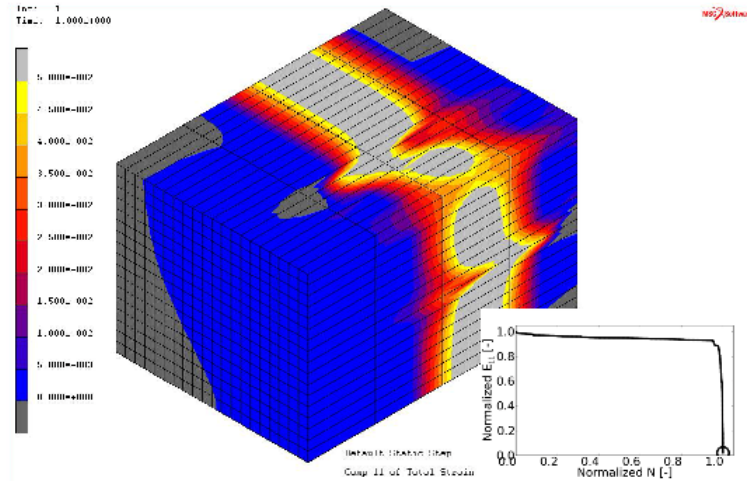
Figure 5.5: Final failure patterns of the MS7 model

5.2   Results and discussion

Fatigue modelling of the MS7 model with input fibre S-N slope parameters C_1 of -10.0, -20.0 and -30.0, and MS45 model with the input fibre C_1 value of -30.0 was performed. In each batch, 20 MS models were simulated under three ϵ_{max} levels from 2% to 4%.

The extracted Weibull shape parameter β_N, S-N slope parameter C_1 and strain-based S-N intercept parameter C_2 of the MS models are shown in Table 5.2. Compared to the MF unit cells, the fatigue life scatter of the MS models is further reduced, shown by higher β_N values. The C_1 values of the MS models are still similar to the input fibre C_1 values, because there are no additional failure mechanisms introduced during the scale-up process from the MF unit cells to the MS models. However, the MS models have smaller C_2 values than the MF unit cells. The main reason for this is that the MS models are four times longer than the MF unit cells. Therefore, statistically the MS models have a higher failure probability.

Table 5.2: Comparison of fatigue parameters of MS models

		MS7 model			MS45 model
Input fibre C_1		-10.0	-20.0	-30.0	-30.0
MS model	β_N	3.52	2.76	1.83	1.82
	C_1	-10.3	-21.0	-32.2	-32.7
	C_2	8.1	14.8	22.2	22.7

Similar fatigue parameters of the MS7 and MS45 models with the input fibre C_1 value of -30.0 are observed in Table 5.2. This indicates the composite fatigue life prediction is consistent under geometrically different scale up approaches.

The normalized E_{11} degradation curves of the MS models are plotted in Figure 5.6. At first glance, the MS models have more severe sudden-death degradation curves compared to the MF unit cells, see Figure 4.14. The decrease of the input fibre C_1 value obviously reduces the degradation rate of normalized E_{11} modulus (before failure) and reduces the scatter of the degradation curves, according to the graphs (a) to (c). For the same input fibre C_1 value, the MS45 models show more scattered normalized E_{11} degradation curves compared to the MS7 model, as shown in the graphs (c) and (d). This is because the MS45 model is coarse-meshed. Therefore, the failure progression in the MS45 model after the initial failed elements is more dispersed.

5.3 Concluding remarks

1. The geometries, initial elastic properties and fatigue simulation procedure of the MS model were introduced.

2. Fatigue simulations on the MS7 and MS45 models were performed. Both models give comparable predictions on the fatigue lives. However, MS7 model gives more consistent normalized E_{11} degradation curves compared to the MS45 fibres.

3. Compared to the single glass fibres and MF unit cells, the fatigue life scatter of the MS models is further reduced, while the extracted S-N slope parameters C_1 are not significantly different.

4. Compared to the MF unit cells, the normalized E_{11} degradation curves of the MS models are more like sudden-death curves. It appears that the degradation rate of normalized E_{11} before failure can be reduced by the decrease of the input fibre C_1 value, the same applies to the scatter of the degradation curves.

Compared to the MS45 model, the MS7 model produces more consistent degradation curves of the composite elastic properties, and therefore is selected for providing the inputs for composite fatigue simulations at
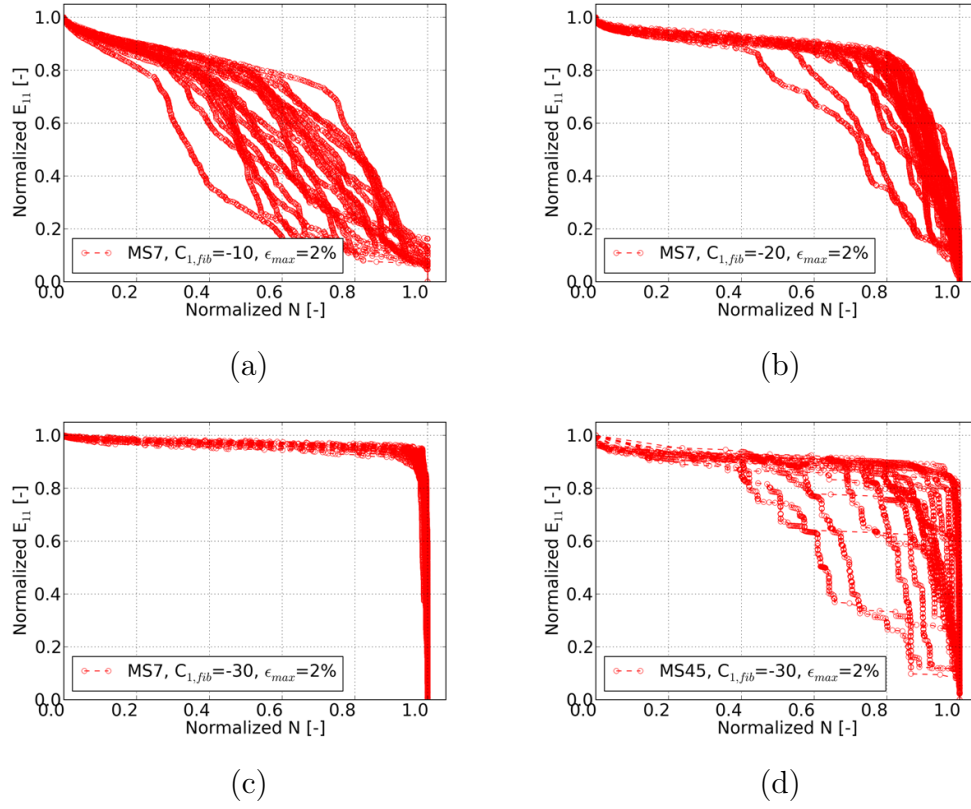
Figure 5.6: Normalized longitudinal Young's modulus degradation curves of the MS models

the macro-scale. The details of these simulations are shown in the next chapter.

Chapter 6

Numerical fatigue simulations of the CS models

In this chapter, the geometry, initial elastic properties and simulation procedure of the CS model are first described in Section 6.1. Then simulation results are shown in Section 6.2 to compare with the experimental results of the unidirectional GFRP composite dog-bone coupons. In the end, the concluding remarks are summarized in Section 6.3.

6.1   Coupon-Size models

The CS model was created as a numerical representation of the unidirectional composite dog-bone coupon. As shown in Figure 6.1, for reducing the computational time, only the gauge area was modelled. The CS model contains 600 elements equivalent to the MS7 models, although the geometrical size of its structural element ($1600{\times}1000{\times}750$ μm^3) is smaller than that of the MS7 model. Likewise, the fibre volume fraction of the CS model is the same as that of the MS7 models.

As inputs, the initial elastic properties of the CS model elements are calculated from the static simulations of the pristine MS7 models. Similar to the MS models, for an arbitrary number of elements, the elastic properties along the y- and z-axes are interchanged. The degradation of those elastic properties is done by randomly selecting a set of corresponding degradation curves (of a MS7 model) from a predefined library, which contains the degradation
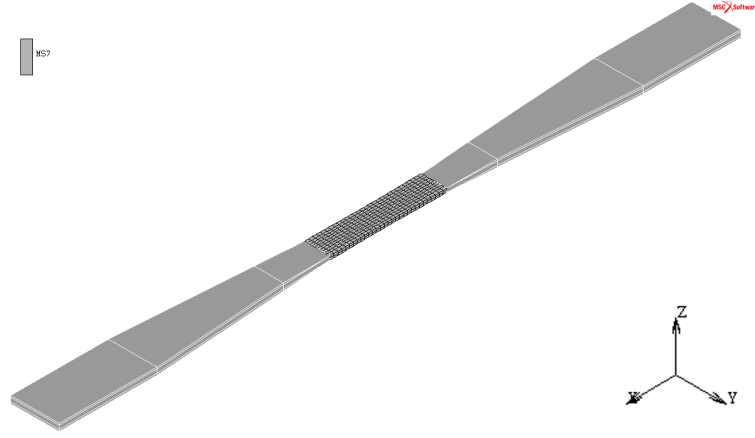
Figure 6.1: Finite element representation of a unidirectional composite dog-bone coupon

curves calculated from 20 MS7 models. The fatigue lives of the CS model elements are calculated by using Eq. 3.10 with the fatigue parameters β_N, C_1 and C_2 shown in Table 5.2.

The fatigue simulation flow chart of the CS model is identical to that in Figure 4.6. However the details of the individual steps are different with the MF unit cell and MS model. For the CS model, the simulation is run in load control mode, to allow direct comparison to the experimental data. As outputs, the fatigue model gives predictions of the CS model fatigue lives and the degradation curve of the axial stiffness (i.e. E_{11}). The calculation consists of the following steps.

1. At the beginning of the first iteration, the initial material properties of the CS model elements are defined by the predicted properties of the equivalent MS7 models. In subsequent iterations, these material properties are re-defined by the (degraded) properties calculated from the previous iteration.

2. Only the degraded E_{11} of the CS model is calculated, for comparing with the experimental axial stiffness degradation curves. The relevant boundary conditions are referred to those for calculations of the E_{11} in the MF unit cell and MS model (see Section 4.1)

3. The stress-strain state in the CS model is calculated by using a finite element simulation under σ_{max}. Opposite constant loads are applied on the ends of the CS model to match the experimental loading conditions.

4. The calculation of fatigue cycle increment at the current iteration is the same as was done for the MS45 model. Likewise, the cycle increment of fatigue cycles is calculated by $1/20$ of the remaining fatigue cycles of the next possible broken element. In the following iterations, if no elements are found broken, the cycle increment remains the same (as used in previous iteration). Otherwise, the cycle increment is updated by the remaining fatigue cycles of the new broken elements. Then in the next iteration, the increment of fatigue cycles is re-calculated by $1/20$ of the residual fatigue life of the new next possible broken element.

   For practical reasons, the calculated cycle increment less than 1 cycle is set to 0.

5. At the current iteration, elements in the MS model withstand variable fatigue loading conditions, calculated by the load redistribution as a result of the elastic properties degradation of these elements themselves. The damage of an element is described by a cumulative damage factor, which is calculated by the ratio between the cycle increment and entire fatigue life of that element. According to Palmgren-Miner Rule, the final element failure is determined when this cumulative damage factor attains unity.

6. If, at the end of that iteration, the final model failure criterion is not reached, the degraded material properties of the elements are saved for the next iteration. All elastic properties of the broken elements are directly reduced to a near-zero value (e.g. 0.001). All elastic properties of the unbroken elements are reduced by the linear interpolation values of the corresponding normalized elastic property degradation curves. These degradation curves were set up from the MS fatigue simulations indirectly based on primarily the sequential fibre breakages, and secondarily matrix failures in the MF unit cells. An example of the interpolation was shown in Figure 5.4.

7. The final failure of the simulated model is reached when failure of adjacent elements extends to the edges of the model. Figure 6.2 shows a CS model with the input fibre S-N slope parameter C_1 of -10.0 at the final failure. The corresponding normalized E_{11} degradation curve is plotted at the right-bottom corner, with the black circles showing the stage where the final failure occurs.
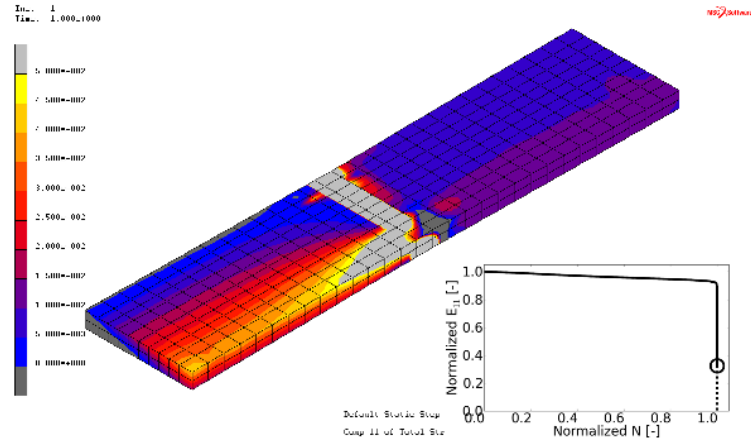
Figure 6.2: Final failure patterns of a CS model

6.2   Results and discussion

Three batches of CS models with input S-N slope parameters C_1 of fibres of -10.0, -20.0 and -30.0 were performed in load control mode. In each batch, 20 CS models were simulated with respect to three σ_{max} levels from 340 MPa to 680 MPa. The extracted fatigue parameters of the CS models are Weibull shape parameter β_N, S-N slope parameter C_1 and stress-based S-N intercept parameter C_3, shown in Table 6.1. For comparing with the MF unit cells and MS models, the strain-based S-N intercepts (i.e. C_2 parameters) of the CS models are also extracted, and shown in parentheses in Table 6.1. The ϵ_{max} levels were obtained by dividing the σ_{max} levels by the experimental E_{11} (i.e. 37600 MPa) of the dog-bone coupons.

Table 6.1: Comparison of fatigue parameters of CS models

Input fibre C_1		-10.0	-20.0	-30.0
	β_N	3.74	3.27	2.15
CS model	C_1	-10.3	-21.0	-32.2
	C_3	33.5	67.8	104.0
	C_2	(7.0)	(13.7)	(21.0)

It can be seen that the β_N values of the CS models are further increased while the C_1 values are still not affected significantly, compared to the single fibres, MF unit cells and MS models. In addition, the C_2 parameters of the CS models are reduced compared to the MF unit cells and MS models. However, this comparison of the C_2 parameters is only qualitative since the

ϵ_{max} level is not constant due to the E_{11} degradation of the CS model during the fatigue simulation.

Figure 6.3 shows the normalized E_{11} degradation curves of the CS models. The degradation of E_{11} becomes less pronounced with the decrease of input fibre C_1 value. In particular, there is almost no degradation on the graph (c) for input fibre C_1 value of -30.0.

(a)

(b)

(c)
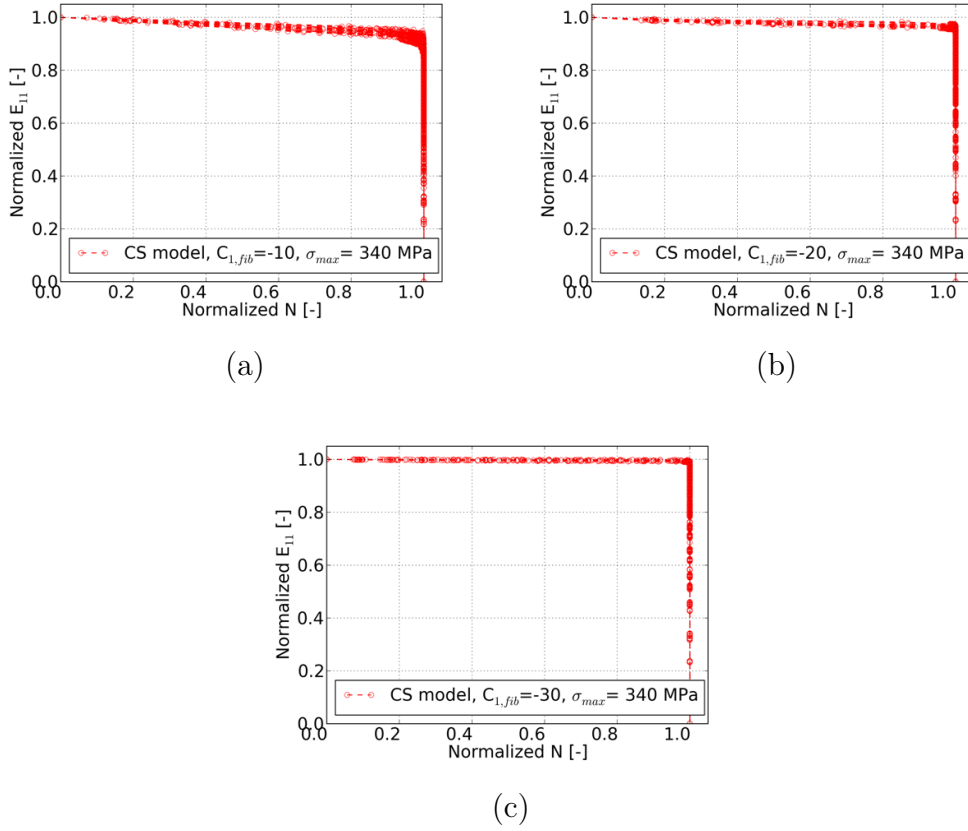
Figure 6.3: Normalized longitudinal Young's modulus degradation curves of the CS models

Since the C_1 value of the composite materials is not significantly influenced by the geometrical scale of the composite structure, the input fibre C_1 value is adjusted to the experimental C_1 value of the dog-bone coupons in the fatigue predictions of the dog-bone coupons themselves. A value of -10.0, which is close to the experimental C_1 value of the dog-bone coupons was used in the prediction of dog-bone coupon fatigue lives.

Figure 6.4 shows the predicted fatigue lives of the dog-bone specimens which are overestimated by about one order of magnitude compared to the experimental results. One possible reason is the insufficient consideration of the fatigue failure mechanisms in the dog-bone specimens. Besides the sequential fibre breakages, other micro-mechanical failure mechanisms, such as the fibre debonding [6], matrix cracking [118], etc., may also exist in the dog-bone specimens during the fatigue test. By taking these additional failure mechanisms into account, the accuracy of the fatigue life predictions might be improved.
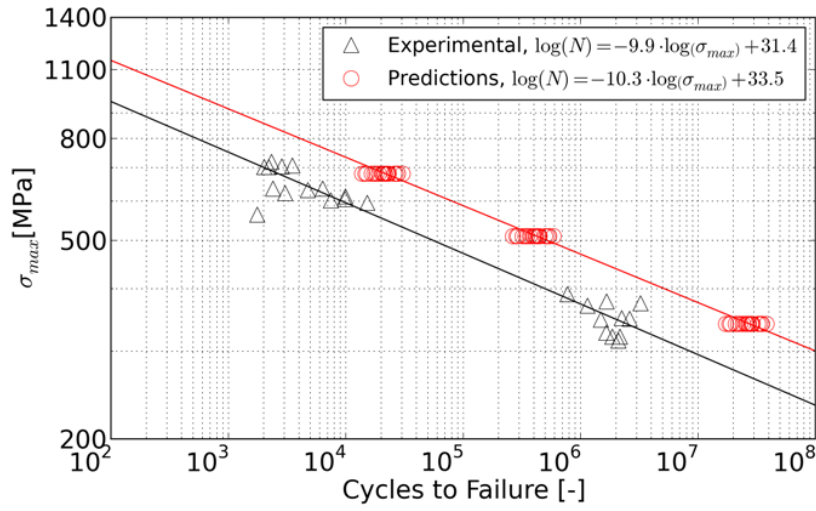
Figure 6.4: Experimental and predicted fatigue lives of the composite dog-bone coupons

Figure 6.5 shows the predicted normalized axial stiffness degradation curves of 20 CS models using the input fibre C_1 value of -10.0, in comparison with the experimental normalized axial stiffness degradation curves. The predicted normalized axial stiffness gradually degrades to approx.10% before failure, agreeing with the experimental observation from the unidirectional GFRP composite dog-bone fatigue tests.

6.3   Concluding remarks

1. The geometry, initial elastic properties and fatigue simulation proce-

Figure 6.5: Experimental and predicted normalized axial stiffness degradation curves of dog-bone specimens

dure of the CS model were introduced.

2. The same trend of the evolution of the fatigue parameters continued at the CS level. That is, compared to the single fibre, MF unit cell and MS model, the β_N value of the CS model is greatly increased, while the C_1 value is relatively constant.

3. The normalized E_{11} degradation becomes less pronounced as the input fibre C_1 value is reduced from -10.0 to -30.0.
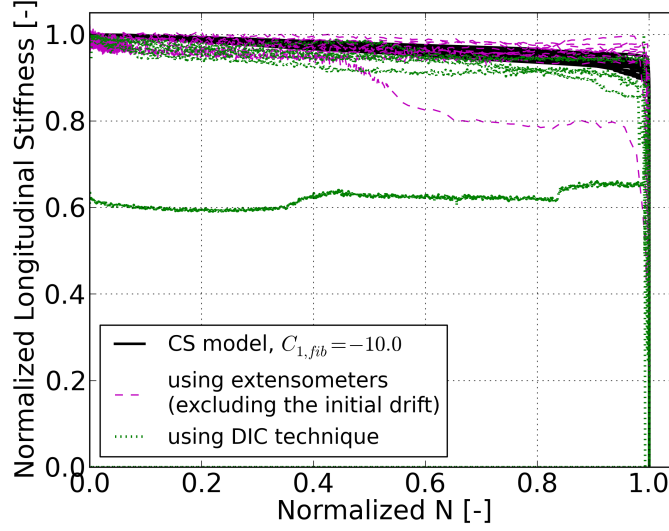
4. The final fatigue predictions were obtained with the input fibre C_1 value matching the C_1 value of the dog-bone specimens. By using the calibrated fibre C_1 value, longer fatigue lives of the dog-bone specimens were predicted, while the predicted normalized E_{11} degradation curves agreed well with the experimental observations.

So far, the entire process of predicting the axial tension-tension fatigue behaviour of unidirectional GFRP composites by using the proposed multi-scale micro-mechanical fatigue model has been demonstrated. In the next chapter, the major conclusions in this study are given, and the possible improvements for the proposed model are discussed.

Chapter 7

Conclusions and recommendations

To fulfil the goal of fatigue damage modelling in wind turbine blade laminates using micro-mechanical methods, a multi-scale finite element model was successfully developed by considering the sequential fibre breakages as the dominant failure mechanism, and was validated with coupon experimental results. At the micro-scale, the numerical composite model (so-called Multi-Fibre or MF unit cell) contains a limited number of fibres and surrounding matrix. The experimental data obtained from single fibres were used as inputs to predict the fatigue behaviour of the MF unit cell. Since the length of the fibres in the MF unit cell was too short for their strength to be experimentally measured, the fibre properties were extrapolated to that particular length from the experimental results using the weakest link theory. Next, the MF unit cell was scaled up to the meso-scale, allowing both life estimations and stiffness degradation, as the numerical model describes sequential breakages of fibres. At the next scale-up level, the Meso-Structure model consisting of 7-fibre unit cells was eventually expanded to describe the behaviour of the centre section of a dog-bone shaped fatigue test specimen, and validated both for fatigue life and stiffness degradation.

Using the proposed model, the composite fatigue lives and (degraded) elastic constants (including E_{11-33}, $\nu_{12,13,21,31,23,32}$ and $G_{12,13,21,31,23,32}$) at the micro- and meso- and macro-scales were modelled based on the material properties of the fibres and matrix. The main conclusions drawn from this work are given in Section 7.1. Then some recommendations

follow to improve the fatigue prediction accuracy in Section 7.2.

The research in this thesis can be regarded as a step forward in enabling the prediction of fatigue behaviour of composite structures, such as wind turbine blades, based on the properties of the constituents by using micro-mechanical models. However, the microscopic failures existing in a wind turbine rotor blade depend on the composite configuration and loading conditions. That is to say, in order to design a full scale blade, a large amount of additional work needs to be done in order to predict the fatigue behaviour of composite laminates with different lay-ups and under different R ratios.

7.1   Conclusions

The fatigue lives of glass fibres and composite materials were characterized by three features, the scatter, S-N slope and intercept. Experimental strain-life data were generated from fatigue tests on single fibres in the life range of 10^3-10^7 cycles. A large amount of scatter (in the order of 4 decades) was encountered. A sensitivity study on the fibre S-N slope was performed with a wide range covering from -10.0 to -30.0, to analyse how the slope parameter evolved during the numerical scaling up. The corresponding results showed this parameter was not sensitive to the composite structural scale. Therefore, according to the current model, the S-N slope of the fibres should be similar to the S-N slope found on coupons.

According to the composite simulation results at the micro-, meso- and macro-scales, the large scatter of fibre fatigue lives was significantly reduced with the increase of composite structural scales. This agreed with the experimental observation that the fatigue lives scatter of single glass fibres is much higher than that of the composite dog-bone coupons. Furthermore, with the input fibre S-N slope matching that of the coupons, the final fatigue life predictions were overestimated by approximately one order of magnitude, which can be considered a promising result. The difference is most likely due to effects not captured in the model, such as other micro-mechanical fatigue failure mechanisms (e.g. fibre debonding, matrix failure, etc.), imperfections (e.g. fibre alignment) and fibre behaviour discrepancy between embedded fibres (in surrounding matrix) and pristine fibres (without surrounding matrix).

The degraded composite elastic constants at different composite structural
scales were also calculated during the scaling-up process. As a particular
example, the normalized E_{11} (axial stiffness) degradation curves were plotted
to show the degradation trends of these composite elastic constants. This
normalized axial stiffness degradation did not significantly depend on the
fatigue load level, as observed from the experimental results of the composite
dog-bone coupons and simulation results of the MF unit cells. It has been
found that the normalized axial stiffness degradation curves exhibited more
clustered and sudden-death behaviour by either scaling up the structural
scales (from micro- to macro-), or decreasing the input fibre S-N slope (from
-10.0 to -30.0) at the same scale. Moreover, the final predictions of the
normalized axial stiffness degradation curves of composite dog-bone coupons
agreed well with the experimental results, when the matching fibre S-N slope
was considered.

7.2   Recommendations

On the basis of current research, the accuracy of predictions of the proposed
model obviously depends on the input fibre properties. Several improvements
in fibre characterisation are discussed in these followings.

1. More single fibre tests shall be performed for accurate determination
   of fibre tensile failure strains. On these fibre tests, individual stiffness
   measurements on the single fibre tests might help to evaluate the test
   results. It is possible that the 2-parameter Weibull distribution func-
   tion is not sufficient enough to characterize fibre static behaviour when
   analysing these more fibre test results. In that case, a multi-modal
   Weibull distribution function has to be considered, as mentioned in
   Section 2.2.1.

2. The Weibull parameters obtained from the single fibre tests shall be
   compared with the values obtained from the other methods, such as
   the fibre bundle tests and single fibre fragmentation tests discussed in
   Appendix A.2 and A.3 respectively.

3. For improving the statistical confidence in the input fibre S-N slope
   parameter, the sample of fibre fatigue lives should either be greatly
   enlarged, or the range of load levels should be enlarged to an extremely
   long fatigue cycle region (up to 10^{10} cycles or higher). For the latter

option, a high frequency fatigue testing facility is required to be able to perform the long cycle fibre fatigue tests. A benefit of this option would be that the fibre behaviour at low load levels can be based on experiments rather than extrapolation, and that the validity of the power law for fibre fatigue can be checked.

4. A link with existing residual strength methods may assist in evaluating the first-cycle breakage results. Digital Image Correlation (DIC) was used to evaluate strains in the coupon specimens. Adopting this technology to single fibre tests may provide useful information along with the other recommended improvements in test methodology. On the other hand, elaborate Scanning Electron Microscope (SEM) observations on the fibre crack surfaces may reveal hints on the underlying mechanisms of fibre fracture and help to explain the very large scatter that is generally observed in this type of experiments. This will be helpful to figure out if the weakest link theory is the best theory to calculate the properties of fibres with micrometre gauge lengths, or some other alternatives should be employed.

A striking observation from this study is that the very large scatter observed in fatigue data of single fibres reduces to about a single decade of scatter for coupon sized composite specimens. The model captures this phenomenon accurately, but the underlying mechanism should be further investigated. This is essential for achieving a higher prediction accuracy of the MS and CS models by providing more reliable composite fatigue degradation curves at the micro-scale.

1. Microscopic observation or other experimental techniques could be used to investigate the initiation and propagation of damage. These observations could be used for clarifications of the offset in life prediction found in this study, and provide guidance for further developments of the model as mentioned above. Combining such an experimental effort with model development would also provide tools to validate future model developments.

2. As discussed in Section 2.2, the fibre/matrix interface failure (i.e. fibre debonding) is an important failure mechanism affecting the sequential fibre breakages in the MF unit cells. The onset of fibre debonding depends on the fibre/matrix interface behaviour, which can be characterised by the methods introduced in Appendix A.3 to A.6.

3. The matrix damage will be another consideration of the MF unit cells. In this thesis, the matrix damage is only assumed to occur as a result of the breakages of polymer chemical bonds, which is caused by the large stress concentration near the fibre breakage. However, in practice, the matrix elements may fail earlier than expected due to matrix plasticity and defects (such as micro-voids, etc.). Therefore, the assumption to describe the matrix failures needs to be relaxed to allow these above-mentioned failures. This would result in more extensive matrix damage which will affect the stress distribution and thus fatigue life.

From a design perspective, the composite fatigue properties with different fibres and matrix could be investigated at the micro- to macro-scales. This work can be carried out by adapting the specific material properties of the fibres and matrix in the proposed model and its future updates.

Appendix A

Test methods for characterizations of fibres and fibre/matrix interface

Properties of fibres and fibre/matrix interface can be extracted by various approaches, where the focus of analysis is different. In general, the approaches of extracting fibre tensile strength (or failure strain) are single fibre tests A.1, fibre bundle tests A.2 and fibre fragmentation tests A.3. Whereas the approaches of extracting fibre/matrix Interface Shear Strength (ISS) are fibre fragmentation tests A.3, fibre pull-out tests A.4, fibre micro-bond tests A.5 and micro-indentation tests A.6.

A.1 Single fibre tests

Figure A.1 illustrates a single fibre tensile test, performed by ASTM standard D3379-75 which is, however, withdrawn in 1998 since no update comes after [8]. From a batch of experimental results, Weibull parameters of Eq. 2.1 can be obtained by either Linear Regression (LR) method or Maximum Likelihood Estimation (MLE) method.

In the LR method, failure probability P can be estimated by Eq. A.1.

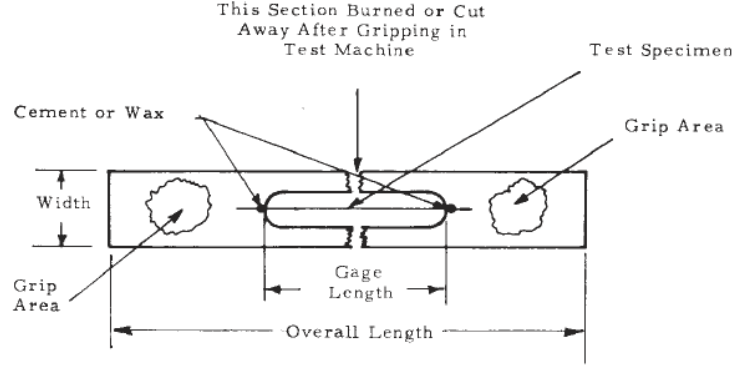$$P = \frac{i - 0.3}{n + 0.4} \tag{A.1}$$

Figure A.1: Illustration of a single fibre tensile test (reproduced from [8])

in which, i is the rank number of certain test and n is the number of tests. Then Weibull parameters can be extracted from the slope and intercept of the plot $\ln(-\ln(1-P))$ vs. $\ln(\sigma)$.

In the MLE method, the likelihood function Eq. A.2 is defined as the product of all probability densities of fibre strengths, which is

$$L(\beta_S, \sigma) = \prod_{i=1}^{n} p_f(\beta_S, \sigma) \tag{A.2}$$

in which L is the likelihood function, p_f is probability density function of the selected Weibull distribution of parameters β_S and σ_0. For instance, p_f of Eq. 2.1 is shown in Eq. A.3.

$$p_f(\beta_S, \sigma_0) = (\frac{l}{l_{ref}})(\frac{\beta_S}{\sigma_0})(\frac{\sigma}{\sigma_0})^{(\beta_S-1)} \exp\{-(\frac{l}{l_{ref}})(\frac{\sigma}{\sigma_0})^{\beta_S}\} \tag{A.3}$$

Then Weibull parameters are solutions from binary equations Eq. A.4 where the estimator of likelihood function becomes the maximum.

$$\frac{\partial(L(\beta_S, \sigma_0))}{\partial \beta_S}\big|_{\beta=\hat{\beta}_S} = 0 \; and \; \frac{\partial(L(\beta_S, \sigma_0))}{\partial \beta_S}\big|_{\sigma_0=\hat{\sigma}_0} = 0 \tag{A.4}$$

in which $\hat{\beta}_S$ and $\hat{\sigma}_0$ are the binary equation solutions.

A.2 Fibre bundle tests

Figure A.2 illustrates a fibre bundle specimen, used to extract the Weibull parameters of fibre tensile failure strains [9, 102, 119–125]. A generalized
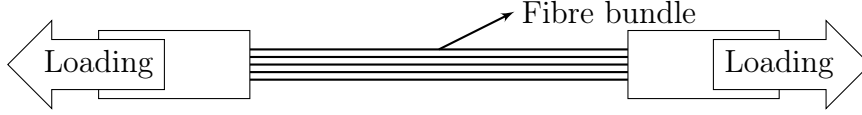

Figure A.2: Illustration of a fibre bundle specimen

model Eq. A.5 to describe the fibre bundle load/strain curve was developed by Phoenix [125].

$$F_{real} = n_f \times E_f \times A_f \times \int_0^\epsilon f(\epsilon - x) \times g(s)\mathrm{d}x \tag{A.5}$$

in which n_f is the number of fibres in the bungle. E_f and A_f are fibre modulus and cross-sectional area, F_{real} is the applied load under strain ϵ. Function f denotes the product of the strain and the survival probability under that strain, i.e. $\epsilon \times P_s(\epsilon)$. Function g denotes the probability density function of the slack lengths. Different slack length density functions including the Dirac distribution, uniform distribution, triangular distribution, etc., were compared in the studies by Phoenix [125] and Creasy [120]. When slack fibres are not dominant, it is accurate enough to predict the slack length of fibres using the uniform distribution. The expression of the uniform distribution is

$$g(\epsilon) = \begin{cases} 1/\epsilon_r & \text{when } 0 \leq \epsilon \leq \epsilon_r \\ 0 & \text{elsewhere} \end{cases} \tag{A.6}$$

in which, ϵ_r is the fibre strain with the maximum slack length. Substitution of Eq. A.6 into Eq. A.5 results in Eq. A.7

$$F_{real} = n \times E_f \times A_f \times 1/\epsilon_r \times \int_{\epsilon-\epsilon_r}^\epsilon x \times P_s(x)\mathrm{d}x \tag{A.7}$$

In the case of no slack fibres, Eq. A.7 reduces to Eq. A.8.

$$F_{real} = n \times E_f \times A_f \times \epsilon \times P_s(x) \tag{A.8}$$

By Eq. A.9, the fibre survival probability $P_s(\epsilon)$ at each strain is calculated

by the ratio between the F_{real} and a imaginary load F_{img} where no fibre is assumed broken under the same strain level. A demonstration of F_{real} and F_{img} is shown in Figure A.3.

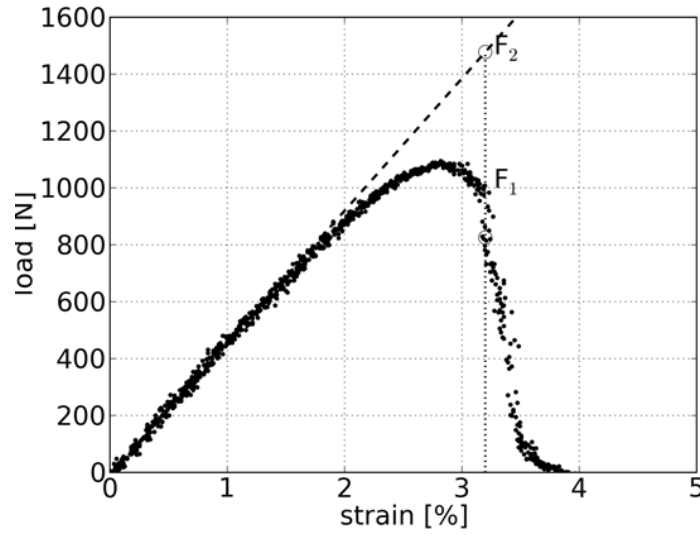$$P_s(\epsilon) = \frac{F_{real}}{F_{img}} \tag{A.9}$$

Figure A.3: Illustrations of fibre survival probability from a fibre bundle load-strain curve (reproduced from [9])

The plot of $\ln(-\ln(P_s))$ vs. $\ln(\epsilon)$ is shown in Figure A.4. It is clear that the regression of survival probabilities violates increasingly the linear relationship represented by a two-parameter Weibull function. Andersons [126] used the first linear part to calculate the Weibull parameters for single fibre strength.

Carlard [123] studied the possible factors that affect load-strain curves of fibre bundles, and found that the violation is primarily because of the local load sharing phenomenon by fibre interactions (such as frictions). Further, Okoroafor [124] monitored the sequence of fibre breaks in a bundle by acoustic emission technique and found that fibre breaking is dominated by a mix of simplex failure mechanisms (such as singlet, doublet, triplet, quartet, ect.). The multiple failure mechanisms can be regarded as the results from fibre interactions. Higher level failure mode means more severe local load transfers
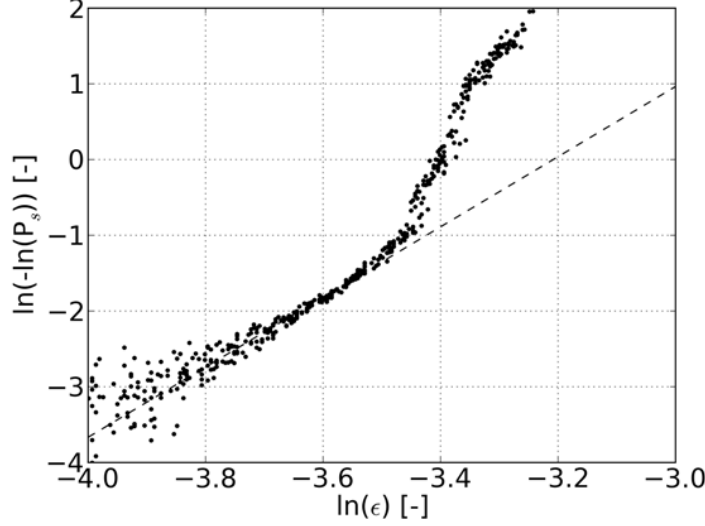
Figure A.4: Plot of $\ln(-\ln(P_s))$ vs. $\ln(\epsilon)$ (reproduced from [9])

because of fibre interactions. Therefore, by assuming that all fibre failure mechanisms follow a 2-parameter Weibull distribution function, Okoroafor proposed a series based model to calculate fibre survival probability, which is

$$P_s(\epsilon) = \exp\{-\frac{l}{l_{ref}} \times \sum_{i=1}^{n} c_i (\frac{\epsilon}{\epsilon_{0i}})^{\beta_i}\} \tag{A.10}$$

in which, index i denotes the type of failure mechanisms include from singlet fibre breakage ($i = 1$) to n-rank fibre breakage ($i = n$), c_i is the weight factors measured by the acoustic emission equipment in failure mode i, β_i and ϵ_{0i} are Weibull parameters of fibre failure strains in failure mode i. Okoroafor indicated that the relationship among Weibull parameters of different failure mechanisms is:

$$\beta_i = i \times \beta \text{ and } \epsilon_{i0} = \epsilon_{avg} \times (\beta_i)^{1/\beta_i} \tag{A.11}$$

where ϵ_{avg} is the average failure strain of fibres. However, the calculation of Weibull scale parameter ϵ_{0i} is questionable since it deviates from the Weibull properties.

A.3   Fibre fragmentation tests

Figure A.5 illustrates a single fibre fragmentation test, which can be used to characterize both Weibull parameters of fibre tensile strengths and fibre/matrix ISS, depending on the interests.
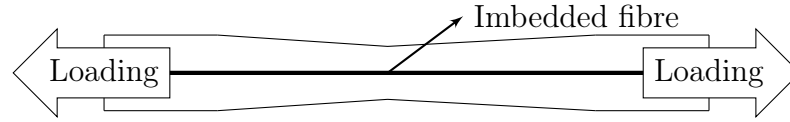

Figure A.5: Illustration of a single fibre fragmentation test

During the fibre fragmentation test where the applied loads are increasing, the embedded fibre is being broken into small pieces, and becomes saturated. The number of fragments is assumed to follow the Poisson distribution Eq. A.12 [127, 128]

$$P_k = \frac{(l_{seg}\lambda)^k \exp(-l_{seg}\lambda)}{k!} \tag{A.12}$$

in which P_k is the probability to have k fragments in that specimen, l_{seg} is the length of the fibre fragmentation specimen, and λ is the fragment density. Therefore, the product of l_{seg} and λ gives the mean value of k.

By considering an extreme condition, in which the fibre only break once within the length l_{seg}, fibre failure probability P can be calculated by Eq. A.13, since the limitation of $(l_{seg}\lambda)^k/k!$ becomes to unity.

$$P = 1 - P_{k=0} = 1 - \exp(-l_{seg}\lambda) \tag{A.13}$$

If the fibre failure probability P is also assumed to follow Eq. 2.1, then the relationship between fragment density λ and applied load σ of the fibre fragmentation specimen can be obtained in Eq. A.14, by comparing Eq. 2.1 and Eq. A.13.

$$\lambda = \frac{1}{l_{ref}}(\frac{\sigma}{\sigma_0})^{\beta_S} \tag{A.14}$$

Then the number of fragments n_{seg} can be calculated by the integration of

λ, as shown in Eq. A.15.

$$n_{seg} = \int_0^{l_{seg}} \lambda_{max}(x)\mathrm{d}x = \int_0^{l_{seg}} \frac{1}{l_{ref}}(\frac{\sigma_{max}(x)}{\sigma_0})^{\beta_S}\mathrm{d}x \qquad (A.15)$$

in which λ_{max} is the maximum crack density of an arbitrary place x over the length, and σ_{max} is the maximum tensile stress applied on the arbitrary place x. The reason to use λ_{max} and σ_{max} in Eq. A.15 is that in the vicinity of fibre fracture the tensile stress is dropped from the maximum stress, but the crack density should be kept constant since cracks have been already formed. Experimentally, the number of fragments n_seg can be measured by optical microscopes or acoustic emission techniques [127–131]. At the beginning of a single fibre fragmentation test, constant stress σ(i.e. σ_{max}) can be assumed along the fibre since fewer fragments are found. Then Eq. A.16 is derived. Then the Weibull parameters of fibre strengths can be extracted from the linear part of the plot of $\ln(n_{seg})$ with respect to $\ln(\sigma_{max})$.

$$n_{seg} = \frac{l_{seg}}{l_{ref}}(\frac{\sigma(x)}{\sigma_0})^{\beta_S} \qquad (A.16)$$

For measuring fibre/matrix ISS, the fibre fragmentation test works only in the case that the matrix failure strain is at least three times as large as the fibre failure strain, based on a rule-of-thumb [11]. The fibre/matrix ISS can be calculated from the fragment lengths, which are usually observed by optical microscopes, acoustic emission techniques, etc. [11, 129, 132–146].

Kelly and Tyson [136] developed Eq. A.17 to calculate the fibre/matrix ISS.

$$\tau_{max} = \frac{\sigma_{fc}d_f}{2l_{seg,cr}} \qquad (A.17)$$

in which τ_{max} is the fibre/matrix ISS, d_f is the fibre diameter, $l_{seg,cr}$ is the critical fibre fragment length beyond which fibre axial normal stress is recovered large enough to cause a new fibre breakage, and σ_{fc} is the tensile strength when the critical fibre fragment length is obtained.

However, the observed fibre fragment lengths are usually statistically distributed and not equalled to $l_{seg,cr}$. Wimolkiatisak and Bell [138] argued the fibre fragment lengths should be in the range between $l_{seg,cr}/2$ and $l_{seg,cr}$, because the fibre fragment longer than $l_{seg,cr}$ has the opportunity to break into 2 pieces (both of which are shorter than $l_{seg,cr}$ but longer than $l_{seg,cr}/2$). Therefore, Wimolkiatisak assumed the average fragment length $L_{seg,avg}$ equalling

to $3l_{seg,cr}/4$. On the other hand, $L_{seg,avg}$ can be obtained by calculating the arithmetic average of all observed fragment lengths or by Eq. A.18 if the fragment lengths are assumed to follow a Weibull distribution [139, 141].

$$L_{seg,avg} = l_{seg,0}\Gamma(1 + 1/\beta_{seg}) \tag{A.18}$$

in which β_{seg} and $l_{seg,0}$ are Weibull shape and scale parameters of fibre fragment lengths. As a result, Eq. A.19 to finally calculate fibre/matrix ISS is derived by substituting Eq. A.18 into Eq. A.17 [138]. In Eq. A.19, σ_{fc} has to be calculated separately from a fibre strength model taking into account the length effect, for instance the modified 2-parameter Weibull distribution Eq. 2.1.

$$\tau_{max} = \frac{3\sigma_{fc}d_f}{8l_{seg,0}\Gamma(1 + 1/\beta_{seg})} \tag{A.19}$$

Drzal et al [139] proposed an alternative expression Eq. A.20 derived from Eq. A.17 to calculate the fibre/matrix ISS.

$$\tau_{max} = \frac{\sigma_{fc}}{2\alpha}\Gamma(1 - 1/\beta_{ld}) \tag{A.20}$$

in which β_{ld} and α are Weibull shape and scale parameters of the ratio $l_{seg,cr}/d$. The term in the gamma function should be corrected by $1 + 1/\beta_{ld}$, according to Weibull distribution properties. In general, the fibre/matrix ISS calculation by Eq. A.20 is higher than the calculation by Eq. A.19 [138].

The drawback of using the single fibre fragmentation test to calculate the fibre/matrix ISS is that the fibre-to-fibre interaction is not considered. This fibre-to-fibre interaction is caused by the load redistribution from the broken fibres to the neighbouring fibres. For solving this problem, multiple fibre fragmentation tests are developed [142–146]. In the multiple fibre fragment test, the fibre/matrix ISS is still calculated by Eq. A.19. However, due to the fibre-to-fibre interaction, the fibre/matrix ISS calculation is influenced by more factors, for instance the fibre volume fraction [142], the fibre-to-fibre spacing distance [143], etc. In conclusion, the upper and lower bounds of the fibre/matrix ISS can be obtained from the single fibre fragmentation tests and multiple fibre fragmentation tests with short fibre-to-fibre spacing distance.

A.4   Fibre pull-out tests

Figure A.6 illustrates a fibre pull-out test. The fibre is planted vertically with a controlled embedded length in a block of uncured matrix. After a curing treatment, fibre is pulled out from the matrix droplet by a very slow rate. The fibre/matrix ISS can be characterized by shear strength or critical energy release rate.
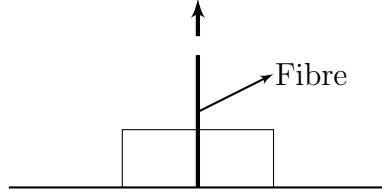

Figure A.6: Illustration of a fibre pull-out test

The fibre/matrix interface shear stress τ over the embedded length is calculated by the equilibrium function Eq. A.21

$$\tau = \frac{r_f}{2}\frac{\mathrm{d}\sigma}{\mathrm{d}x} \tag{A.21}$$

in which E_f is the fibre Young's modulus, r_f is the fibre radius and σ is the fibre axial normal stress at location x. Because of the shear lag effect, σ is not evenly distributed over the embedded length. Chua and Piggott [11] calculated σ by a model Eq. A.22 similar to Cox's shear-lag model Eq. 2.4

$$\sigma = \sigma_t \frac{\sinh[\psi(l_{em}-x)/r_f]}{\sinh(\psi l_{em}/r_f)} \text{ where } \psi = \{\frac{E_m}{E_f}(\frac{1}{(1+\nu_m)\ln(r_m/r_f)})\}^{1/2} \tag{A.22}$$

in which σ_t is the fibre pull-out strength, l_{em} is embedded length, E_m and E_f are Young's moduli of matrix and the fibre, ν_m and r_m are the Poisson's ratio and radius of matrix. Substitution of Eq. A.22 into Eq. A.21 gives rise to the final calculation of fibre/matrix interface shear stress by Eq. A.23. According to Eq. A.23, the calculated τ value is dependent on many issues, such as fibre diameter, fibre embedded length and fibre/matrix stiffness ratio, etc. In practice, a strong diversion of the calculated τ value among is found

among different test facilities [11, 132–134].

$$\sigma = \psi\sigma_t\frac{\cosh[\psi(l_{em} - x)/r_f]}{2\sinh(\psi l_{em}/r_f)} \text{ where } \psi = \{\frac{E_m}{E_f}(\frac{1}{(1 + \nu_m)\ln(r_m/r_f)})\}^{1/2}$$

$$(A.23)$$

Instead of the fibre/matrix ISS, Hampe et al [10] developed an energy release rate based criterion to characterize fibre/matrix interface property. As shown in Figure A.7, they divided the load-displacement curve of a fibre pull-out test into three regions, which are elastic deformation region (AB), fibre debonding region (BCD) and fibre friction region (DE). The critical energy release rate E_{cr} to make fibre fully debonding is then calculated by Eq. A.24.

$$E_{cr} = \frac{A_{BCD}}{2\pi l_{em} r_f}$$

$$(A.24)$$

in which A_{BCD} is the area where the debonding work is determined. Unfortunately, Hampe pointed out the critical energy release rate criterion E_{cr} can only be used for the brittle matrix composites. For ductile matrix, the area BCD is not obvious to be detected.
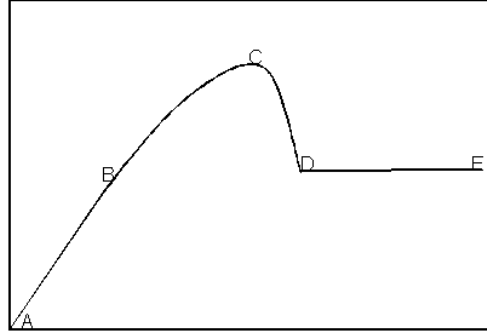

Figure A.7: The load-displacement curve of a fibre pull-out test (reproduced from [10])

A.5   Fibre micro-bond tests

Figure A.8 illustrates a fibre micro-bond test. The fibre micro-bond specimen is produced by curing a fibre in a matrix droplet. After that the fibre micro-bond specimen is placed in between two knife edges (or small metal

blocks [134]). The calculated fibre/matrix ISS depends on not only fibre diameter, embedded length, but also geometry and symmetry of the matrix droplet, variations of concentrations of hardener in the matrix droplet, etc. [11]. Eq. A.25 shows the formula to calculate fibre/matrix ISS, by assuming a constant interfacial stress τ over the embedded length.

$$\tau_{max} = \frac{F_{de}}{\pi d_f l_{em}} \tag{A.25}$$

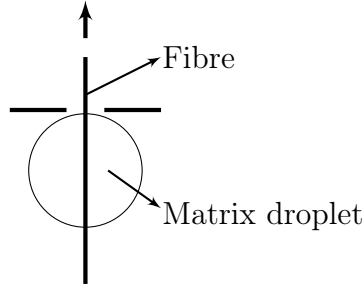in which F_{de} is the debonding force, d_f and l_{em} are fibre diameter and embedded length.

Figure A.8: Illustration of a fibre micro-bond test (reproduced from [11])

The calculated fibre/matrix ISS also depends on the position of the supporting knife-edges, where matrix cracks might be induced during the fibre micro-bond test. Nishikawa and his colleagues [135] investigated the effects of knife-edge position on the fibre/matrix ISS calculation. From their experimental and numerical simulation results, they found that if the knife-edges are too close, the matrix crack formed from the knife-edge position will propagate to fibre/matrix interface, resulting in a significant reduction on the debonding force. On the contrary, if the knife-edges are far enough, for instance twice the fibre diameter from one knife-edge to the fibre, the matrix crack will hardly reduce the debonding force. Therefore, they proposed to use the convergence (to the upper limit) of a batch of experimental debonding forces to calculate the fibre/matrix ISS.

A.6   Micro-indentation tests

Figure A.9 illustrates a micro-indentation test. A section of composite specimen is carefully polished and placed in the testing machine. Then com-

pressive load is applied through an indenter on a single fibre which is not contacted by any other fibres. Note that the diameter of the indenter should be smaller than the selected fibre, in order to produce a nice single fibre debonding. A large enough maximum indented displacement should also be set to make sure debonding occurs during the test. The advantage of micro-indentation tests is that the fibre/matrix ISS can be directly measured on the macroscopic composite specimen.
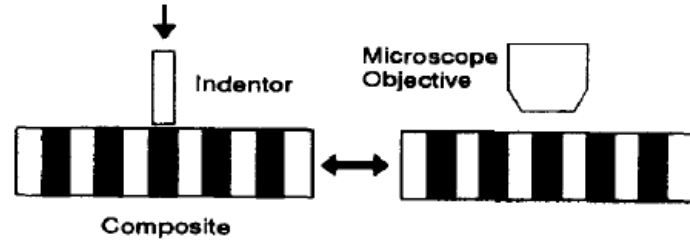

Figure A.9: Illustration of a micro-indentation test (reproduced from [11])

In early studies of micro-indentation tests, the fibre/matrix ISS is calculated by FE element models. One reason is because an accurate analytical solution of the stress state of and around the indented fibre is difficult to get since the indenter only contact the fibre top surface in part [133, 147]. Another reason is that the fibre debonding point is very difficult to be detected from a load-indented displacement curve. For instance, Figure A.10 shows an example of a load-indented displacement curve of a unidirectional GFRP specimen by curve (a). It can be seen there is no evident curvature change to point out the fibre debonding on that indentation curve.

Kharrat et al [148] and Zidi et al [12, 149] developed an analytical calculation of the fibre/matrix ISS from Cox's shear lag model Eq. 2.4. They divided the original indentation displacement u_i into two contributions, the displacement u_{ep} due to fibre elastic-plastic deformation and the fibre compressive displacement u_f, which is also called reduced displacement in [148]. The displacement u_{ep} can be measured by the micro-indentation test on a bulk glass specimen with the same indentation rate, or empirically modelled by a power law Eq. A.26 [150].

$$u_{eq} = KP^m \tag{A.26}$$

in which K and m are fit parameters. Curve (b) in Figure A.10 shows an example of the indentation curve of a bulk glass specimen. Then the reduced
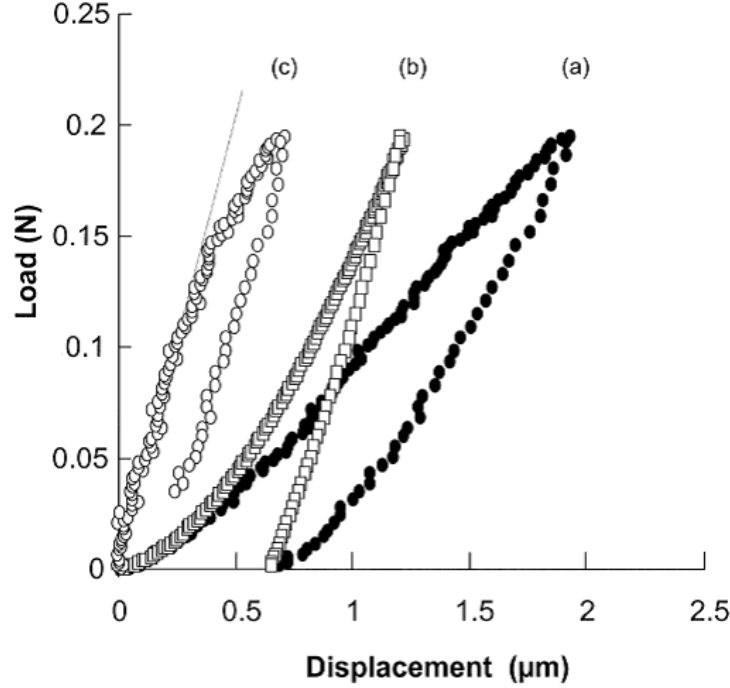
(a) Indentation curve of the composite (b) Indentation curve of the bulk
glass (c) Reduced indentation curve of the composite

Figure A.10: An example of load-indented displacement curve (reproduced
from [12])

displacement u_f can be calculated by removing u_{eq} from u_i. Curve (c) in
Figure A.10 shows the reduced displacement uf calculating by eliminating
curve (b) from curve (a). From curve (c), the debonding load can be detected
as the first value deviating from the linear part of the curve.

The governing equilibrium equation calculate the stress state of the indented
fibre is shown in Eq. A.27.

$$\frac{\partial^2 \sigma}{\partial x^2} - \phi^2 \sigma = -\phi^2 \sigma_\infty \tag{A.27}$$

in which σ and σ_∞ are fibre axial normal stress at location x and the far-
away ends, ϕ is the shear-lag parameter. For solving Eq. A.27, two following
boundary conditions are considered. Firstly, it is assumed that the indented

force F_{in} on the fibre top surface is evenly distributed. That means

$$\sigma(x = 0, r) = \frac{F_{in}}{\pi r_f^2} \tag{A.28}$$

Secondly, the fibre radius is assumed much smaller than the fibre length (i.e. the axial thickness of the specimen). That means

$$\sigma(x = \infty, r) = 0 \tag{A.29}$$

The solution is then shown in Eq. A.30.

$$\sigma(x) = \frac{F_{in}}{\pi r_f^2} \exp(-\psi x) \text{ where } \psi = \{\frac{G_m}{E_f}[\frac{2\pi}{A_f(\ln(s/r_f))}]\}^{1/2} \tag{A.30}$$

in which E_f is the fibre Young's modulus, G_m is the matrix shear modulus, s is the centre-to-centre distance of fibres and r_f is the fibre radius. The fibre/matrix ISS can be calculated by the fibre mechanical equilibrium equation, that is

$$\tau(x) = -\frac{1}{2}\frac{d\sigma(x)}{dx} = \frac{\psi F_{in}}{2\pi r_f} \exp(-\psi x) \text{ where } \psi = \{\frac{G_m}{E_f}[\frac{2\pi}{A_f(\ln(s/r_f))}]\}^{1/2} \tag{A.31}$$

Eq. A.31 shows the maximum fibre/matrix ISS is obtained at the region $x = 0$, where F_{in} reaches the inflection point $F_{in,cr}$ in the load-reduced displacement curve, that means

$$\tau_{max} = \frac{\psi F_{in,cr}}{2\pi r_f} \text{ where } \psi = \{\frac{G_m}{E_f}[\frac{2\pi}{A_f(\ln(s/r_f))}]\}^{1/2} \tag{A.32}$$

Bibliography

[1] Nijssen R. P. L. *Fatigue Life Prediction and Strength Degradation of Wind Turbine Rotor Blade Composites*. PhD thesis, Delft University of Technology, 2006.

[2] Talreja R. *Fatigue of Composite Materials*. Technomic Inc., 1987.

[3] Ladevéze P. and Genet M. A new approach to the subcritical cracking of ceramic fibers. *Compos. Sci. Technol.*, 70:1575–1583, 2010.

[4] Zinck P., Pays M. F., Rezakhanlou R., and Gerard J. F. Mechanical characterisation of glass fibres as an indirect analysis of the effect of surface treatment. *J. Mater. Sci.*, 34:2121–2133, 1983.

[5] Sjögren A., Joffe R., Berglund L., and Mäder E. Effects of fibre coating (size) on properties of glass fibre/vinyl ester composites. *Composites Part A*, 30:1009–1015, 1999.

[6] Pupurs A. and Varna J. Ud composite in mechanical fatigue: modeling multiple fibre breaks and debond growth. In *Proceedings of 17th International Conference on Composite materials*, Edinburgh, UK, July 2009.

[7] Diao X., Ye L., and Mai Y. A statistical model of residual strength and fatigue life of composite laminates. *Compos. Sci. Technol.*, 54:329–336, 1995.

[8] *Standard Test Method for Tensile Strength and Young's Modulus for High-Modulus Single-Filament Materials*. ASTM standard D3379-75r98.

[9] Qian C., Nijssen R. P. L., Jansen E. L., van Delft D. R. V., Gürdal Z., and Zhang G. Q. Micro-mechanical modelling of wind turbine rotor

blade composites – static properties of fibre bundles. In *Proceedings of European Wind Energy Conference and Exhibition*, Marseille, France, March 2009.

[10] Kalinka G. Meretz S. Hampe, A. and E. Schulz. An advanced equipment for single-fibre pull-out test designed to monitor the fracture process. *Composites*, 26:40–46, 1995.

[11] Chua P. S. and Piggott M. R. The glass fibre-polymer interface: I. theoretical consideration for single fibre pull-out tests. *Mater. Sci. Technol.*, 22:33–42, 1985.

[12] Zidi M., Carpentier L., Chateauminois A., and Sidoroff F. Quantitative analysis of the micro-indentation behavior of fibre-reinforced composites: development and validation of an analytical model. *Compos. Sci. Technol.*, 60:429–437, 2000.

[13] Mandell J. F., Reed R. M., and Samborsky D. D. Fatigue of fiberglass wind turbine blade materials. Technical report, Montana State University, August 1992. Sandia National Laboratory contractor report: SAND92-7005.

[14] van Delft D. R. V., de Winkel G. D., and Joosse P. A. Fatigue behaviour of fibreglass wind turbine blade material under variable amplitude loading. In *AIAA/ASME Wind Energy Symposium, no. AIAA-97-0951*, Reno, Nevada, USA, 1997.

[15] http://www.wmc.eu/focus6.

[16] Downing S.D. and Socie D.F. Simple rainflow counting algorithms. *Int. J. Fatigue*, 4:31–40, 1982.

[17] Miner M. A. Cumulative damage in fatigue. *J. Appl. Mech.*, 12:159–164, 1945.

[18] Sendeckyj J. P. Constant life diagrams - a historical review. *Int. J. Fatigue*, 23:347–353, 2001.

[19] Degrieck J. and van Paepegem W. Fatigue damage modelling of fibre-reinforced composite materials: Review. *Appl. Mech. Rev.*, 54:279–300, 2001.

[20] Whitworth H. A. Evaluation of the residual strength degradation in composite laminates under fatigue loading. *Compos. Struct.*, 48:261–264, 2000.

[21] http://www.wmc.eu/optimatblades_optidat.php.

[22] Mishnaevsky Jr. L. Hierarchical composites: Analysis of damage evolution based on fiber bundle model. *Compos. Sci. Technol.*, 71:450–460, 2011.

[23] Qing H. and Mishnaevsky Jr. L. Fatigue modeling of materials with complex microstructures. *Comput. Mater. Sci.*, 50:1644–1650, 2011.

[24] Li S., Singh C. V., and Talreja R. A representative volume based on translational symmetries for fe analysis for cracked laminates with two arrays of cracks. *Int. J. Solids Struct.*, 46:1793–1804, 2009.

[25] Curtin W. A. Theory of mechanical properties of ceramic matrix composites. *J. Am. Ceram. Soc.*, 74:2837–2845, 1991.

[26] Curtin W. A. Tensile strength of fiber-reinforced composites: II. application to polymer matrix composites. *J. Compos. Mater.*, 32:2060–2081, 1998.

[27] Curtin W. A. Tensile strength of fiber-reinforced composites: III. beyond the traditional weibull model for fiber strengths. *J. Compos. Mater.*, 34:1301–1332, 2000.

[28] Phoenix S. L., Ibnabdeljalil M., and Hui C. Y. Size effects in the distribution for strength of brittle matrix composites: analysis and monte-carlo simulation. *Int. J. Solids Struct.*, 34:545–568, 1997.

[29] Harlow D. G. and Phoenix S. L. The chain-of-bundle probability model for the strength of fibrous materials: I. analysis and conjectures. *J. Compos. Mater.*, 12:195–214, 1978.

[30] Harlow D. G. and Phoenix S. L. The chain-of-bundle probability model for the strength of fibrous materials: II. a numerical study of convergence. *J. Compos. Mater.*, 12:314–334, 1978.

[31] Okabe T., Takeda N., Kamoshida Y., Shimizu M., and Curtin W. A. A 3d shear-lag model considering micro-damage and statistical strength prediction of unidirectional fiber-reinforced composites. *Compos. Sci. Technol.*, 61:1773–1787, 2001.

[32] Markov K. Z. *Heterogeneous Media: Modelling and Simulation*, chapter 1. Elementary Micromechanics of Heterogeneous Media. Birkhauser, Boston, 1999.

[33] Reifsnider K. L. The critical element model: A modelling philosophy. *Eng. Fract. Mech.*, 25:739–749, 1986.

[34] Akshantala N. A. and Talreja R. A micromechanics based model for predicting fatigue life of composite laminates. *Mater. Sci. Eng., A*, 285:303–313, 2000.

[35] Spearing S. M. and Beaumont P. W. R. Fatigue damage mechanics of composite materials. I: Experimental measurement of damage and post-fatigue properties. *Compos. Sci. Technol.*, 44:159–168, 1992.

[36] Spearing S. M., Beaumont P. W. R., and Ashby M. F. Fatigue damage mechanics of composite materials. II: A damage growth mode. *Compos. Sci. Technol.*, 44:169–177, 1992.

[37] Spearing S. M. and Beaumont P. W. R. Fatigue damage mechanics of composite materials. III: Prediction of post-fatigue strength. *Compos. Sci. Technol.*, 44:299–307, 1992.

[38] Spearing S. M., Beaumont P. W. R., and Smith P. A. Fatigue damage mechanics of composite materials. IV: Prediction of post-fatigue stiffness. *Compos. Sci. Technol.*, 44:309–317, 1992.

[39] Uleck K. R. *A hybrid model for fatigue life estimation of polymer matrix composites*. PhD thesis, University of Maryland, 2006.

[40] Noll T., Magin M., and Himmel N. Fatigue life simulation of multi-axial cfrp laminates considering material non-linearity. *Int. J. Fatigue*, 32:146–157, 2010.

[41] Diao X., Ye L., and Mai Y. Simulation of fatigue performance of cross-ply composite laminates. *Appl. Compos. Mater.*, 3:391–406, 1996.

[42] Halpin J. C., Jerina K. L., and Johnson T. S. Characterisation of composites for the purpose of reliability evaluation. In *Analysis of the Test Methods for High Modulus Fibres and Composites (ASTM STP-521)*, pages 5–64. American Society for Testing and Materials, Philadelphia, PA, 1974.

[43] Kabir M. R., Lutz W., Zhu K., and Schmauder S. Fatigue modeling of short fiber reinforced composites with ductile matrix under cyclic loading. *Comput. Mater. Sci.*, 36:361–366, 2006.

[44] Halpin J. C., Jerina K. L., and Johnson T. S. Fitting models to composite materials fatigue data. In *Test Methods and Design Allowables for Fibrous Composites (ASTM STP-734)*, pages 245–260. American Society for Testing and Materials, Philadelphia, PA, 1981.

[45] Van Paepegem W., Degrieck J., and De Baets P. Finite element approach for modelling fatigue damage in fibre-reinforced composite materials. *Composites Part B*, 32:575–588, 2001.

[46] Huang Z.-M. Simulation of the mechanical properties of fibrous composites by the bridging micromechanics model. *Composites Part A*, 32:143–172, 2001.

[47] Huang Z.-M. Micromechanical modeling of fatigue strength of unidirectional fibrous composites. *Int. J. Fatigue*, 24:659–670, 2002.

[48] Lian W. and Yao W. Fatigue life prediction of composite laminates by fea simulation method. *Int. J. Fatigue*, 32:123–133, 2010.

[49] Goda K. and Phoenix S. L. Reliability approach to the tensile strength of unidirectional cfrp composites by monte-carlo simulation in a shear-lag model. *Compos. Sci. Technol.*, 50:457–468, 1994.

[50] Curtin W. A. Tensile strength of fiber-reinforced composites. I: Model and effects of local fibre geometry. *J. Compos. Mater.*, 32:2042–2059, 1998.

[51] Okabe T. and Takeda N. Size effect on tensile strength of unidirectional cfrp composites - experiment and simulation. *Compos. Sci. Technol.*, 62:2053–2064, 2002.

[52] Mishnaevsky Jr. L. and Brøndsted P. Modeling of fatigue damage evolution on the basis of the kinetic concept of strength. *Int. J. Fract.*, 144:149–158, 2007.

[53] Mishnaevsky Jr. L. and Brøndsted P. Micromechanisms of damage in unidirectional fiber reinforced composites: 3d computational analysis. *Compos. Sci. Technol.*, 69:1036–1044, 2009.

[54] Qing H. and Mishnaevsky Jr. L. Unidirectional high fiber content composites: Automatic 3d fe model generation and damage simulation. *Comput. Mater. Sci.*, 47:548–555, 2009.

[55] van Delft D. R. V., Joosse P. A., and Rink H. D. Fatigue behaviour of fibreglass wind turbine blade material at very high cycle ranges. In *Proceedings of EWEC'94*, Thessaloniki, Greece, October 1994.

[56] Elices M. and Llorca J. *Fiber Fracture*. Elsevier Science, 2002.

[57] Jayatilaka A. De S. and Trustrum K. Statistical approach to brittle fracture. *J. Mater. Sci.*, 12:1426–1430, 1977.

[58] `http://en.wikipedia.org/wiki/Fracture_mechanics`.

[59] Epstein B. Statistical aspects of fracture problems. *J. Appl. Phys.*, 19:140–146, 1948.

[60] Coleman B. D. Time dependence of mechanical breakdown phenomena. *J. Appl. Phys.*, 27:862–866, 1956.

[61] Coleman B. D. Statistics and time dependence of mechanical breakdown in fibers. *J. Appl. Phys.*, 29:968–983, 1958.

[62] Coleman B. D. On the strength of classical fibres and fibre bundles. *J. Mech. Phys. Solids.*, 7:60–70, 1958.

[63] Watson A. S. and Smith R. L. An examination of statistical theories for fibrous materials in the light of experimental data. *J. Mater. Sci.*, 20:3260–3270, 1985.

[64] Padgett W. J., Durham S. D., and Mason A. M. Weibull analysis of the strength of carbon fibers using linear and power law models for the length effect. *J. Compos. Mater.*, 29:1873–1884, 1995.

[65] Thomason J. L. and Kalinka G. A technique for the measurement of reinforced fibre tensile strength at sub-milimeter gauge lengths. *Composites Part A*, 32:85–90, 2001.

[66] Wu E. M. and Robinson C. S. Computational micro-mechanics for probabilistic failure of fiber composites in tension. *Compos. Sci. Technol.*, 58:1421–1432, 1998.

[67] Gupta P. K., Inniss D., Kurkjian C. R., and Brownlow D. L. Determination of crack velocity as a function of stress intensity from static fatigue data. *J. Am. Ceram. Soc.*, 77:2445–2449, 1994.

[68] Brow P. K., Lower N. P., Lang A. J., and Kurkjian C. R. Structure and the intrinsic strength of glass. In *Proceedings of 7th International Otto Schott Colloquium*, Jena, July 2002.

[69] Kurkjian C. R., Gupta P. K., Brow P. K., and Lower N. The intrinsic strength and fatigue of oxide glasses. *J. Non-Cryst. Solids*, 316:114–124, 2003.

[70] Wiederhorn S. M. Influence of water vapor on crack propagation in soda-lime glass. *J. Am. Ceram. Soc.*, 50:407–414, 1967.

[71] Wiederhorn S. M. and Bolz L. H. Stress corrosion and static fatigue of glass. *J. Am. Ceram. Soc.*, 53:543–548, 1970.

[72] Armstrong J. L., Matthewson M. J., and Kurkjian C. R. Humidity dependence of the fatigue of high-strength fused silica optical fibers. *J. Am. Ceram. Soc.*, 83:3100–3108, 2000.

[73] Mrotek J. L., Matthewson M., and Kurkjian C. R. The fatigue of high-strength fused silica optical fibers in low humidity. *J. Non-Cryst. Solids*, 297:91–95, 2002.

[74] Pierre L. and Genet M. A new approach to the subcritical cracking of ceramic fibers. *Compos. Sci. Technol.*, 70:1575–1583, 2010.

[75] Zhang Z. and Hartwig G. Relation of damping and fatigue damage of unidirectional fibre composites. *Int. J. Fatigue*, 24:713–718, 2002.

[76] Hahn H. T and Turkgenc O. The effect of loading parameters on fatigue of composite laminates. part IV information systems. Technical report, 2000. Contract report DOT/FAA/AR-00/48.

[77] Jones F. R. Interphase formation and control in fibre composite materials. *Key. Eng. Mat.*, 116-117:41–60, 1996.

[78] Fraser W.A., Ancker F. H., Dibenedetto A. T., and Elbirli B. Evaluation of surface treatments for fibers in composite materials. *Polym. Composite*, 4:238–48, 1983.

[79] Larson B. K. and Drzal L. T. Glass fibre sizing/matrix interphase formation in liquid composite moulding: effects on fibre/matrix adhesion and mechanical properties. *Composites*, 25:711–721, 1994.

[80] Mallarino S., Chainlan J. F., and Vernet J. L. Glass fibre sizing effect on dynamic mechanical properties of cyanate ester composites. I: Single frequency investigations. *Eur. Polym. J.*, 41:1804–1811, 2005.

[81] Sato N. and Kurauchi T. Effect of fibre sizing on composite interfacial deformation studied by thermo-acoustic emission measurement. *J. Mater. Sci. Lett.*, 11:362–364, 1992.

[82] Thomason J. L. The interface region in glass fibre-reinforced epoxy resin composites: 3. characterization of fibre surface coatings and the interphase. *Composites*, 26:487–498, 1995.

[83] Van den Oever M. and Peijs T. Continuous-glass-fibre-reinforced polypropylene composites: II. influence of maleic-anhydride modified polypropylene on fatigue behaviour. *Composites Part A*, 29A:227–239, 1998.

[84] He M. Y., Evans A. G., and Curtin W. A. The ultimate tensile strength of metal and ceramic-matrix composites. *Acta Metall. Mater.*, 41:871–878, 1993.

[85] Cox H. F. The elasticity and strength of paper and other fibrous materials. *Brit. J. Appl. Phys.*, 3:72–79, 1952.

[86] Hedgepeth J. M. Stress concentrations in filamentary structures. Technical report, May 1961. NASA Technique Note, D882.

[87] Beyerlein I. J. and Phoenix S. L. stress concentrations around multiple fiber breaks in an elastic matrix with local yielding or debonding using quadratic influence superposition. *J. Mech. Phys. Solids*, 44:1997–2039, 1996.

[88] Rosen B. W. Tensile failure of fibrous composites. *AIAA J.*, 2:1985–1994, 1964.

[89] Galiotis C. A study of mechanisms of stress transfer in continuous- and discontinuous- fibre model composites by laser raman spectroscopy. *Compos. Sci. Technol.*, 48:15–28, 1993.

[90] Anagnostopoulos G., Parthenios J., Andreopoulos A. G., and Galiotis C. An experimental and theoretical study of the stress transfer problem in fibrous composites. *Acta Mater.*, 53:4173–4183, 2005.

[91] Satry A. M. and Phoenix S. L. Load redistribution near non-aligned fibre breaks in a two-dimensional unidirectional composite using break-influence superposition. *J. Mater. Sci. Lett.*, 12:1596–1599, 1993.

[92] Deng L. and Fan F. Statistical analysis of failure of unidirectionally fibre-reinforced composites with local load sharing. *Int. J. Fract.*, 59:69–81, 1993.

[93] Nedele M. R. and Wisnom M. R. Three-dimensional finite analysis of the stress concentration at a single fibre break. *Comp. Sci. Technol.*, 51:517–524, 1994.

[94] Nedele M. R. and Wisnom M. R. Stress concentration factors around a broken fiber in a unidirectional carbon fibre-reinforced epoxy. *Composites*, 25:549–557, 1994.

[95] Li H., Ja Y., Mamtimin G., Jiang W, and An L. Stress transfer and damage evolution simulations of fiber-reinforced polymer-matrix composites. *Mat. Sci. Eng. A-Struct.*, 425:178–184, 2006.

[96] Xia Z., Okabe T., and Curtin W. A. Shear-lag versus finite element models for stress transfer in fiber-reinforced composites. *Compos. Sci. Technol.*, 62:1141–1149, 2002.

[97] van der Heuvel P. W. J., Goutianous S., Young R. J., and Peijs T. Failure phenomenon in fibre-reinforced composites. part6: a finite element study of stress concentrations in unidirectional carbon fibre-reinforced epoxy composites. *Compos. Sci. Technol.*, 64:645–656, 2004.

[98] Hedgepeth J. M. and van Dyke P. Local stress concentrations in imperfect filamentary composite materials. *J. Compos. Mater.*, 1:294–309, 1967.

[99] Landis C. M., McGlockton M. A., and McMeeking R. M. An improved shear lag model for broken fibers in composites materials. *J. Compos. Mater.*, 33:667–680, 1999.

[100] Ochiai S., Schulte K., and Peters P. W. M. Strain concentration factors for fibers and matrix in unidirectional composites. *Compos. Sci. Technol.*, 41:237–256, 1991.

[101] Landis C. M. and McMeeking M. A. Stress concentrations in composites with interface sliding, matrix stiffness and uneven fiber spacing using shear lag theory. *Int. J. Solids Struct.*, 36:4333–4361, 1999.

[102] Qian C. Static tests on single glass fibres. Technical report, Knowledge Centre WMC, 2010. WMC internal report WMC-2010-25.

[103] http://www.isixsigma.com/tools-templates/sampling-data/how-determine-sample-size-determining-sample-size/.

[104] Comer A. J., Katnam K. B., Stanley W. F., and Young T. M. Characterising the behaviour of composite single lap bonded joints using digital image correlation. *Int. J. Adhes. Adhes.*, 40:215–223, 2013.

[105] Lava P., Cooreman S., Coppiters S., De Strycker M., and Debruyne D. Assessment of measuring errors in dic using deformation fields generated by plastic fea. *Opt. Lasers Eng.*, 47:747–753, 2009.

[106] Lava P., Cooreman S., and Debruyne D. Study of systematic errors in strain fields obtained via dic using heterogeneous deformation generated by plastic fea. *Opt. Lasers Eng.*, 48:457–468, 2010.

[107] Qian C., Westphal T., Nijssen R. P. L., and Zarouchas D. S. Measurements of axial stiffness degradation of unidirectional composite materials in tension-tension fatigue tests. Technical report, Knowledge Centre WMC, 2012. WMC internal report WMC-2012-100.

[108] Barnard P. M., Butler R. J., and Curtis P. T. The strength-life equal rank assumption and its application to the fatigue life prediction of composite materials. *Int. J. Fatigue*, 10:171–177, 1988.

[109] Mishnaevsky Jr. L. and Brøndsted P. Micromechanical modeling of strength and damage of fiber reinforced composites. Technical report, 2007. Risø-R-1601, ISBN: 978-87-550-3588-1.

[110] Qian C., Westphal T., Kasapoglou C., and Nijssen R. P. L. Fatigue simulations on a multiple-fibre unit cell of wind turbine composites. In *Proceeding of 3rd Thematic Conference on the Mechanical Response of Composites*, Hannover, Germany, 2011.

[111] Case S. W. *Mechanics of Fiber-Controlled Behavior in Polymeric Composite Materials*. PhD thesis, Virginia Polytechnic Institute and State University, 1996.

[112] *Marc 2008 R1 Manual, Volume B.*

[113] Qian C., Westphal T., and Nijssen R. P. L. Micro-mechanical fatigue modelling of unidirectional glass fibre reinforced polymer composites. *Comput. Mat. Sci.*, accepted.

[114] He T. An estimate of strengths of polymers. *Polymer*, 27:253–255, 1986.

[115] Landis C. M., Beyerlein I. J., and McMeeking M. A. Micromechanical simulation of the failure of fiber reinforced composites. *J. Mech. Phys. Solids.*, 48:621–648, 2000.

[116] Halpin J. C. and Kardos J. L. The halpin-tsai equations: a review. *Polym. Eng. Sci.*, 16:344–352, 1976.

[117] Christensen R. M. Tensor transformations and failure criteria for the analysis of fiber composite materials. *J. Compos. Mater.*, 22:874–897, 1988.

[118] Gamstedt E. K. *Fatigue Damage Mechanisms in Polymer Matrix Composites.* PhD thesis, Luleå University of Technology, 1997.

[119] Chi Z., Chou T., and Shen G. Determination of single fibre strength distribution from fibre bundle testings. *J. Mater. Sci.*, 19:3319–3324, 1984.

[120] Creasy T. S. A method of extracting weibull survival model parameters from filament bundle load/strain data. *Compos. Sci. Technol.*, 60:825–832, 2000.

[121] R'Mili M., Bouchaour T., and Merle P. Estimation of weibull parameters from loose-bundle tests. *Compos. Sci. Technol.*, 56:831–834, 1996.

[122] Hill R. and Okoroafor E. U. Weibull statistics of fibre bundle failure using mechanical and acoustic emission testing: the influence of interfibre friction. *Composites*, 26:699–705, 1995.

[123] Carlard V. and Lamon J. Failure of fibre bundles. *Compos. Sci. Tech.*, 64:701–710, 2004.

[124] Okoroafor E. U. and Hill R. Investigation of complex failure modes in fibre bundles during dynamic mechanical testing using acoustic emission and weibull statistics. *J. Mater. Sci.*, 30:4233–4243, 1995.

[125] Phoenix S. L. Probabilistic strength analysis of fibre bundle structures. *Fibre Sci. Technol.*, 7:15–31, 1974.

[126] Andersons J., Joffe R., Hojo M., and S. Ochiai. Glass fibre strength distribution determined by common experimental methods. *Compos. Sci. Technol.*, 62:131–145, 2002.

[127] Shioya M. and Takaku A. Estimation of fibre and interfacial shear strength by using a single-fibre composite. *Comp. Sci. Tech.*, 55:33–39, 1995.

[128] Wagner H. D. and Eitan A. Interpretation of the fragmentation phenomenon in single-filament composite experiments. *Appl. Phys. Lett.*, 56:1965–1967, 1990.

[129] Netravali A. N., Topoleski L. T. T., Sachse W. H., and Phoenix S. L. An acoustic emission technique for measuring fiber fragment length distributions in the single-fiber-composite test. *Comp. Sci. Tech.*, 35:13–29, 1989.

[130] Tamuzh V. P., Korabel'nikov Y. G., Rashkovan I. A., Karklin'sh A. A, Gorbatkina Y. A., and Zakjarova Y. T. Determination of scale dependence of strength of fibrous fillers and evaluation of their adhesion to the matrix, based on results of tests of elementary fibers in a polymer block. *Mech. Comp. Mater.*, 27:413–148, 1991.

[131] Manor A. and Clough R. B. In-situ determination of fiber strength and segment length in composites by means of acoustic emission. *Comp. Sci. Tech.*, 45:73–81, 1992.

[132] Pitkethley M. J., Favre J. P., U. Gaur, Jakubowski J., Mudrich S. F., Caldwell D. L., Nardin M., Wagner H. D., DiLandro L., Hampe A., Armistead J. P., Desaeger M., and Verpoest I. A round-robin programme on interfacial test methods. *Compos. Sci. Technol.*, 48:205–214, 1993.

[133] Herrera-Franco P. J. and Drzal L. T. Comparison of methods for the measurement of fibre/matrix adhesion in composites. *Composites*, 23:2–27, 1992.

[134] Andrews M. C., Day R. J., Patrikis A. K, and Young R. J. Deformation micromechanics in aramid/epoxy composites. *Composites*, 25:745–751, 1994.

[135] Nishikawa M., Okabe T., Hemmi K., and Takeda N. Micromechanical modeling of the microbond test to quantify the interfacial properties of fiber-reinforced composites. *Int. J. Solids Struct.*, 45:4098–4113, 2008.

[136] Kelly A. and Tyson W. R. Tensile properties of fiber reinforced metals: copper/tungsten and copper/molybdenum. *J. Mech. Phys. Solids*, 13:329–350, 1965.

[137] Yavin B., Gallis H. E., Scherf J., and Eitan A. Continuous mointoring of the fragmentation phenomenon in single fiber composite materials. *Polym. Compos.*, 12:436–446, 1991.

[138] Wimolkiatisak A. S. and Bell J. P. Interfacial shear strength and failure modes of interphase-modified graphite-epoxy composites. *Polym. Compos.*, 10:162–172, 1989.

[139] Drzal L. T., Rich M. J., Koening M. F., and Lloyd P. F. Adhesion of graphite fibers to epoxy matrics: II. the effect of fibre finish. *J. Adhesion*, 6:133–151, 1983.

[140] Bascom W. D. and Jensen R. M. Stress transfer in single fiber/resin tensile tests. *J. Adhesion*, 19:219–239, 1986.

[141] K. Kim J, Zhou L. M., and Mai Y. W. Stress transfer in the fibre fragmentation test. part I an improved analysis based on a shear strength criterion. *J. Mater. Sci.*, 28:6233–6245, 1993.

[142] Kim J. K. and Mai Y. W. Stress transfer in the fibre fragmentation test. part II multiple fibre composites. *J. Mater. Sci.*, 30:3024–3032, 1995.

[143] Park J., Kim J., and Goda K. A new method of evaluating the interfacial properties of composites by means of the gradual multi-fiber fragmentation test. *Compos. Sci. Technol.*, 60:439–450, 2000.

[144] Li A. F., Grubb D. T, and Phoenix L. Fibre interaction in the multi-fiber composite fragmentation test. *Compos. Sci. Technol.*, 54:251–266, 1995.

[145] Accorsi M. L., Pegoretti A., and Dibenedetto A. T. Dynamic analysis of fibre breakage in single- and multiple-fibre composites. *J. Mater. Sci.*, 31:4181–4187, 1996.

[146] van Den Heuvel P. W. J., Peijs T., and Young R. J. Analysis of stress concentration in multi-fibre microcomposites by means of raman spectroscopy. *J. Mater. Sci. Lett.*, 15:1908–1911, 1996.

[147] Mandell J. F., Chen J. H., and McGarry F. J. A microdebonding test for in situ assessment of fibre/matrix bound strength in composite materials. *Int. J. Adhes.*, 1:40–44, 1980.

[148] Kharrat M., Chateauminois A., Carpentier L., and Kapsa P. On the interfacial behaviour of a glass/epoxy composite during a micro-indentation test: assessment of interfacial shear strength using reduced indentation curves. *Composites Part A*, 28A:39–46, 1997.

[149] Zidi M., Carpentier L., Chateauminois A., Kapsa P., and Sidoroff F. Development of a micro-indentation model simulating different mechanical response of the fibre/matrix interface. *Compos. Sci. Technol.*, 61:369–375, 2001.

[150] Chen Y. M., Ruff A. W., and Dally J. W. A hybrid method for determining material properties from instrumented micro-indentation experiments. *J. Mater. Res.*, 9:1314–1321, 1994.

Acknowledgement

It is the best decision I have ever made to pursue my Doctoral Degree in the Netherlands. Over the past five years, there has been a very long list of individuals I would like to show my appreciation towards, for the warmth I get in this lovely country. First are my advisors Mr. Tim Westphal, Dr. Christos Kassapoglou and Dr. Rogier Nijssen. I want to thank them for their patient and brilliant guidance as supervisors, and their continuous encouragement and many helps on sharpening my English as friends. In addition, I want to pass along my sincere appreciation to my promotor Prof. Zafer Gürdal for his concerns and support, also to Mr. Don van Delft and Prof. Kuochi Zhang, for giving me the opportunity to carry on my PhD research.

Knowledge Centre WMC provides me a comfortable working environment and so many enthusiastic colleagues. It is my great pleasure to work with a group of people who are/were working at WMC Materials Department, especially Erik Stammes, Sibrand Raijmaekers, Alejandro Gonzalez, Dr. Josephine Sari, Partrick Dettmers, Dr. Dimistrios Zarouchas, Fransico Lahuerta, etc.. My special thanks are also to the helps from Dr. Martin Jan de Ruiter and Dr. Gerben de Winkel on my finite element simulations, and Jan Kuiken on my python scripts. Furthermore, I would like to thank the Hoorn-WMC carpool group (core members John Heijdra, Rogier Nijssen, Martin-Jan de Ruiter, etc.) for the convenience of driving me to and from work with lots of "what happens in the car stays in the car" jokes.

Last but not the least, I owe my deepest gratitude to my wife Shanshan Liu, my parents, my relatives and all my friends for their emotional support and encouragement during the hard times of my PhD. 特别对于我的父母与家人，我要再次感谢他们这些年来给予我的鼓励和支持，使我即使身在遥远的荷兰也能感觉到家的温暖。

Curriculum Vitae

Cheng Qian was born on July 19th 1983, in Tonghua, Jilin province, China. From September 1999 to June 2006, he pursued his Bachelor's and Master's degrees in School of Materials Science and Engineering, Beijing Institute of Technology. Right after receiving his Master's degree, Cheng moved to Faculty of Mechanical, Maritime and Materials Engineering in Delft University of Technology, for an one-year project sponsored by Infineon Technologies. His responsibility was to model the thermal mechanical properties of moulding compound materials, which are used as encapsulation materials for electronic components, during the cure process.

Since March 2008, he has been a joint PhD candidate with Knowledge Centre Wind turbine Materials and Constructions (WMC) and Faculty of Aerospace Engineering in Delft University of Technology. To complete this PhD project, he works entirely at WMC as a Research Scientist.